

CMOS-integrated biosensor circuits and systems : FMCW radar sensor for noncontact multimodal vital signs monitoring and coherent photoacoustic sensor for non-invasive in vivo sensing and imaging

Fang, Zhongyuan

2020

Fang, Z. (2020). CMOS-integrated biosensor circuits and systems : FMCW radar sensor for noncontact multimodal vital signs monitoring and coherent photoacoustic sensor for non-invasive in vivo sensing and imaging. Doctoral thesis, Nanyang Technological University, Singapore. <https://hdl.handle.net/10356/150277>

<https://hdl.handle.net/10356/150277>

<https://doi.org/10.32657/10356/150277>

This work is licensed under a Creative Commons Attribution-NonCommercial 4.0 International License (CC BY-NC 4.0).

Downloaded on 09 Apr 2024 10:36:41 SGT

**CMOS-Integrated Biosensor Circuits and Systems: FMCW
Radar Sensor for Noncontact Multimodal Vital Signs
Monitoring and Coherent Photoacoustic Sensor for Non-
invasive *In Vivo* Sensing and Imaging**

FANG ZHONGYUAN

School of Electrical & Electronic Engineering

A thesis submitted to the Nanyang Technological University
in partial fulfillment of the requirement for the degree of
Doctor of Philosophy

2020

Statement of Originality

I hereby certify that the work embodied in this thesis is the result of original research, is free of plagiarised materials, and has not been submitted for a higher degree to any other University or Institution.

22/09/2020

.....
Date

Zhongyuan Fang

.....
Fang Zhongyuan

Supervisor Declaration Statement

I have reviewed the content and presentation style of this thesis and declare it is free of plagiarism and of sufficient grammatical clarity to be examined. To the best of my knowledge, the research and writing are those of the candidate except as acknowledged in the Author Attribution Statement. I confirm that the investigations were conducted in accord with the ethics policies and integrity standards of Nanyang Technological University and that the research data are presented honestly and without prejudice.

22/09/2020



.....
Date

.....
Zheng Yuanjin

Authorship Attribution Statement

This thesis contains material from 9 paper(s) published in the following peer-reviewed journal(s) and from papers accepted at conferences in which I am listed as the first-author in 2 transactions (1 IEEE TMTT and 1 IEEE T-BioCAS) and 3 conferences (2 ISCAS, 1 SOCC). I am listed as a corresponding author in 2 conferences (1 SOCC and 1 ISCAS). I am listed as a first student author in 2 conferences (1 ISSCC, 1 ISCAS) and 1 journal (JSSC). The thesis also contains material of two papers to be submitted to JSSC and ISSCC 2021, where the ideas on implementing the multi-channel coherent I/Q matched detection, implementing the beamforming on improving the signal-to-noise ratio (SNR) based on the mixed-signal system-on-chip design are illustrated.

Chapter 3 is published as **Zhongyuan Fang**, Liheng Lou, Kai Tang, Wensong Wang, Yisheng Wang, Ting Guo, Chuanshi Yang, and Yuanjin Zheng, Wide Field-of-View Locating and Multimodal Vital Sign Monitoring Based on X-Band CMOS-Integrated Phased-Array Radar Sensor, **-IEEE Transactions on Microwave Theory and Techniques (2020)**. DOI: 10.1109/TMTT.2020.2989284.

The contributions of the co-authors are as follows:

- Prof. Yuanjin Zheng provided the initial project direction and edited the manuscript drafts.
- I prepared the manuscript drafts. The manuscript was revised by Dr. Liheng Lou.
- I co-designed the study with Prof. Yuanjin Zheng and performed the laboratory work at the School of Electrical and Electronic Engineering. I also developed the efficient algorithms for signal processing. I participated in the delay-locked-loop (DLL) design on-chip to enable the wide field-of-view beam steering of the radar sensor. I built up and tested the whole system.
- Dr. Liheng Lou helped configure the SPI of the radar chip board. Dr. Lou also helped set up the radar sensor for experiments and developed the transmitter on-chip including phase shifter and DLL.

- Dr. Kai Tang implemented the receiver front end on-chip.
- Dr. Wensong Wang participated in the design of the antenna array.
- Mr. Yisheng Wang implemented the digital synthesizer on-chip.
- Dr. Ting Guo implemented the power amplifier on-chip.
- Mr. Chuanshi Yang participated in the setting up of the testing and participate in the experiments for the bio-radar.

Chapter 3 is published as Zhe Liu, Liheng Lou, **Zhongyuan Fang**, Kai Tang, Ting Guo, and Yuanjin Zheng, A DLL-based Configurable Multi-Phase Clock Generator for True-Time-Delay Wideband FMCW Phased-Array in 40nm CMOS, - **IEEE International Symposium on Circuits and Systems (ISCAS), 2018**. DOI: 10.1109/ISCAS.2018.8351374.

The contributions of the co-authors are as follows:

- Prof. Yuanjin Zheng provided the initial project direction and edited the manuscript drafts.
- I participated in implementing the Vernier delay-locked-loop (DLL) based clock generator for wide bandwidth beam steering for the phased-array radar. I simulated and verified the design and participated in the layout.
- I performed the laboratory work with Dr. Liheng Lou on testing the DLL at the School of Electrical and Electronic Engineering.
- Dr. Liheng Lou proposed the Vernier DLL architecture.
- Ms. Zhe Liu helped on the testing of the circuits and wrote the paper.
- Dr. Kai Tang helped on the PCB board design.
- Dr. Ting Guo helped on the circuit testing.

Chapter 4 is published as, **Zhongyuan Fang**, Liheng Lou, Chuanshi Yang, Kai Tang, and Yuanjin Zheng, A Ku-band FMCW Radar on Chip for Wireless Micro Physiological Signal Monitoring by Interferometry Phase Analysis, - **IEEE International Symposium on Circuits and Systems (ISCAS), 2018**. DOI: 10.1109/ISCAS.2018.8351226.

The contributions of the co-authors are as follows:

- Prof. Yuanjin Zheng provided the initial project direction and edited the manuscript drafts.
- I came out the ideal of leveraging the *Ku*-band FMCW radar sensor on sensing tiny vital signs under the guidance of Prof. Zheng and built up the testing architecture including the antenna, radar chip, and the algorithm for signal processing and prepared the manuscript drafts with the help of Dr. Lou and Prof. Zheng. The manuscript was further modified by Prof. Yuanjin Zheng and Dr. Liheng Lou.
- I started the study under the supervision of Prof. Yuanjin Zheng and performed the laboratory work with Dr. Liheng Lou.
- Dr. Liheng Lou designed the transmitter part of the radar transceiver.
- Dr. Kai Tang designed the receiver part of the radar on-chip and designed the testing PCB.
- Mr. Chuanshi Yang prepared the laboratory for the testing.

Chapter 4 is also published as **Zhongyuan Fang**, Liheng Lou, Kai Tang, Ting Guo, Bo Chen, Yisheng Wang, Chuanshi Yang, Longjie Zhong, and Yuanjin Zheng, A Digital-Enabled Interferometric Radar Sensor for Physiological Sign Monitoring, **-IEEE International System-on-Chip Conference (SOCC), 2019**. DOI: 10.1109/SOCC46988.2019.1570571644.

The contributions of the co-authors are as follows:

- Prof. Yuanjin Zheng provided the initial project direction and edited the manuscript drafts.
- I leverage the in-phase (I)/ quadrature (Q) based coherent detection method to detect the tiny signals related to vital signs accurately and specifically under the guidance of Prof. Zheng. I built up the system architecture including the antenna, radar chip, and the algorithm for signal processing and prepared the manuscript drafts. The manuscript was revised by Prof. Yuanjin Zheng and Dr. Liheng Lou.
- Dr. Kai Tang designed the receiver front end of the radar on-chip.
- Dr. Bo Chen designed the PA for the transmitter.
- Dr. Ting Guo designed the DA for the transmitter and helped testing.
- Mr. Yisheng Wang designed the frequency synthesizer on-chip.

- Mr. Chuanshi Yang participated in the experiments and testings.
- Dr. Longjie Zhong participated in the discussions on algorithm optimization and provided advice on manuscript writing.

Chapter 4 is published as **Zhongyuan Fang**, Chuanshi Yang, Haoran Jin, Liheng Lou, Kai Tang, Xiaoyan Tang, Ting Guo, Wensong Wang, and Yuanjin Zheng, A Digital-Enhanced Chip-Scale Photoacoustic Sensor System for Blood Core Temperature Monitoring and In Vivo Imaging, **-IEEE Transactions on Biomedical Circuits and Systems (2019)**. DOI: 10.1109/TBCAS.2019.2943823.

The contributions of the co-authors are as follows:

- Prof. Yuanjin Zheng provided the initial project direction and edited the manuscript drafts.
- I came out the ideal of using the coherent detection method on sensing tiny but vital photoacoustic signals in a mixed-signal way under the guidance of Prof. Zheng. I developed the system architecture and prepared the manuscript drafts. The system architecture is further modified by Prof. Zheng before tape-out. The manuscript was revised by Prof. Yuanjin Zheng and Dr. Liheng Lou.
- I co-designed the study with Prof. Yuanjin Zheng and performed the laboratory work at the School of Electrical and Electronic Engineering. I also initiated the idea and developed the mixed-signal IC loop to enable the essential coherent detection. I implemented the Gilbert cell to enable the mixed-signal correlation process on-chip. I developed the innovative system including the AD/DA board and the FPGA implementation, which is scalable and flexible. I developed the algorithms on photoacoustic signal processing.
- Mr. Chuanshi Yang implemented the design of the LNA, VGA and filter.
- Dr. Haoran Jin helped on implementing the experiments.
- Dr. Liheng Lou participated in the testing and the modified the architecture of the system.
- Dr. Kai Tang helped on implementing the PCB board.
- Ms. Xiaoyan Tang developed the code for FPGA implementation.

- Dr. Ting Guo participated in the circuit testing and PCB design.
- Dr. Wensong Wang helped on testing and revising the manuscript.

Chapter 4 is also accepted as **Zhongyuan Fang**, Chuanshi Yang, Kai Tang, Liheng Lou, Wensong Wang, Haoran Jin, Xiaoyan Tang, and Yuanjin Zheng, A Quadrature Adaptive Coherent Lock-in Chip-Based Sensor for Accurate Photoacoustic Detection, - **IEEE International Symposium on Circuits and Systems (ISCAS), 2020**, which will appear on IEEE Xplore soon.

The contributions of the co-authors are as follows:

- Prof. Yuanjin Zheng provided the initial project direction and edited the manuscript drafts.
- Under the guidance of Prof. Zheng, I came out the ideal of leveraging the in-phase (I) and quadrature (Q) based templates to achieve the closed-loop coherent detection on target PA signals. The whole system architecture is implemented with a scalable and configurable form, proposing the efficient mixed-signal algorithms on the photoacoustic signal processing. I prepared the manuscript drafts. The manuscript was revised by Prof. Yuanjin Zheng.
- Mr. Chuanshi Yang developed the front end including LNA, LPF and VGA of the PA receiver.
- Dr. Kai Tang helped design the PCB power board.
- Dr. Liheng Lou participated in the experimental setup for the circuit system and participated in the writing modifications.
- Dr. Wensong Wang participated in the experimental settings, discussed on the optimization of the algorithms, and helped modify the manuscript.
- Dr. Haoran Jin helped built up the bio-experimental setting and implemented the related experiments.
- Ms. Xiaoyan Tang helped implement the FPGA code for the algorithm.

22-09-2020

.....
Date

Zhongyuan Fang

.....
Fang Zhongyuan

Acknowledgments

As time flies by, the four-year Ph.D. study has been completed. I have successfully designed several high-performance mixed-signal CMOS-integrated sensor circuits and systems aiming at the efficient ubiquitous healthcare monitoring and early disease diagnosis for the incoming internet-of-everything (IoE) era. Moreover, multimodal sensor ICs have been developed.

I acknowledge Prof. Yuanjin Zheng on the supervision and support, who guides the right way towards coming out with novel ideas and implementing innovative research on integrated circuits and systems. I am grateful to Dr. Liheng Lou, who helps a lot with the IC research. I acknowledge Dr. Kai Tang with the help of the IC design. I acknowledge Dr. Wensong Wang on the efficient and productive collaborations on antenna-circuit co-design. I acknowledge Dr. Longjie Zhong for the helpful discussions on interface IC design. I acknowledge Mr. Yanshu Guo from Tsinghua University to collaborate on the subsampling FSK receiver design. I am grateful to Prof. Chun-Huat Heng from NUS and Prof. Hanjun Jiang from Tsinghua University for the helpful discussions and suggestions on the low-power receiver IC design. I acknowledge Ms. Xiaoyan Tang and Mr. Chuanshi Yang's work on the integrated PA sensing system implementation. I also acknowledge some of my long-time friends, Mr. Tongyu Zong at the New York University, Mr. Zhengzhong Tu at the University of Texas, Austin, Mr. Xiang Ge at the Fudan University, Mr. Bo Peng at University of Cambridge, Mr. Jiawei Chen at the UC Berkeley, and Mr. Xiaojie Tan at NUS for their supports. I need to acknowledge my father, a scientist and a technical official, for his encouragement on me toward research. I am grateful to Dr. Meisheng Zhou, an experienced professional in the semiconductor industry and Fudan alumni, who provided me with useful advice on the semiconductor research. I acknowledge Prof. Hao Min and Prof. Na Yan at Fudan University, where I started the research on integrated circuit and system design under their supervision as an undergraduate research assistant from 2014 to 2016.

I will keep exploring further on the high-performance mixed-signal integrated circuits and systems design for the next-generation IoE applications. I hope to make contributions to Chinese semiconductor developments.

Summary

For pervasive healthcare monitoring and potential disease diagnosis, biosensors which can be deployed massively with compact size, low power consumption, and efficient and effective near-sensor processing capabilities are required. Synergetic optimizations on multi-physical sensing mechanisms, circuits, and efficient signal processing algorithms are needed to enable the efficient and effective operation. In the intricate and noisy scenarios, current sensor devices are usually limited by the detecting accuracy, low specificity, and large power consumption. Moreover, current sensors realized by discrete blocks are usually with bulky size, which is inconvenient for the massive deployment for pervasive healthcare monitoring applications.

With the rapid development of CMOS technologies, biosensors are on the way to be monolithically integrated into a single chip to enable the highly efficient data acquisition and effective signal processing with low-power consumption and small size. The sensor data is acquired and processed at the edge near-sensor; thus, the data movement's power consumption is eliminated. Moreover, multi-physical sensing mechanisms can be utilized to enhance the biosensor's capability, achieving multimodal sensor fusion by leveraging the advantages of complementary physical mechanisms, demonstrating enormous potential to be used for global COVID-19 pandemic.

The CMOS-integrated radar sensor is a suitable candidate to monitor multimodal vital signs and detect specific movements like falling in a noncontact way utilizing electromagnetic (EM) waves. To further enable multimodal biomedical sensing for pervasive healthcare applications, considering that photoacoustic sensor is realized based on light excitation and acoustic sensing, which can be used to achieve the non-invasive monitoring on the in-depth blood core temperature and *in vivo* imaging on the target tissues.

In the thesis, a CMOS-integrated phased-array radar sensor prototype fabricated in the GlobalFoundries 65-nm CMOS process for wide field-of-view (FoV) multimodal vital sign monitoring and falling detection is presented. The co-design of integrated circuit blocks and effective signal processing algorithms is implemented to enable the accuracy, low power consumption, and reliability of the radar sensor for noncontact health applications. Furthermore, to enable the in-depth blood core temperature monitoring and *in vivo* imaging, a high-precision CMOS-integrated mixed-signal coherent lock-in photoacoustic sensor prototype is fabricated in GlobalFoundries 65-nm CMOS process, achieving potential disease diagnosis and health monitoring with compact size. Moreover, a four-channel photoacoustic system-on-chip (SoC) was fabricated in TSMC 65-nm process, which includes the analog front end (AFE), analog-to-digital converter (ADC), digital-to-analog converter (DAC), and the digital processing module implementing coherent lock-in and accurate beamforming on-chip to achieve accurate detection on in-depth target photoacoustic signals with an enhanced signal to noise ratio (SNR), improved sensitivity, and high specificity for the first time.

By the optimizations on the mixed-signal integrated circuits (ICs) design, energy-efficient sensor signal processing algorithms, and the multi-physical sensing mechanisms including EM, acoustics and optical techniques, the CMOS-based radar sensor and photoacoustic sensor prototypes have verified their capabilities on accurate multimodal noncontact vital signs monitoring, falling detection, non-invasive temperature monitoring, and in-depth *in vivo* vessel imaging. The thesis explores the CMOS-integrated mixed-signal circuits and systems leveraging multi-modal sensing techniques for efficient and effective versatile sensing, pervasive healthcare monitoring, and potential disease diagnosis for the current COVID-19 pandemic as well as for the incoming intelligent Internet of Everything (IoE) era.

Table of Contents

Acknowledgement	i
Summary	ii
List of Figures	viii
List of Tables	xiv
List of Acronyms	xvi
Chapter 1 Introduction	1
1.1 Background and Motivation	2
1.2 Objectives	2
1.3 Major Contributions of the Thesis.....	4
1.4 Organization of the Thesis.....	6
Chapter 2 Review of the Biomedical Radar Sensors and Photoacoustic Sensors	8
2.1 Biomedical Sensor Techniques for Pervasive Healthcare	8
2.2 Introduction to Biomedical Radar Sensors	11
2.2.1 Comparison of Radar Architectures	11
2.2.2 Radar Signal Processing Methods for Healthcare Applications	17
2.3 Photoacoustic Sensor Systems for Non-invasive In Vivo Sensing and Imaging	25
2.3.1 Photoacoustic Principle	26
2.3.2 Photoacoustic Sensor for Non-invasive Temperature Monitoring.....	27
2.3.3 Photoacoustic Sensor for <i>in vivo</i> Imaging	30
2.4 Summary of Review	36

Chapter 3 CMOS-Integrated Radar Sensor Design for Multimodal Vital Sign Monitoring, Falling Detection, and Versatile Sensing	37
3.1 Chip-Scale Radar Sensors for Healthcare Application	38
3.2 CMOS-Integrated Radar Sensor Design	40
3.2.1 Link Budget Analysis for the Proposed Radar Sensor	42
3.2.2 Accurate Beam-Steering for the Subject Localization in a Wide Field-of-View	44
3.2.3 Vivaldi Antenna Array for Broadband Radar Transmitter Beam-Steering..	49
3.2.4 ITPA Algorithm for Discerning Multimodal Vital Signs	51
3.3 Experimental Verifications and Analysis	57
3.4 Discussion and Comparison	64
3.5 DLL-based Multi-Phase Clock Generator for True-Time-Delay Wideband FMCW Phased-Array Radar Sensor	69
3.5.1 Principle of DLL.....	69
3.5.2 Vernier-Based DLL Architecture	71
3.5.3 Circuit Implementation.....	73
3.5.4 Testing and Measurement Results.....	74
3.6 Chip-Scale 1TX-1RX <i>Ku</i> -Band FMCW Radar Sensor for Respiration Monitoring, Falling Detection, and Motion Recognition.....	77
3.6.1 Chip-Scale <i>Ku</i> -Band Radar Sensor Architecture	78
3.6.2 Experiments on Monitoring Breathing and Falling Detection	80

3.6.3 Chip-Scale Radar Sensor for Noncontact Motion Detection	83
3.7 <i>I/Q</i> -based Coherent Radar for Enhanced Detection Capability	84
3.8 Summary.....	85
Chapter 4 Digital-Enhanced Chip-Scale Photoacoustic Sensor for Blood Core Temperature Monitoring and <i>In Vivo</i> Imaging	87
4.1 Photoacoustic Sensor for Physiological Sign Monitoring.....	88
4.2 Chip-Based PA Sensor System Architecture	91
4.2.1 Sensor System for Coherent Photoacoustic Detection	92
4.2.2 <i>In Vivo</i> Digital-Enhanced Coherent Photoacoustic Signal Detection Technique	94
4.3 Photoacoustic Sensor System Implementation.....	98
4.3.1 Analog Front-End (AFE) of the Sensor Chip.....	98
4.3.2 System-Level Implementation of the Mixed-Signal Coherent Closed-Loop PA Sensor	103
4.4 Experiments and Measurement Results	105
4.5 <i>I/Q</i> -Based Coherent Lock-in Technique for PA Signal Detection Based on Early-Late Tracking.....	110
4.6 4-channel Coherent PA SoC Design	114
4.6.1 Gilbert Cell Implementation.....	116
4.6.2 DAC.....	116
4.7 Summary.....	120
Chapter 5 Conclusions and Recommendation for Future Work	121

5.1 Conclusions	121
5.2 Recommendation for Future Work	122
5.2.1 FSK Transceiver for ULP Communication	124
5.2.2 CMOS-Integrated UWB Radar Sensor for Accurate Multimodal Vital Signs Monitoring.....	125
5.2.3 Efficient Algorithm for Radar Signal Processing.....	126
Author's Publications	128
Bibliography	132

List of Figures

Figure 2.1. Proposed pervasive healthcare solution enabled by noncontact radar sensors and portable non-invasive photoacoustic sensors	9
Figure 2.2. Block diagram of a single frequency CW radar	12
Figure 2.3. Block diagram of the UWB radar.....	12
Figure 2.4. Block diagram of the FMCW radar.....	12
Figure 2.5. Schematic of a continuous phase tracking radar [105].....	13
Figure 2.6. Schematic of a burst-chirp UWB radar sensor [107], [119].....	13
Figure 2.7. Schematic of an SoC UWB pulse radar sensor [28].....	14
Figure 2.8. Schematic of an impulse radio radar sensor [26]	14
Figure 2.9. Schematic of the FMCW radar for gesture recognitions [106]	15
Figure 2.10. Geometry of radar and target with translation and rotation [42].....	17
Figure 2.11. Flowchart of the method leveraging FTPR algorithm for heartbeat detection [6].....	18
Figure 2.12. (a) UWB experimental setup, and (b) heartbeats restored from the PCA [109].....	19
Figure 2.13 (a) Photography of the radar hardware. (b) Synchronization module for the signal generator and DAQ. (c) Block diagram of the radar system and experimental setup [23].	20
Figure 2.14. The signal processing flow of the FMCW radar healthcare monitoring [23].	20
Figure 2.15. Photoacoustic phenomenon and the sensing and imaging on target	26
Figure 2.16. Schematic of a typical photoacoustic sensing device for blood temperature. (a) Main body; (b) Sensor head (acoustic module and optical module) (c) Trigger signal and the PA response signals; (d) Final system setup and illustration of each part. FC:	

fiber coupler, LD: laser diode, MMF: multimode fiber, PD: photodiode, Tx: Transmitter, VGA: variable gain amplifier, LNA: low noise amplifier, DSP: digital signal processor, ADC: analog to digital converter [68].	29
Figure 2.17. PA imaging with ultrasound imaging probe. (a) Two-dimensional array probe and (b) Linear array probe for dual mode PAT-US imaging.	32
Figure 2.18. Experimental setup of the coherent PAUS correlation and imaging. ConL, condenser lens; FC, fiber collimator; MMF, multimode fiber; ND, neutral density; BS, beam splitter; PD, photodiode; US, ultrasound transducer [58].	33
Figure 2.19. Acoustic-resolution photoacoustic microscopy (AR-PAM) system used for imaging the skin vasculature. (a) Schematic of system, (b) region of forearm scanned, (c) lateral x–y MIP image, (d) vertical x–z slice image taken along vertical line in (c) [90].	35
Figure 2.20. (a) Compact PA and US system. (b) FPGA-enabled system. [113].	36
Figure 3.1. Radar-based healthcare and chronic disease monitoring deployed in a wide field-of-view: (a) Conventional radar sensors, and (b) proposed CMOS-integrated phased-array radar sensor	39
Figure 3.2. CMOS-integrated phased-array radar sensor for vital sign monitoring and falling detection [117].	41
Figure 3.3. True time delay generated by the Vernier Delay Matrix.	45
Figure 3.4. (a) X-band Phase shifter and (b) circuit of the IQ current generator.	46
Figure 3.5. Two-Stage Beam-steering principle for the proposed chip-scale radar sensor [117].	47
Figure 3.6. Antenna implementation: (a) Element photo, and (b) radiation pattern at 10 GHz [117].	49

Figure 3.7. Antenna array patterns at 10 GHz with steering angles from -30° to 30° with a 10° interval [117].	49
Figure 3.8. Transmitted chirp waveform and the de-chirping process at receiver.	51
Figure 3.9. Flowchart of the ITPA algorithm for ranging and vital sign monitoring [117].	52
Figure 3.10. Illustration of the interferometric time-phase analysis algorithm	56
Figure 3.11. Experiment illustration: (a) Algorithm implementation in the experiment, and (b) systematic configuration of the radar sensor	57
Figure 3.12. Measured spectrum of the chirp signal from transmitter antenna	59
Figure 3.13 Measured spectrum of the de-chirped IF signal after the mixer.....	59
Figure 3.14. Experimental setup and environment: (a) Radar system and subjects in the scene with illustration, and (b) localization of subjects in the experiment.	59
Figure 3.15. Respiration and heartbeat measurement at 0° : (a) Phase pattern in time domain, and (b) spectrum of the interferometric phase after ITPA.....	60
Figure 3.16. Respiration and heartbeat measurement at 30° : (a) Phase pattern in time domain, and (b) spectrum of the interferometric phase after ITPA.....	62
Figure 3.17. Tested respiration/heartbeat rate from radar system for the subject at 0° direction, and standard measurement results [117].....	62
Figure 3.18. Detected falling at 0° using the ITPA algorithm: (a) Signatures in time domain, and (b) spectrum of the interferometric phase signature.	63
Figure 3.19. Detected falling at 30° using the ITPA algorithm: (a) Signatures in time domain and (b) spectrum of the interferometric phase signature [117].....	63

Figure 3.20. Measured 4-element TX beam-steering radiation pattern at 10 GHz with: (a) $\pm 60^\circ$ scan angles with coarse scanning of 10° steps and (b) Fine beam control of $\sim 1^\circ$ steps at 2λ antenna pitch. [129].....	66
Figure 3.21. A testing setup of the phased-array chip-scale radar system [129]	66
Figure 3.22. (a) A 4-channel TX and (b) True-time-delay in multiphase output [123].	70
Figure 3.23. The structure of the Vernier architecture DLL [123].	72
Figure 3.24. (a) The circuit of voltage-controlled delay cell. (b) V_{tune} versus delay time in VCDC [123].....	74
Figure 3.25. The circuit of charge pump [123]	74
Figure 3.26. Cell number vs. delay time (J is the cell number in primary loop and K in secondary loops) [123].....	75
Figure 3.27. The simulated and measure delay time (a) at 400MHz, the simulated and (b) measure delay time at 1 GHz [123].....	75
Figure 3.28. Measured delay time at 1GHz with 7-stage VCDL [123]	76
Figure 3.29. The measured 4-channel outputs and the synthesized radiation pattern [123]	76
Figure 3.30. Die photograph of the Vernier DLL [123]	77
Figure 3.31. Chip-scale FMCW radar sensor architecture [35].....	80
Figure 3.32. Radar sensor experimental setup [35]	82
Figure 3.33. Preliminary results on respiration rate and falling monitoring [35]	82
Figure 3.34. An illustrative scenario of the one-channel chip-scale FMCW radar sensors deployed for healthcare monitoring.	82

Figure 3.35. (a) The setup of the motion detection using the chip-scale radar sensor and	
(b) The detection on the hand motion [121]	84
Figure 4.1. Illustration of photoacoustic effect.	88
Figure 4.2. Conventional photoacoustic sensor system with commercial transducer ..	90
Figure 4.3. System diagram of the proposed chip-based coherent lock-in photoacoustic	
sensor system for in vivo physiological signal sensing and in-depth imaging [120] ...	91
Figure 4.4. Measured PA signal induced by a low-power laser under poor SNR and	
interferences environment.....	96
Figure 4.5. Extracted target PA waveform profile under strong laser excitation processed	
by coherent summation and averaging	96
Figure 4.6. Target PA signal capturing [120].	97
Figure 4.7. Schematics of key analog frontend circuit blocks of the PA sensor system:	
(a) Low noise amplifier (LNA). (b) Low-pass filter (LPF). (c) Variable gain amplifier	
(VGA). (d) Gilbert cell [120]......	99
Figure 4.8. Schematic of the CMFB in the LNA [120].	99
Figure 4.9. Simulation result of noise versus frequency of the LNA [120].....	102
Figure 4.10. Post-simulation result of gain versus frequency of the 3rd order LPF [120].	
.....	102
Figure 4.11. Simulated gain versus control voltage of the VGA [120].	102
Figure 4.12. Measured gain versus control voltage of the chain of LNA, LPF and VGA	
[120]......	102
Figure 4.13 Illustration of the template waveform generation under coherent lock-in, the	
reconstruction on the target signal and the gated integration.	104

Figure 4.14. (a) Raw received PA signal induced by extreme weak laser. (b) Reconstructed profile of the target PA signal with SNR enhancement.	104
Figure 4.15. Illustration of the PA sensor chip: (a) PCB testing board. (b) Die microphotograph [120]	105
Figure 4.16. Experimental setup of the chip-scale PA sensor system for the biomedical experiments. (a) Schematic, and (b) test environment [120].	107
Figure 4.17. Temperature measurement results under the extreme weak laser illumination using the chip-scale PA sensor system. (a) Conventional open-loop measurement results. (b) Closed-loop temperature measurement results under lock-in state [120].....	107
Figure 4.18. <i>In vivo</i> vessel imaging under weak laser illumination. (a) Conventional open-loop imaging results. (b) Closed-loop imaging results under lock-in state [120]	107
Figure 4.19. Illustration of the proposed QuACL system: (a) Photoacoustic effect. (b) Pulsed laser for inducing the PA signal at the object. (c) System diagram.	111
Figure 4.20. (a) Illustration of the I and Q templates. (b) Spectrum of the PA template. (c) Illustration of early-late tracking loop with discrimination curve indicated.	112
Figure 4.21. Measured temperature under weak laser irradiating phantom in hot water. (a) Measured result with direct amplitude-temperature mapping. (b) Measured results using one-channel coherent PA detection. (c) Measured results using mixed-signal quadrature coherent PA detection	113
Figure 4.22. Block diagram of the 4-channel I/Q based coherent PA sensor SoC with early-late tracking function	115
Figure 4.23. (a) Circuit diagram of the Gilbert cell. (b) Layout of the Gilbert cell....	116

Figure 4.24. System architecture of the 8-bit current-steering DAC.....	117
Figure 4.25. Block diagram of the Decode_1 st module... ..	117
Figure 4.26. Block diagram of the Decode_2 nd module... ..	117
Figure 4.27. Schematic of the 4-bit binary to thermometer converter.....	118
Figure 4.28. Circuit diagram of the buffer.....	119
Figure 4.29. (a) Circuit diagram of the latch synchronizer. (b) Circuit diagram of the current cell	119
Figure 4.30. Layout of the 8-bit current steering DAC.....	119
Figure 5.1. The schematic of the AFS FSK TRX.....	123
Figure 5.2. Schematic of the current bleeding Gilbert cell for AFS FSK TRX.....	123
Fig. 5.3. Measured parallel impedance R_p of two different devices at the parallel resonant frequencies of 911.9 MHz and 923.1 MHz [131].	124
Figure 5.4. Proposed coherent chirped UWB CMOS-integrated radar sensor with turbo mood closed-loop tracking.....	125
Figure 5.5. Proposed robust and accurate algorithm for multimodal vital signs monitoring based on radar sensor.....	126

List of Tables

TABLE 2-1. Comparison of Features of Different Radar Sensors	21
TABLE 2-2. Summary of Chip-Scale CW and FMCW Radars	22
TABLE 2-3. Summary of Chip-Scale UWB Radars	23
TABLE 2-4. Comparison of Features of Different Non-Invasive Temperature Monitoring Sensor Types [68].	30
TABLE 3-1. Link Budget Calculations	43
TABLE 3-2. Phase Shifting Settings at Each Channel for Steering Angles of 0° and 30°	60
TABLE 3-3. Comparison with the State-of-the-Art Radar Sensors	65
TABLE 3-4. Circuit Parameters of the X-Band Phased-Array Prototype and Comparison	68
TABLE 3-5. Performance Comparison of the DLL Clock Generator	77
TABLE 4-1. Technology Summary and Comparison with Prior Arts	109

List of Acronyms

AC	Alternating Current
ADC	Analog-to-Digital Converter
AFE	Analog Front End
AI	Artificial Intelligence
ASIC	Application-Specific Integrated Circuit
BPF	Band-Pass Filter
BW	Bandwidth
CMOS	Complementary Metal-Oxide Silicon
CMFB	Common-Mode Feedback
CML	Current-Mode Logic
CNN	Convolutional Neural Network
CP	Charge Pump
CPU	Central Processing Unit
CT	Computed Tomography
CW	Continuous Wave
DA	Driver Amplifier
DAC	Digital-to-Analog Convertor
DAQ	Data Acquisition
DC	Direct Current
DCO	Digital Controlled Oscillator
DDS	Direct Digital Synthesizer
DLL	Delay-Locked Loop
DSP	Digital Signal Processing
EM	Electromagnetic

ENOB	Effective Number of Bits
FCC	Federal Communications Commission
FFT	Fast Fourier Transform
FMCW	Frequency Modulated Continuous Wave
FOV	Field of View
FPGA	Field-Programmable Gate Array
FR	Flame Retardant
FSK	Frequency Shift Keying
FTPR	Frequency-Time Phase Regression
GPU	Graphical Processing Unit
HPF	High-Pass Filter
HSMC	High Speed Mezzanine Card
IC	Integrated Circuit
IF	Intermediate Frequency
IFFT	Inverse Fast Fourier Transform
IoE	Internet of Everything
IR	Impulse-Radio
ISAR	Inverse Synthetic Aperture
ISM	Industrial, Scientific and Medical
ITPA	Interferometric Time-Phase Analysis
LNA	Low Noise Amplifier
LPF	Low-Pass Filter
LO	Local Oscillator
LOS	Line-of-Sight
LUT	Lookup Table

MEMS	Microelectromechanical System
MIR	Middle Infrared
MPS	Multi-Phase Synthesizer
MRI	Magnetic Resonance Imaging
MUSIC	Multiple Signal Classification
MUX	Multiplexer
NAND	Not-And
NIR	Near Infrared
PA	Photoacoustic
PC	Personal Computer
PCA	Principal Component Analysis
PCB	Print Circuit Board
PET	Positron Emission Tomography
PFD	Phase Frequency Detector
PGA	Programmable-Gain Amplifier
PLL	Phase-Locked Loop
PRF	Pulse Repetition Frequency
PRI	Pulse Repetition Interval
PS	Phase Shifter
PVT	Process, Voltage and Temperature
PZT	Piezoelectric Transducer
RAM	Random Access Memory
RF	Radio Frequency
RFFE	Radio Frequency Front End
RMSE	Root Mean Square Error

RNN	Recurrent Neural Network
RX	Receiver
SNR	Signal-to-Noise Ratio
SPI	Serial Peripheral Interface
SoC	System-on-Chip
TRX	Transceiver
TSMC	Taiwan Semiconductor Manufacturing Company
TX	Transmitter
US	Ultrasound
ULP	Ultra-Low-Power
UWB	Ultra-Wideband
VCDC	Voltage Controlled Delay Cell
VCDL	Voltage Controlled Delay Line
VCO	Voltage-Controlled Oscillator
VGA	Variable-Gain Amplifier

Chapter 1

Introduction

Through the global aging, the percentage of seniors becomes higher and higher. It is estimated that 15% of people will be aged over 65 by 2040 [1], among them, many elderlies will face chronic diseases like diabetes, etc. Moreover, it is estimated that 0.85%-1.5% of total healthcare expenditures are related to falling [2]. It is essential to achieve the pervasive monitoring on healthcare indicators in an easy and convenient way, where in-time detection of the falling and the monitoring on multimodal vital signs like respiration rate and heartbeat rate variations are realized with low cost, high efficiency, high sensitivity and specificity.

As the radar sensors are immune to light interferences and have capabilities of long detection range, high accuracy, as well as high-level protection on the privacy of the subject, it is one of the most promising candidates for noncontact multimodal vital signs monitoring and falling detection [2], [4]-[8]. Besides detecting the macro movements like falling and micro-movements like respiration rate and heartbeat rate based on the radar sensors, it is also essential to monitor blood core temperature and realize accurate imaging on vessels in a convenient and easy-deployable way, which is critical for portable potential disease diagnosis in the current global COVID-19 pandemic. As the photoacoustic (PA) sensor demonstrates the potential for wearable disease diagnosis due to its characteristics of non-invasive, fitness, compactness, and imaging ability, a chip-based PA sensor is designed, where blood core temperature monitoring and vessel imaging can be achieved simultaneously. Leveraging the advancement of complementary metal-oxide-semiconductor (CMOS) techniques, sensor circuits and systems are to be realized with small size and low power consumption.

The thesis presents the novel CMOS-integrated radar sensors and chip-based photoacoustic sensors for biomedical applications, including the design of the analog front-end (AFE), radiofrequency front-end (RFFE), the digital processing module, and efficient signal processing algorithms. Mixed-signal coherent sensor data processing method is proposed to enable accurate capturing of the target signal, precise target signal reconstruction, and feature extraction, where the interferometric phase processing algorithm is used for the CMOS-integrated radar sensor for multimodal vital sign monitoring. The novel mixed-signal coherent detection method is used for the photoacoustic sensing and imaging with improved signal to noise ratio (SNR) and enhanced interference suppression capabilities.

1.1 Background and Motivation

Healthcare sensors have been developed rapidly, and the quality of people's lives has been improved significantly over the past several decades with the advancements of semiconductor techniques and the sensor technologies [1]-[4]. To enable the pervasive healthcare, the sensors need to monitor the health indicators such as respiration rate, heartbeat rate, blood core temperature, and detect the possible risky accidents like falling accurately in real-time [3]-[8]. Moreover, it would be promising to implement the imaging on *in vivo* objects with compact-sized devices, enabling the potential disease diagnosis in a portable or wearable way [44]-[52].

The chip-scale radar sensors can provide real-time high-resolution ranging and high-fidelity detection by transmitting the frequency modulated continuous waveform (FMCW) and detecting the micro doppler shift caused by the specific movements like falling or gestures, etc. [11]. The radar sensors leveraged the micro-doppler effect and implemented the imaging on motion, where the two-dimensional high-resolution

imaging of the target is processed for real-time monitoring [9],[10],[12]. Besides falling detection, the coherent radar sensors can be used to monitor the respiration rate or heartbeat rate by coherently processing the phase information.

Besides the integrated bio-radar sensors implemented for noncontact falling detection and multimodal vital signs monitoring, the photoacoustic effect has demonstrated its potential to monitor the blood core temperature and achieve *in vivo* imaging in a non-invasive way [45]. Moreover, there is a great need to bring efficient signal processing algorithms near the wearable sensors to achieve accurate sensing with ultra-low power (ULP) consumption. Portable PA sensors can be developed to ensure the non-invasive temperature monitoring and in-depth *in vivo* vessel imaging.

Nowadays, the sensor data is mainly processed by specific processing units like CPU, FPGA, DSP module, etc., which dissipates much power and has a high requirement on the devices' computation capability and is unsuitable for pervasive healthcare applications. For pervasive healthcare monitoring, the sensor data needs to be acquired and processed at the edge near the sensor node, requiring real-time processing with low power consumption. The specific waveform patterns related to health status need to be extracted and recognized accurately in real-time. In the thesis, CMOS-integrated radar sensors are used for noncontact locating, monitoring on specific movements like falling, detection on multimodal vital signs like respiration rate and heartbeat rate. Moreover, the chip-based photoacoustic sensors are deployed in a portable or wearable way to enable the non-invasive monitor physiological signs and diagnose diseases based on the specifically featured PA waveforms [45],[46].

Through the optimizations on CMOS-integrated radar sensors, chip-based photoacoustic sensors, novel transducer design, and efficient sensor data processing algorithms, the continuous personalized pervasive healthcare monitoring and potential

disease diagnosis with low power consumption, compact size, high accuracy, and high specificity can be achieved.

1.2 Objectives

This research aims to solve the critical issues in the design of CMOS-integrated sensor circuits and systems for pervasive healthcare monitoring and potential disease diagnosis in the incoming Internet of Everything (IoE) era. Firstly, a CMOS-integrated phased-array radar sensor was implemented for the compactness and robustness of the multimodal vital sign monitoring and falling detection in a wide field-of-view (FoV). Secondly, the Vernier-based delay-locked loop (DLL) which enables the wide-bandwidth beam steering with wide steering range and fine steering step. Thirdly, the low-power analog front end (AFE), the photoacoustic transducer, and coherent detection techniques have been implemented to enable a compact-sized wearable photoacoustic sensor for blood temperature monitoring and *in vivo* vessel imaging. Fourthly, a four-channel photoacoustic system-on-chip (SoC) has been implemented, including the AFE, ADC, DAC, and the coherent processing module on-chip. The SoC enables accurate beamforming, coherent lock-in on target photoacoustic signals, and highly precise reconstruction on the target signal masked under interferences and noise, allowing the highly precise vital signs sensing and biomedical imaging. Fifthly, MEMS-based ultra-low-power (ULP) frequency shift keying (FSK) receivers are implemented to enable highly efficient short-range communication between biomedical sensor nodes.

1.3 Major Contributions of the Thesis

To achieve accurate non-invasive healthcare monitoring and disease diagnosis, synergetic optimizations on circuits, sensors, and efficient signal processing algorithms

need to be implemented. In the intricate, dynamic, resource-constrained, and noisy scenarios encountered in the real world, current sensor approaches face the limitations on the accuracy, power consumption, and size, etc. To address such limitations, the thesis presented several highly integrated chip-based mixed-signal sensor systems for adaptive and accurate multimodal vital signs monitoring, specific movements detection, and imaging, which include: 1) CMOS-integrated radar sensors for multimodal vital sign monitoring and falling detection; 2) a chip-based mixed-signal coherent photoacoustic sensor system for accurate blood temperature monitoring and *in vivo* imaging; 3) a 4-channel photoacoustic sensor SoC with I/Q based coherent detection for early-late loop tracking and highly accurate imaging; 4) a MEMS-based ultra-low-power (ULP) FSK receiver for highly efficient short-range communication for internet-of-everything (IoE) devices.

A series of work on CMOS-integrated radar sensors and chip-based photoacoustic sensors aiming at realizing the seamless pervasive healthcare sensing is presented, where the phased-array chip-scale radar sensor is deployed in the room to monitor multimodal vital signs continuously, and the chip-based photoacoustic sensors are designed in a compact size to enable the portable disease diagnosis and physiological signs monitoring, where the work from 9 paper(s) published in the following prestigious peer-reviewed journal(s) and conferences are listed. Among which, I am listed as the first author in 2 prestigious IEEE transactions. The phased-array radar sensor for multimodal vital sign monitoring published in IEEE T-MTT, and the mixed-signal based photoacoustic sensor published in IEEE T-BioCAS. My work has also been published as three first-author conference papers, including 3 ISCAS papers and 1 SOCC paper. I am listed as a co-corresponding author in 1 SOCC paper, where the presented radar sensor was used for motion detection. The thesis presents the critical ideas initiated by

me on implementing the coherent I/Q detection and multi-channel beamforming towards improving the signal-to-noise ratio (SNR) based on the SoC, which will lead to further publications in prestigious IEEE journals and conferences.

To conclude, the thesis presented the key innovative ideas and the explicit implementations of the CMOS-integrated radar sensors for multimodal vital signs monitoring. Also, a series of chip-based photoacoustic sensor circuits and systems are presented, which have demonstrated their capabilities on continuous temperature monitoring, multimodal vital signs monitoring, and *in vivo* vessel imaging for healthcare monitoring as well as potential disease diagnosis.

1.4 Organization of the Thesis

The remainder of the thesis is organized as follows.

In chapter 2, the literature review on biomedical sensor systems for pervasive healthcare is presented, which includes various kinds of CMOS-integrated radar sensors for multimodal vital sign monitoring, falling detection, and related algorithms for physiological feature extraction. Moreover, the photoacoustic and ultrasound sensors for temperature monitoring, physiological signs monitoring, and imaging are reviewed.

Chapter 3 demonstrates an X-band CMOS-integrated phased-array radar sensor for wide field-of-view (FoV) locating and multimodal vital sign monitoring, including radar front-end for noncontact signal detection and the interferometric time-phase analysis (ITPA) method for accurate vital sign monitoring in the phase domain. The two-stage beam steering technique enabled by the DLL and phase shifter on-chip is presented, by which the wide FoV detection can be realized. The experimental verifications and the discussions are given. A Vernier delay-locked-loop (DLL) design is demonstrated for the wideband beam steering with fine resolution, containing the circuit blocks, test

results, and the related analysis of the DLL for the chip-scale phased array radar sensor. Moreover, chip-scale Ku -band radar sensors are demonstrated for respiration monitoring and falling detection, including the transceiver front-end and the interferometric phase algorithm for respiration and falling pattern extraction. Moreover, the Ku -band radar sensor was leveraged to recognize the gestures based on the Doppler effect, exploring its potential usage in a noncontact seamless human-machine interface. Furthermore, an I/Q based coherent radar sensor architecture is proposed for tiny movements detection. The experimental verifications and the discussions are presented.

Chapter 4 demonstrates the design of a chip-based photoacoustic sensor, which includes the research on the low-power analog front end (AFE), the photoacoustic sensor, and coherent detection techniques for enabling a compact-sized wearable or portable PA-based healthcare solution. The system testing setup and experimental results on blood temperature monitoring and *in vivo* vessel imaging are fully presented. A four-channel photoacoustic system-on-chip (SoC), which has been designed, including AFE, ADC, DAC, and coherent processing on-chip. The SoC enables accurate beamforming, coherent lock-in, and early-late tracking on target photoacoustic signals, and highly accurate reconstruction on the masked signal in interference and noise, where the enhanced sensing and imaging can be enabled. The system demonstration and key circuit blocks, including the DAC and multiplier, are discussed explicitly.

Chapter 5 presents the conclusion, discusses the potential challenges and recommends future research toward fully enabling the pervasively connected, highly efficient, personalized healthcare system with CMOS-integrated biosensors and MEMS-enhanced ULP communications circuits and systems design.

Chapter 2

Review of the Bio-Radar Sensor and Photoacoustic

Sensor Techniques

To achieve the compact-size healthcare sensor system, innovations on the integrated circuits, systems, and algorithms are required. Radar sensors and photoacoustic sensors are the promising techniques, where the chip-scale radar sensor is used for noncontact multimodal vital sign monitoring, and the photoacoustic sensors are used for noninvasive physiological signs monitoring. Moreover, highly efficient and effective signal processing methods are required to enable the high specificity and sensitivity for feature recognition realized near-sensor. Section 2.2 reviews general radar sensor techniques for healthcare monitoring, where the section 2.2.1 reviews the biomedical radar techniques and section 2.2.2 reviews on the algorithms for radar data processing to realize specific movement detection, multimodal vital signs detection, and localization. Section 2.3 reviews the circuits and systems techniques for photoacoustic sensor applications, which can realize in-depth blood core temperature monitoring and *in vivo* imaging. The summary of the review is presented in Section 2.4.

2.1 Biomedical Sensor Techniques for Pervasive Healthcare

With the rapid development of integrated circuit and efficient signal processing techniques at the edge, compact-size biosensors are expected to be deployed massively in the future to achieve seamless and efficient monitoring on the subjects. There are several types of sensor techniques in use for indoor healthcare monitoring. An acoustic system uses microphones to detect vibrations that indicate a fall, which is implemented

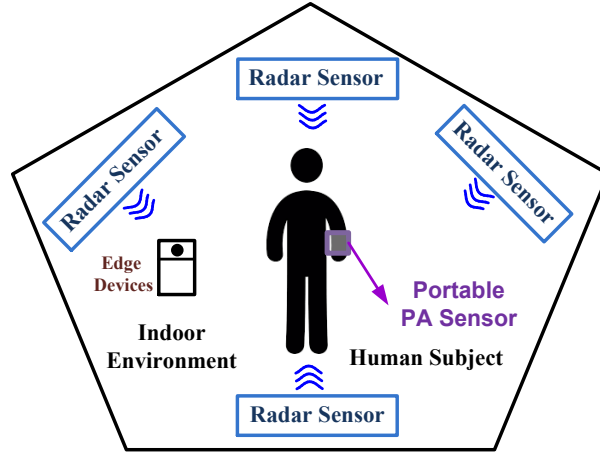


Fig 2.1. Illustration of the proposed pervasive healthcare monitoring solution enabled by noncontact radar sensors and portable noninvasive photoacoustic sensors.

in a relatively noncontact way [16]. However, it is not as effective as other technologies on detecting fallings considering that the accuracy is limited with the acoustic wave. A visual system is effective where the monitoring camera is deployed in various positions to identify the falling in a wide field of vi. However, this method may lead to the invasion of privacy to the users. Also, physiological signs such as respiration rate and heartbeat rate cannot be monitored by the camera. Moreover, the cameras can only monitor the condition within its view, which is easily affected by the possible obstacles existing in the scenarios.

Compared to the sensor techniques based on acoustic or camera. The radar sensor has demonstrated its capability on detecting specific movements like falling and monitoring vital signs like respiration rate and heartbeat rate. By leveraging the micro-doppler effect and imaging, which will generate a two-dimensional high-resolution image of the target, the accurate monitoring of the falling's dynamic process can be detected [14],[15],[17],[43]. Compared to the visual system, the radar-based solution is not intrusive on privacy, and it is much more accurate on movement detection. By transmitting the FMCW waveforms, radio frequency (RF) radar sensors can enable real-

time high-resolution ranging and high-fidelity detection in various kinds of scenarios where the micro-Doppler shift is detected and the corresponding imaging induced by specific movements like falling is obtained [18], [19]. The micro-radar sensor for fall detection and prevention is easy to implement under various room conditions, which is demonstrated in Fig. 2.1 and can protect privacy by only detecting the signs related to the ongoing falling process such as gaits variations [15].

The rapid development of integrated circuit techniques pushes sensor systems' transition from being realized in bulky size by discrete components to the portable or wearable way enabled by mixed-signal ICs. The photoacoustic (PA) effect demonstrates the enormous potential for the continuous sensing of in-depth blood core temperature as the optic and ultrasound sensing methods are combined to enhance the accuracy and specificity for accurate in-depth *in vivo* imaging and accurate physiological signs sensing [45]. The sensor transmits near-infrared (NIR) and middle infrared (MIR) light into the target blood vessel, which will absorb the light energy and generate specific acoustics waveforms [51]-[55]. By detecting the generated acoustic signal by the transducer, the blood core temperature monitoring and the vessel imaging are achieved.

Through the synergetic combination of the noncontact CMOS-integrated radar sensor and chip-based photoacoustic sensors, the pervasive healthcare monitoring can be achieved; the proposed scenario is demonstrated in Fig. 2.1, where the wearable PA sensors will continuously monitor physiological parameters related to health statuses, such as in-depth blood core temperature, blood glucose level, and oxygen saturation (SO₂). Moreover, the continuous *in vivo* vessel imaging can also be achieved for potential disease diagnosis based on the chip-scale mixed-signal PA sensor IC. The CMOS-integrated radar sensor systems can be implemented in different locations to

realize the noncontact multimodal vital signs monitoring, falling detection, and potential gesture recognitions for cognitive human-machine interfaces with a wide FoV coverage.

2.2 Introduction to Biomedical Radar Sensors

The respiration and heartbeat rates are essential biomedical metrics, which can be used for various kinds of applications, including personalized healthcare, early-stage disease diagnosis, baby monitoring, elderly care, etc. Currently, most commercial cardiopulmonary activity monitoring devices are realized in a contact way where pads are attached to the skin, which is inconvenient for the people. To overcome the limitations of inconvenience, radar sensors demonstrate the potential for monitoring multimodal vital signs in a non-contact way. The vibration of the chest caused by cardiopulmonary activities will modulate the phase of the transmitted EM signal. The information such as respiration and heartbeat rates can be extracted by specific signal processing at the receiver. After demodulation and filtering, the features related to cardiopulmonary activities can be attained [2], [4]-[15].

For typical biomedical monitoring scenarios, radar sensors need to detect the target subjects in a few meters range; such radar sensor systems need to be realized in a compact size with low power consumption to enable the long-time operation. Thanks to the development of semiconductor techniques, CMOS-integrated radar sensors have demonstrated the potential to meet the IoE healthcare monitoring requirements with low cost and easy deployment [26]-[31].

2.2.1 Comparison of Radar Sensor Architectures

In general, radar sensors can be categorized as narrowband Doppler radar [105], [116], frequency modulated continuous wave (FMCW) radar [106], [110], [114], [115],

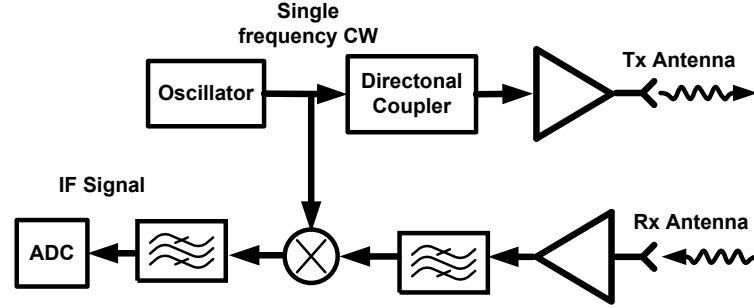


Fig. 2.2. Block diagram of a single frequency CW radar.

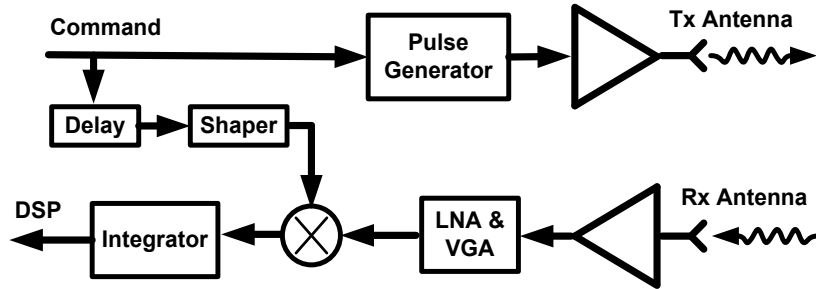


Fig. 2.3. Block diagram of the UWB radar.

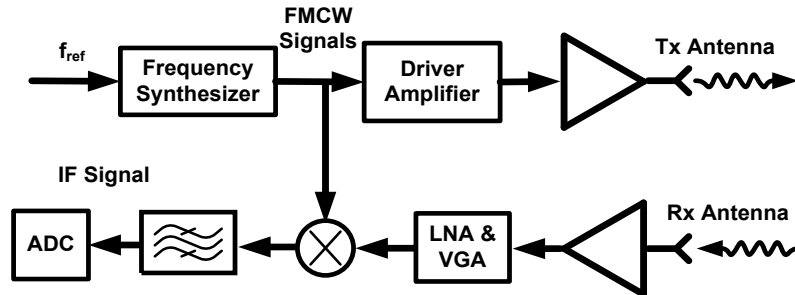


Fig. 2.4. Block diagram of the FMCW radar.

and ultra-wideband (UWB) radar [107]-[109], [111], [112], [118]. The block diagram of the single-frequency continuous wave (CW) radar is shown in Fig. 2.2, where a continuous sinusoidal wave generated from an oscillator with a constant frequency is transmitted toward the target. The returned signal contains the micro-doppler induced frequency shift proportional to the corresponding physiological micromovements such as heartbeat and respiration, or macro movements like falling or specific gestures. The demodulation of these doppler induced frequency shifts or phase differences at the receiver can be used to extract the heartbeat and respiration rate information [15]. The

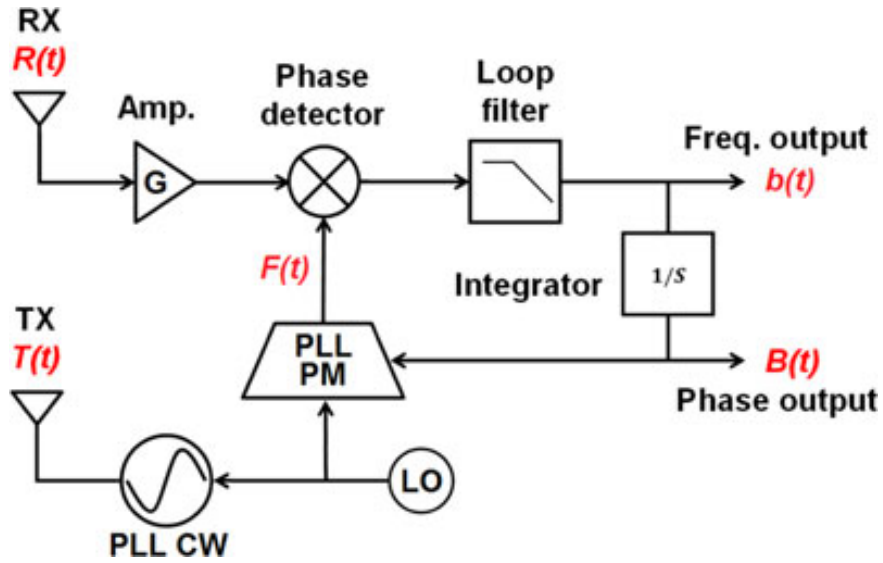


Fig 2.5. Schematic of a continuous phase tracking radar [105].

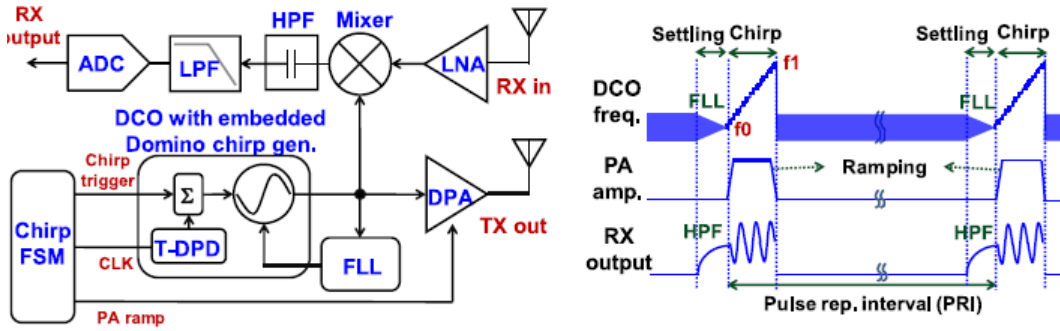


Fig 2.6 Schematic of a burst-chirp UWB radar sensor [107], [119].

CW biomedical radars for vital sign detection primarily used phase-locked oscillators due to better phase noise [2], [3]. The development of range correlation theory makes free-running oscillators applicable only for short-range vital signs monitoring because the signal-to-noise ratio (SNR) will degrade rapidly with the increasing of the detection distance [4]. Moreover, the flicker noises from the mixers in the conventional Doppler radar receiver further degrade the detection sensitivity [5]. The major limitation of the CW radar is that it cannot realize the range detection; thus, it is unavailable to achieve the localization on the subject. The detection of the Doppler frequency shift has found usages in weather sensing, positioning, life detection for rescue, cardiopulmonary

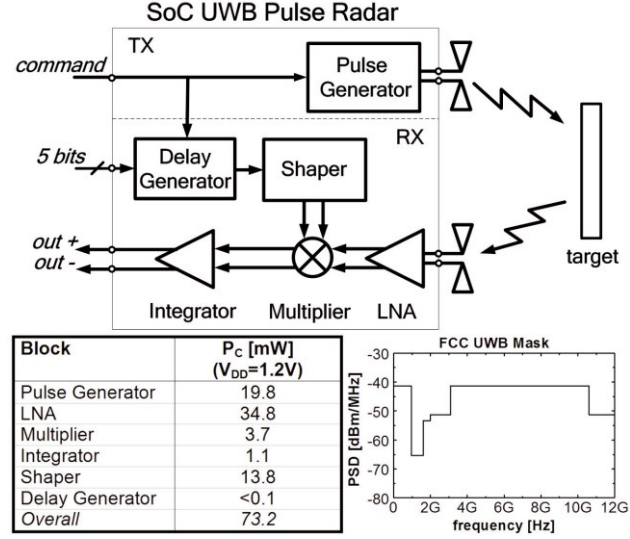


Fig 2.7 Schematic of an SoC UWB pulse radar sensor [28].

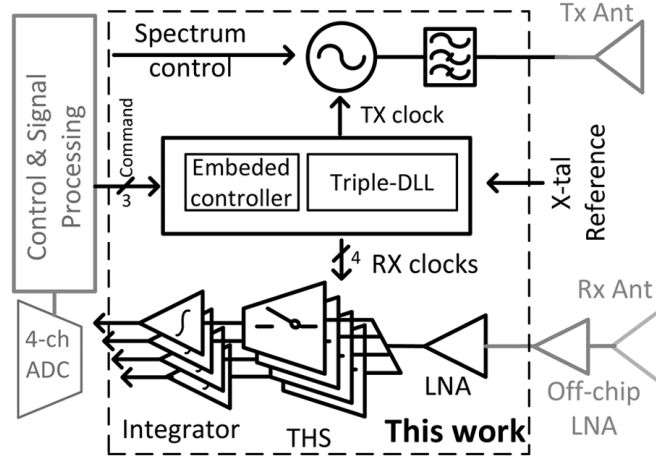


Fig 2.8 Schematic of an impulse radio radar sensor for vital sign monitoring [26].

monitoring, and human vital signal detection such as heart rate, respiration rate, throat movement, and vessel flow, etc. [1]-[4], [26], which is useful for the scenarios such as surgery, rehabilitation, and home healthcare.

An alternative approach is to employ the UWB pulse to monitor the heartbeat and breathing [28]. The block diagram of the narrowband CW radar is shown in Fig. 2.3, where the transmitter sends very short and repetitive pulses toward the chest. The echoed pulse will be received by the receiver and has a round-trip time delay with respect to the transmitter pulse. The receiver will then capture this delay time that is proportional to the movement of the heartbeat and breathing. Obviously, this time delay is also

sensitive to micro-movements of the subject, the tiny displacements induced by respiration or other physiological movements can be extracted accurately by the coherent processing on the echoed signals at the receiver [22]-[24]. Moreover, phased-array radar sensors demonstrate capability on high-resolution imaging [31], [126].

A phase tracking CW radar sensor for noncontact respiratory and heartbeat monitoring has been developed by IMEC, the architecture of which is shown in Fig. 2.5, where the phase-locked loop (PLL) is leveraged to achieve accurate phase tracking. The reflected signal from the chest-wall is with phase modulation proportional to the micro-movement caused by heartbeat or breathing movements of the chest wall. Through the demodulation of this phase in the receiver, the heartbeat rate and respiration rate signal can be recovered [26]. However, it needs to assume that the body is not moving. When the body moves relative to the transceiver direction, the Doppler frequency shift is decided by both the macro movements and micro-movements like heartbeat or respiration, leading to the inaccuracy of vital signs monitoring [27]. The effects caused by body movements can be calibrated by further digital signal processing.

A UWB chirp-based chip-scale radar sensor for vital signs monitoring has been presented by IMEC [107], [119], where the digital controlled oscillator (DCO) with embedded Domino chirp generation is used for fast chirp generation [28]. The transmitted pulsed chirp signal and the receiver output signal are shown on the right side of Fig. 2.6. The received echoed radar signal is processed by the de-chirping, filtered by both the high-pass filter and low-pass filter, and digitized by the ADC. An SoC UWB pulsed radar sensor is presented by University College Cork, Ireland, the diagram of which is demonstrated in Fig. 2.7, where the pulse generator transmits the pulses, and the received signal is processed by coherent mixing and integration by the AFE of the receiver. The system can achieve ranging and respiration monitoring. A 4-channel

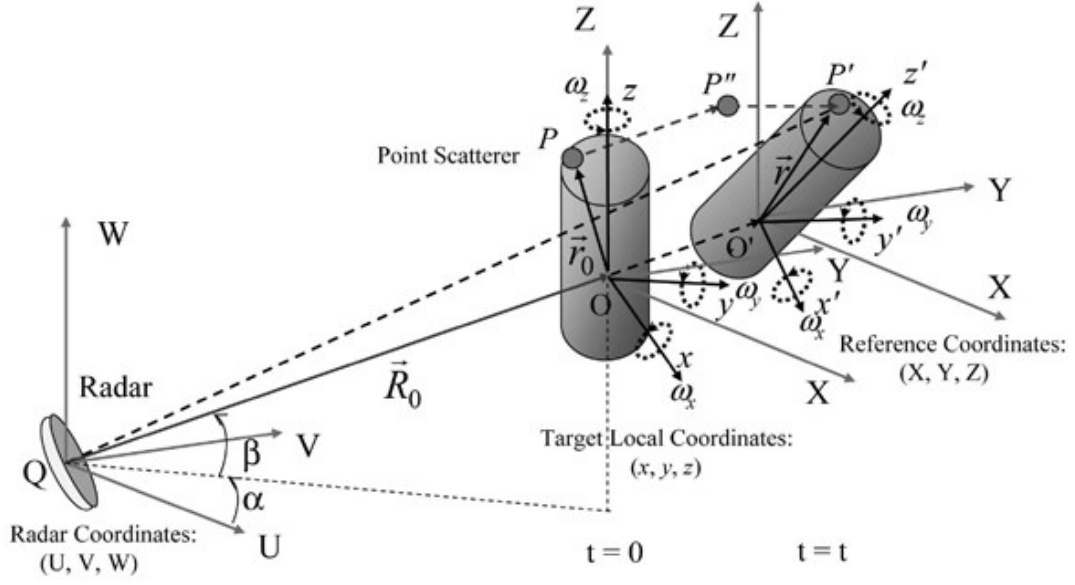


Fig. 2.10. Geometry of radar and target with translation and rotation [42].

sampling CMOS impulse radio radar sensor was developed by Electronics and Telecommunications Research Institute, Korea, which is illustrated in Fig. 2.8, where the transmitter, the 4-channel receiver, and the embedded digital control module are integrated on a single chip. The system can achieve improved SNR by the multi-channel sampling; moreover, a 100-ps resolution can be enabled by the triple-DLL [28].

A highly integrated 6-channel FMCW radar sensor with the antenna-in-package for gesture recognition and short-range communication has been developed by Google and Infineon Inc [106]. The diagram is illustrated in Fig. 2.9, where the RF front end, analog front end, serial peripheral interface (SPI), and sensor control units are integrated on-chip. Moreover, the high bandwidth communication can be achieved simultaneously with the radar. The patch antennas at the receiver have a combined antenna gain of around 10 dBi, while each transmitter antenna is with a gain of about 6 dBi. The transceiver on-chip contains an integrated VCO wide tuning range, which achieves a measured phase noise lower than -80 dBc/Hz at 100 kHz offset. The acquired radar

signal is further processed by the artificial intelligence (AI)-assisted algorithms in the digital domain to achieve precise gesture recognition and classification [106].

2.2.2 Radar Signal Processing Methods for Healthcare Monitoring

It is observed that the Doppler frequency shift will happen when the objects move away or toward the radar. However, if the target or any structure on the target has micro vibration or rotation in addition to its bulk transition, as shown in Figure 2.10, it will induce a frequency modulation on the returned signal. From this modulation, sideband signals are generated from the main bulk Doppler frequency shift, which is called micro-Doppler shift. Here the total Doppler frequency shift can be represented as $f = \frac{2f}{c} [\vec{V} + \vec{\omega} \times \vec{r}]_{radial}$ where \vec{V} , $\vec{\omega}$, and \vec{r} represent translation velocity with respect to the radar, rotation angular velocity, and range location, respectively. The first term is the Doppler shift due to the translation, and the second term is the micro-Doppler due to the rotations of the object [42]. The accurate expression for the induced micro-Doppler frequency due to the different micro-movements such as rotation, vibration, tumbling, etc. can be rigorously derived. Generally, the returned signal phase includes the information of the distance between the radar and the object, radical velocity, and micro-Doppler frequency shift caused by movements. The Doppler effect is used to realize the detection and recognition of the falling. Although multiple dimension parameters can be detected and estimated, the complexity of the system configuration and signal processing increases greatly with many high-speed high-power circuits, making real-time monitoring more difficult and less accurate. To reduce the power consumption and improve the accuracy, the coherent detection FMCW radar sensor enabled by the on-chip frequency synthesizer and mixer is usually used.

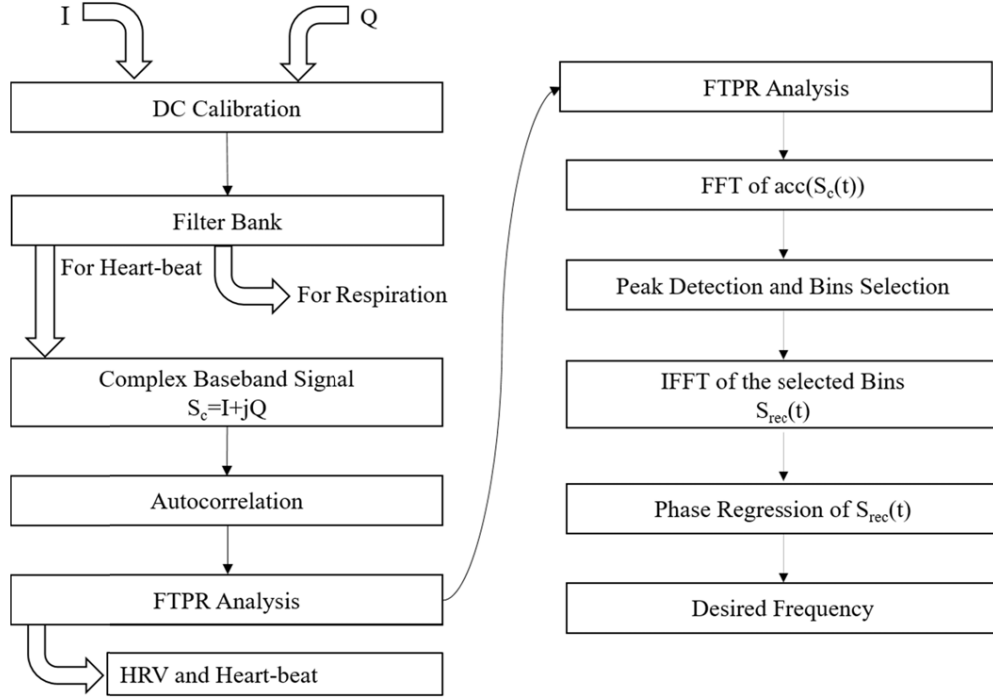


Fig. 2.11. Flowchart of the presented method leveraging FTPR algorithm for heartbeat detection [6].

For accurate tiny movements monitoring, such as detecting the heart rate variation, specific algorithms need to be developed to extract the weak target signals. In [6], the Gaussian pulse train model and frequency-time phase regression (FTPR) algorithm are leveraged to detect heart rate variability. The flowchart of the algorithm is demonstrated in Fig. 2.11. The recorded in-phase (I) and quadrature (Q) channels of the CW Doppler radar will be fed into a computer for processing. The dc offset cancellation is implemented at each channel, which will remove the dc component by subtracting their corresponding mean values from each of the I and Q signals. The I and Q signals are then passed through a filter bank consisting of a set of low-pass and bandpass filters. The data after LPF is used for respiration recovery. The data for heartbeat analysis is generated by the bandpass filtering of I and Q channels, which removes the breathing signal and the higher frequency noise signals. The filtered signals are merged to form a

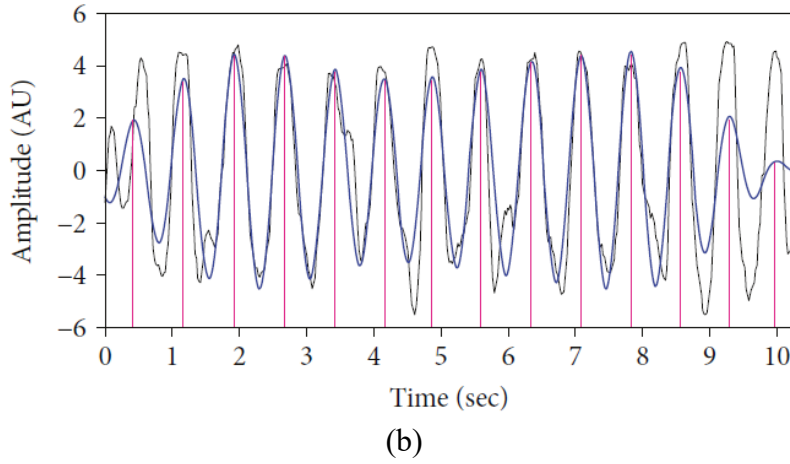
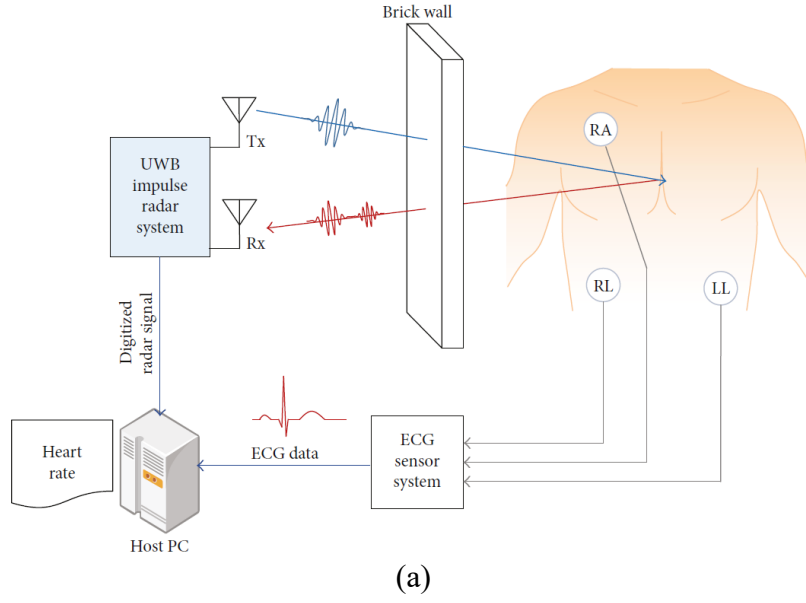


Fig. 2.12. (a) UWB experimental setup, (b) heartbeats restored from the PCA [109].

complex time-domain signal. The complex signal is then processed with the FTPR analysis, FFT on the complex signal's autocorrelation, peak detection, IFFT, and phase regression to obtain the desired frequency corresponding to the heartbeat movement [6].

The UWB impulse radar sensor can be leveraged for accurate heartbeat detection, where an experimental UWB setup is demonstrated in Fig. 2.12 (a) to realize healthcare monitoring through a wall. The principal component analysis (PCA) algorithm is leveraged to analyze the time series data and extract the heartbeat information through the phase variations in the time domain, where the recovered heartbeat waveform by the

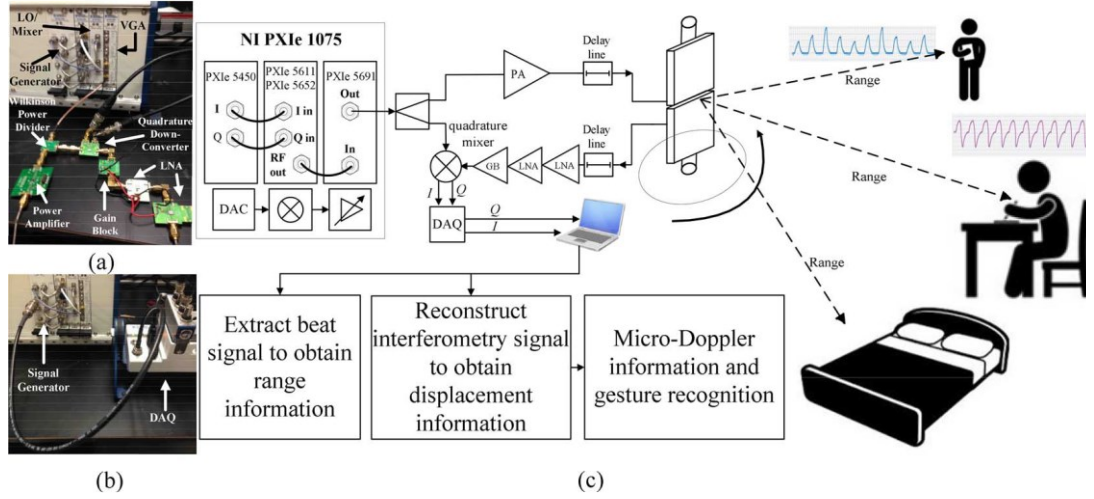


Fig. 2.13. (a) Photography of the radar hardware. (b) Synchronization module for the signal generator and DAQ. (c) Block diagram of the radar system and experimental setup [23].

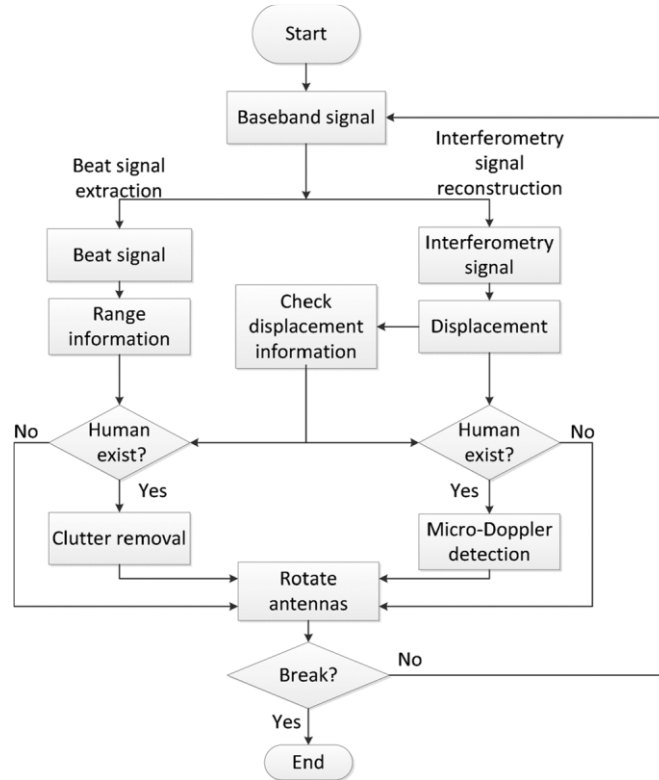


Fig. 2.14. The signal processing flow of the FMCW radar healthcare monitoring [23].

PCA algorithm is illustrated in Fig. 2.12(b) [109]. The impulse-radio UWB (IR-UWB) receiver can also be realized with time-correlator implemented by the analog technique, where at the receiver, the energy collected by the antenna is amplified by a low-noise amplifier (LNA) and a variable gain amplifier (VGA). Then the amplified signal with a

TABLE 2-1.
Comparison of Features of Different Radar Sensors

Feature	FMCW	UWB Pulse	Single Frequency CW
<i>Detection Accuracy</i>	High	Middle to High	Middle
<i>Ranging</i>	Long	Middle	No
<i>Localization</i>	Yes	Yes	No
<i>Frequency</i>	Flexible	FCC mask	High
<i>Doppler Detection</i>	Very Good	Good	Yes
<i>Tiny Motion Detection</i>	Excellent	Good to Excellent	Good
<i>High SNR</i>	Yes	No	Yes
<i>System Complexity</i>	Middle	Low to Middle	Low
<i>Power Consumption</i>	Middle	Low to Middle	Low

suitable level is passed through a time-domain correlator realized by mixer and integrator. The template generator is leveraged to realize the demodulation, relaxing the requirements of the constituent ADC and reducing the overall power consumption [111].

A typical FMCW radar sensing experimental setup for precise indoor localization and versatile life activity monitoring is illustrated in Fig. 2.13, where (a) demonstrates the board-level radar system realized based on commercial blocks, (b) demonstrates the synchronization setting for the signal generator and the data acquisition module (DAQ), and (c) shows the block diagram of the prototype hardware and the signal processing blocks for realizing ranging, tiny movement detection, and gesture recognition. Fig. 2.14 demonstrates the signal processing flow, starting from the baseband signal, the beat signal is used for ranging and the interferometry signal is processed to obtain tiny movements. The antenna is controlled to focus the beams on the target's direction.

The comparison and summary of the features of different kinds of radar sensors are presented in Table 2-1. Potentially, combining the advantages of the full bandwidth and the micro-doppler radar can detect tiny physiological signals with high range resolution as well as time resolution. The FMCW radar sensor realized by advanced CMOS

TABLE 2-2.
Summary of Chip-Scale CW and FMCW Radars

Properties		ISSCC 2019 [114]	ISSCC 2018 2018 [115]	TMTT 2020 2020 [116]	TMTT 2020 2020 [117]	JSSC 2016 [106]
Integrated Functions on Chip		Tx+Rx	Tx+Rx + Control Logic	Tx+Rx	MPS+Tx Array+Rx +SPI	DAC+Mixer+ Peak Detector+VC O+SPI+Frequency Divider+Mux +Buffer
Modulation Method		FMCW	FMCW	CW Doppler	FMCW	Sawtooth Modulation
Tx Output Bandwidth		13 GHz	4 GHz	n.a.	1 GHz.	1 GHz
Center Frequency		145 GHz	79 GHz	103 GHz	10 GHz	60 GHz
Antenna Type		On chip	In Package	Horn Antenna	Vivaldi Antenna	Patch Antenna
Technology		28-nm CMOS	45-nm CMOS	65-nm CMOS	65-nm CMOS	350nm SiGe
Power Consumption		500 mW	3500+ mW	262 mW	262 mW	900 mW
IF Bandwidth (MHz)		17	15	15	10	0.01-1
Active Channel		1Tx+1Rx	3Tx+4Rx	1Tx+1R _x	4Tx+1Rx	2Tx+4Rx
Beam-Steering Methodology		n.a.	n.a.	n.a.	Two-Stage Beam-steering	n.a.
Signal Processing Method		FFT	FFT	Filterin g & FFT	ITPA	Ranging/Com munication
Func ti ons	Localiza tion	n.a.	YES	n.a.	YES	YES
	Respirati on	n.a.	n.a.	YES	YES	n.a.
	Heartbea t	YES	n.a.	YES	YES	n.a.
	Hand Gesture	YES	n.a.	n.a.	YES	YES

techniques can be leveraged to enable real-time, accurate monitoring on multimodal vital signs like respiration rate or heartbeat, gaits, and accurate detecting on specific movements like falling based on specified algorithms processing in both the time

TABLE 2-3.
Summary of Chip-Scale UWB Radars

Properties		ISSCC 2010 [118]	JSSC 2014 [26]	ISSCC 2019 [119]	ISSCC 2011 [28]	JSSC 2017 [30]
Integrated Functions on Chip		Tx+Rx+SP I	Tx+Rx+ DLL+ Control Logic	ADC+LPF+ HPF+LNA/ Mixer+DC O+PA	Pulse Generator + Delay Generator + Shaper +LNA +Mixer+ Integrator	TX/RXFE+ ADC
Modulation Method		OOK/BPS K	UWB	Burst Chirp	UWB Pulse	UWB Pulse
Measured Tx Output Bandwidth		1 GHz	2 GHz	0.7-0.8 GHz.	n.a.	1.4 GHz, 1.5GHz
Center Frequency		4 GHz	4 GHz	6.8-8.2 GHz	2.8-5.4 GHz	7.29 GHz, 8.748 GHz
Architecture		UWB Impulse	Impulse Radio	Burst Chirp	UWB Pulse	UWB Pulse
Antenna Type		n.a.	Horn Antenna	n.a.	n.a.	n.a.
Technology		180-nm CMOS	130-nm CMOS	40-nm CMOS	90-nm CMOS	55-nm CMOS
Power Consumption		Tx: 0.92nJ/Bit Rx: 5.3nJ/Bit @1Mbps	25mW/C hannel	19 mW	73.2 mW	118 mW
Sensitivity (dBm)		-82 to -90	-70	n.a.	n.a.	n.a.
Active Channel		1Tx+1Rx	1Tx+4Rx	1Tx+1 Rx	1Tx+1 Rx	1Tx+1Rx
Signal Processing Method		Ranging & Communicati on	Fourier Transfor m	FFT	Ranging/Tra cking by DG and Integrator	Range- Doppler
Communicatio n Rate		1 Mbps	n.a.	n.a.	n.a.	n.a.
Func tions	Localiz ation	YES	n.a.	n.a.	YES	n.a.
	Respira tion	n.a.	YES	YES	YES	YES
	Heartb eat	n.a.	n.a.	YES	n.a.	YES

domain as well as in the spectrum.

The summary of the state-of-the-art chip-scale bio-radar sensors is shown in Table

2-2, where the critical parameters like bandwidth, carrier frequency, power consumption are presented [106], [114]-[117]. It is clearly demonstrated that the FMCW radar can achieve localization on subjects while it is hard for single-frequency CW radars. Moreover, FMCW radars can enable communication within the bandwidth simultaneously when operating for health sensing. With the increase of the center frequency, the antennas can be integrated in-package, further reducing the system's volume. To obtain the healthcare information, the received radar signal can be processed by FFT in the frequency domain as well as specific processing in time domain to attain real-time monitoring on heartbeat and respiration variability.

A summary of typical chip-scale UWB radar sensors is presented in Table 2-3, where the UWB frequency band is between 4 GHz to 9 GHz [26], [28], [30], [118], [119]. The impulse UWB architecture can be used for ranging and vital signs monitoring at the same time. Moreover, the UWB radar has the potential to realize communication with the FCC standard at the same time. It is promising to leverage the advantages of UWB and FMCW techniques to achieve precise localization and accurate multimodal vital signs monitoring at the same time based on one integrated radar sensor [28].

2.3 Photoacoustic Sensor Systems for Noninvasive *In Vivo* Physiological Signs and Imaging

Besides the radar sensors for noncontact multimodal vital signs monitoring and specific movement detection, portable biomedical applications like temperature monitoring and *in vivo* vessel imaging for potential disease diagnosis are required for pervasive health applications, where sensors leveraging multi-physical mechanisms are used. Photoacoustic and thermoacoustic effects refer to the acoustic generation induced by a pulsed electromagnetic wave, such as laser, microwave, or recently proposed

magnetic mediation due to the thermo-elastic characteristic [51],[52]. In the recent decade, the photoacoustic technique demonstrates its significant potentials for biomedical sensing and imaging applications. Although photoacoustic imaging could break through the optical diffusion limit by converting photons to ultrasound and sustaining high spatial resolution in deep tissue, the sensitive detection of the weak photoacoustic signal is a long-standing challenge, especially for deep tissue imaging [53]. Due to strong optical scattering and absorption, it is hard to achieve high energy conversion efficiency from optical to acoustic energy. Moreover, it is necessary to be implemented with strict ANSI safety standard limit ($<20 \text{ mJ/cm}^2$) [54].

A pulsed laser will illuminate the sample to induce the transient acoustic emission in a typical photoacoustic sensing system, which will be detected by ultrasound transducers. The photoacoustic effect can be leveraged to monitor various kinds of physiological signs non-invasively, showing the potential to be harnessed conveniently for pervasive healthcare monitoring and potential disease diagnosis in the IoE era.

2.3.1 Photoacoustic Principle

The photoacoustic effect refers to the acoustic wave generation of the tissue through the thermoelastic mechanism when illuminated by intensity-modulated light. As illustrated in Fig. 2.15, a pulsed laser illuminates the blood vessel that contains the target, such as red blood cells, to be detected. The target absorbs part of the laser energy, undergoes thermal expansion, and then launches acoustic waves detected by the external ultrasound transducer. The multi-wave sensing technique has shown its potential for various kinds of biomedical applications considering its capability to enable high-resolution in-depth *in vivo* imaging, which can detect the target in several-centimeter depth utilizing the rich optical characteristic. Moreover, the flexibility in configuring

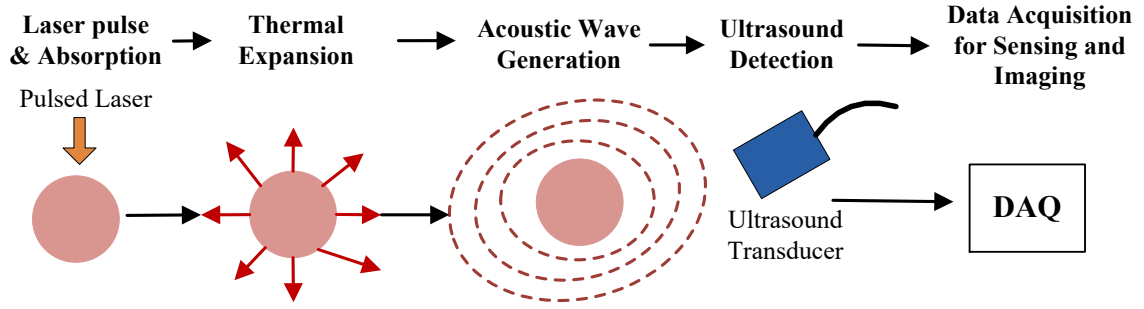


Fig. 2.15. Photoacoustic phenomenon and the sensing and imaging on target.

the photonic and ultrasonic parameters allow it to be customized in vastly different applications scenarios with target scales varying from organelles to organs and penetration depth from several millimeters for the superficial layer to the depth of several centimeters for in-depth *in vivo* tissue imaging and sensing [51]-[54], [68].

Nowadays, several kinds of photo-acoustics systems have been demonstrated. A functional photoacoustic microscopy system with compact size has been developed, enabling a 15- μm imaging resolution with a 3 mm penetration depth. The PA endoscopic probe with an outer diameter of 3.8 mm and an intravascular PA probe with an outer diameter of 1.2 mm was designed to realize the PA sensing and imaging with compact size and convenient deployment [51], [53], [55]. Moreover, a photoacoustic tomography system has been presented to achieve the *in vivo* imaging of a rat's whole brain with the skin and skull intact in a non-invasive way [58]-[60].

The spectroscopic nature of the PA effect can be further leveraged to quantify the concentrations of specific chromophores via their spectral signatures, where the spectroscopic measurement of blood oxygen saturation (SpO_2) can be achieved with high accuracy [62]. Also, the in-depth blood core temperature can be obtained by the PA sensing in a non-invasive way, demonstrating the potential to enable non-invasive and accurate temperature monitoring for COVID-19 disease diagnosis and monitoring.

2.3.2 Photoacoustic Sensor for Non-Invasive Temperature Monitoring

Non-invasive temperature measurement solutions generally depend on using various kinds of waves that can penetrate a material to sense specific physical parameters in a direct or indirect way. Different sensing mechanisms can be used, which include mechanical waves like ultrasound, electromagnetic waves like radiofrequency and light waves, and thermal waves [68]. Each sensing mechanism is with its own advantages and limitations. Portable and low-cost diagnostic ultrasound-based methods can penetrate deep into the human body and provide real-time temperature information. However, the accuracy of this method is limited due to its weak sensitivity to temperature. Magnetic resonance thermometry is currently the most accurate method in measuring *in vivo* temperature, considering its excellent detection sensitivity and high spatial resolution. However, it is only suitable for scenarios where the temperature variation is relatively slow due to the high cost and large size for generating the magnetic fields, preventing the usage in portable or wearable sensor applications with low cost and low power consumption. Infrared thermography can enable continuous temperature monitoring with better than 0.1 Celsius accuracy, but it can only sense the temperature at the surface of an object with a depth smaller than 0.5 mm. As pure optical methods are sensitive to tissue physiological parameters, including temperature, it owns the potential for temperature monitoring. However, the strong scattering of light within *in vivo* scenario precludes it from achieving high-resolution in-depth temperature monitoring on the carotid or pulmonary artery [68].

The methods mentioned above are all with significant limitations as they only leverage one specific physics sensing mechanism. None of them can enable heat strain monitoring, which is essential for *in vivo* temperature monitoring. Considering that photoacoustic sensors leverage the multi-physical sensing mechanism where the

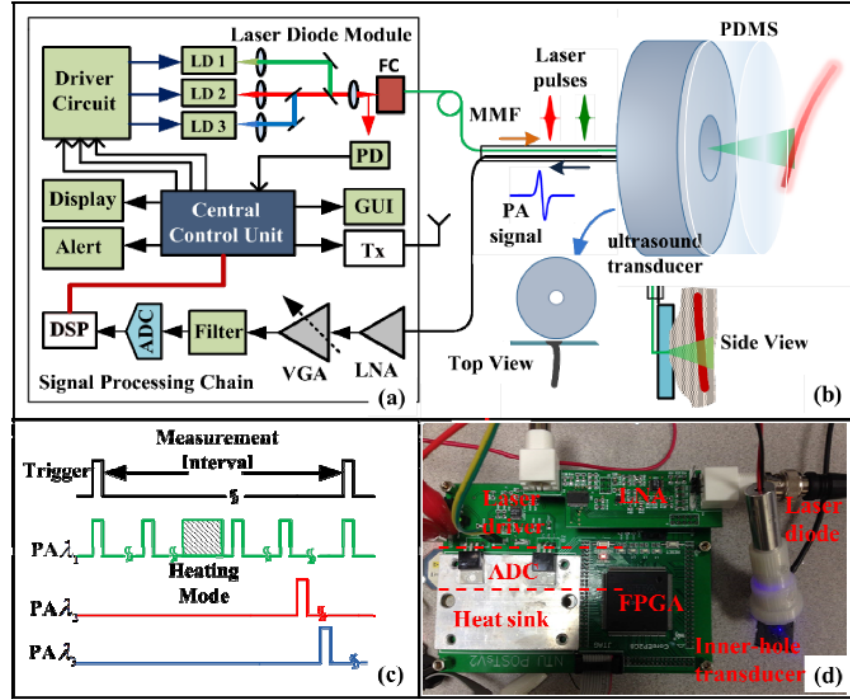


Fig. 2.16. Schematic of a typical photoacoustic sensing device for blood temperature. (a) Main body; (b) Sensor head (acoustic module and optical module) (c) Trigger signal and the PA response signals; (d) Final system setup and illustration of each part. FC: fiber coupler, LD: laser diode, MMF: multimode fiber, PD: photodiode, Tx: Transmitter, VGA: variable gain amplifier, LNA: low noise amplifier, DSP: digital signal processor, ADC: analog to digital converter [68].

advantages of both optical and acoustic are achieved. The high contrast and sensitivity are enabled by optical sensing while a fair resolution is achieved based on ultrasound sensing, enabling non-invasive in-depth blood core temperature measurement with excellent accuracy, which is promising for Covid-19 monitoring recently.

Several researches on photoacoustic temperature sensing in various applications scenarios like monitoring radio frequency (RF) ablation and high intensity focused ultrasound therapy, etc. The reported temperature measurements vary in accuracy and resolution, depending on the applications. The temperature in a single cell had been measured with an accuracy of 0.2-degree Celsius. A temperature monitoring system for cancer therapy can achieve 0.16-degree Celsius accuracy when ignoring the laser energy fluctuations. It was reported that an improved temperature sensitivity of 0.15 Celsius degree was obtained in a 2-second temporal step and 0.015 Celsius degrees by summing

Table 2-4.
Comparison of Features of Different Non-Invasive Temperature Monitoring Sensor
Types [68]

Technology	Penetration	Sensitivity	System Complexity	Power Consumption	Real Time
<i>Photoacoustic</i>	Middle to High	High	Middle	Low to Middle	Yes
<i>Ultrasound</i>	High	Middle	Middle	Low	Yes
<i>MRI</i>	High	High	High	High	No
<i>Pure Optical</i>	Low	High	Middle	Low	Yes
<i>Infrared</i>	Low	High	Low	Low	Yes

and averaging on the detected signals, while the temporal step is 200 seconds in this case. The measurement accuracy is highly scalable corresponding to the sampling periods. Table 2-4 demonstrates the comparison of features of different non-invasive temperature sensors. The main advantage of the PA sensor is its middle system complexity, low to middle power consumption, middle to high penetration, and the configurable accuracy to meet the requirements of various kinds of temperature monitoring scenarios [68].

A typical photoacoustic sensing system for blood core temperature monitoring is demonstrated in Fig. 2.16. The block diagram is illustrated in (a), the control unit is realized based on FPGA to set the laser driving circuit as well as process the received PA signals by the AFE formed by LNA, VGA, filter, and ADC [68]. The acoustic sensor and optical sensor are illustrated in (b), where the polydimethylsiloxane (PDMS) layer is used for coupling between the object and the sensor. The trigger signal and the PA response are demonstrated in (c). The system setup, including FPGA, laser driver, laser diode, and LNA are illustrated in (d). The whole system is realized by commercial blocks implemented on PCB; although it is claimed in [68] that the system is portable or wearable, there is still room to further reduce system's size using CMOS techniques.

2.3.3 Photoacoustic Sensor for *In Vivo* Imaging

Besides in-depth temperature monitoring and physiological signs sensing, another essential application of the PA sensor system is *in vivo* imaging. Nowadays, medical ultrasound imaging contributes to a more critical role in disease diagnosis and healthcare monitoring [44]-[50]. Compared to cross-sectional imaging techniques such as magnetic resonance imaging (MRI), X-ray-computed tomography (CT), and positron emission tomography (PET), etc., ultrasound imaging does not need the ionization process, which requires an expensive, bulky system to realize the function, and the ionization process is usually harmful to the human body. Compared to conventional US imaging system, the magnitude of the acoustic pressures induced by the PA effect is much smaller, where a typical clinical US scanner can produce focal peak pressures greater than 1 MPa while the PA-induced pressure amplitudes are typically less than 10 kPa; thus, the nonlinear acoustic propagation is avoided. The low PA pressure amplitudes also indicate fewer hazards compared to US exposure [68].

To miniaturize the volume of the imaging devices and avoid potentially harmful ionizing radiation, ultrasound technique is preferred to produce a real-time image output with a higher temporal resolution [1]. Moreover, with the development of software-based imaging techniques and the miniaturization of commercial electronics devices, nowadays, some kinds of ultrasonic sensor systems with compact sizes have been developed [45]-[50]. However, such a sensor system's overall cost is still high, considering that a commercial GPU, CPU, or FPGA is needed. To further miniaturize the volume and decrease the power consumption of the system, it is necessary to achieve the co-design and coordinated optimizations of the customized integrated circuit and systems with specific signal processing algorithms.

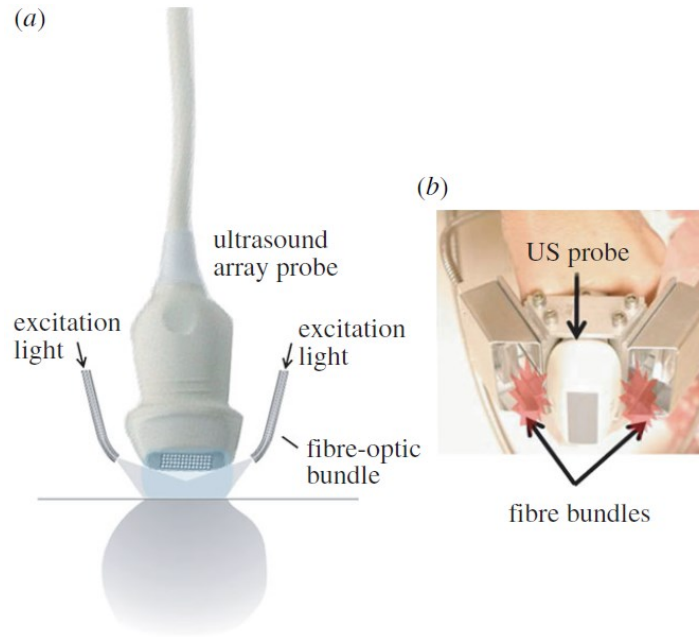


Fig. 2.17. PA imaging with ultrasound imaging probe. (a) Two-dimensional array probe and (b) Linear array probe for dual mode PAT-US imaging [89].

For PA or thermoacoustic imaging, modulated pulsed electromagnetic radiation is used to irradiate the target tissue and generate the ultrasound waves [51]-[54], where the optical wavelengths with the spectrum between 550 and 900 nm in the visible and near-infrared (NIR) part are usually used. The NIR spectral range 600–900 nm can provide the maximum penetration depth extending to several centimetres. By optical excitation, specific tissue chromophores such as haemoglobin, melanin, water, or lipids will absorb the optical energy and produce a rapid conversion to heat, which will induce a temperature rise of less than 0.1 K [89]. The temperature rise is well below the level that can cause physical damage or physiological changes. The heating induces the increase of pressure, accompanying the relaxation of the pressure, the emission of broadband low-amplitude acoustic waves within tens of megahertz frequency range, and less than 10 kPa pressure will occur. The acoustic wave will propagate to the surface and be detected by a mechanically scanned single ultrasound receiver or by a receiver array. Imaging can be formed directly or to be implemented with a reconstruction algorithm based on the back-projection method or multi-channel beamforming

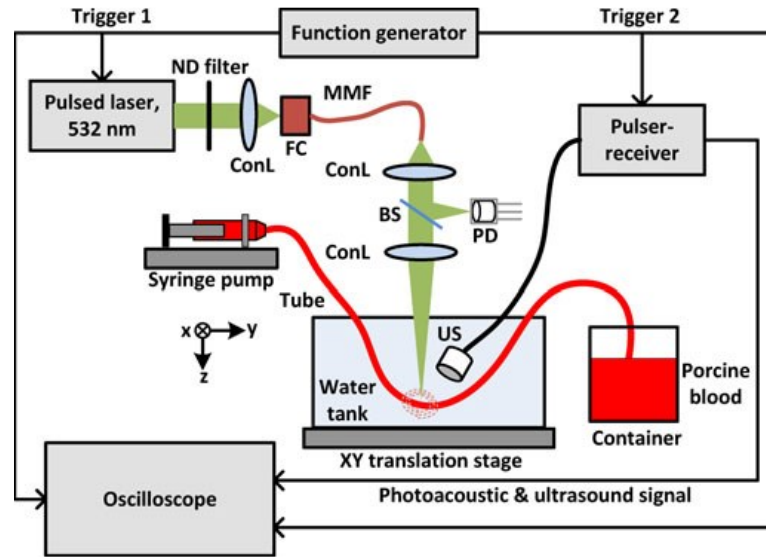


Fig. 2.18. Experimental setup of the coherent PAUS correlation and imaging. ConL, condenser lens; FC, fiber collimator; MMF, multimode fiber; ND, neutral density; BS, beam splitter; PD, photodiode; US, ultrasound transducer [58].

techniques [89], by which the resolution and contrast can be improved.

As sources of PA and US imaging are fundamentally different, the contrast of the constructed images is different. The US image indicates the mismatch of acoustic impedance between different tissues, where the contrast of the US image is determined by the mechanical and elastic properties of tissue. The PA imaging is determined by the initial distribution of the pressure induced by the exciting laser, reflecting the tissue's properties of optical absorption and scattering. A typical solution is to vertically offset the array from the tissue surface, fill the intervening space with an optically transparent acoustic coupling, then the laser light is delivered obliquely to the tissue surface beneath the array [89], the process is illustrated in figure 2.17(a). A linear array is used for two-dimensional imaging where the laser beams are delivered in orthogonal to the array's length axis. However, the requirement for a spacer puts a limitation on the dimensions of the two-dimensional array that can be used—the larger the area, the greater the required spacer thickness. Thus, the effective detection aperture and the image quality are decreased. Figure 2.17(b) demonstrates a specific implementation in which a

commercially available diagnostic linear array probe and a pair of fibre bundles are integrated to form a hand-held dual-mode US-PA imaging head. The system can realize real-time two-dimensional PA and US imaging at 10 frames per second and can enable relatively deep tissue imaging applications [89]. Furthermore, the PA imaging and US imaging can be leveraged in a synergetic way to enable the enhanced imaging performance, where a photoacoustic-ultrasound correlation coherent detection method was proposed in [58]. As demonstrated in Fig. 2.18, the PA signal and US signal are acquired and processed by a coherent correlation method, which is realized in an easy and relatively compact form based on commercial devices. However, the main limitation is that the system is built up based on discrete devices, leaving the room for further integration within a smaller volume and lower power consumption.

Figure 2.19 demonstrates a typical PA imaging technique, where the excitation light sources are implemented around the receiver so that the excited PA signals from all directions can be collected. The system reduces the large PA signal generated at the surface, usually obscuring the in-depth tissue signals. The system is implemented with a motor control system enabled by the personal computer (PC) and the DAQ. The x-y imaging of the scanned forearm is presented in Fig. 2.19(b) and (c). The vertical x-z slice image taken along the vertical line of Fig. 2.19(c) is shown in Fig. 2.19(d) [90].

Furthermore, 3D imaging can be achieved based on PA sensor systems where both the transducer and the excitation beam are mechanically scanned over a planar surface to detect the target. The transducer detects the induced PA signals, and the imaging is achieved at each step to generate a sequence of images. The PA signals are processed by rectification, envelope detection, spatially resolution, and is mapped to greyscale to realize three-dimensional imaging for disease diagnosis, such as identifying melanomas via the morphology and composition [90].

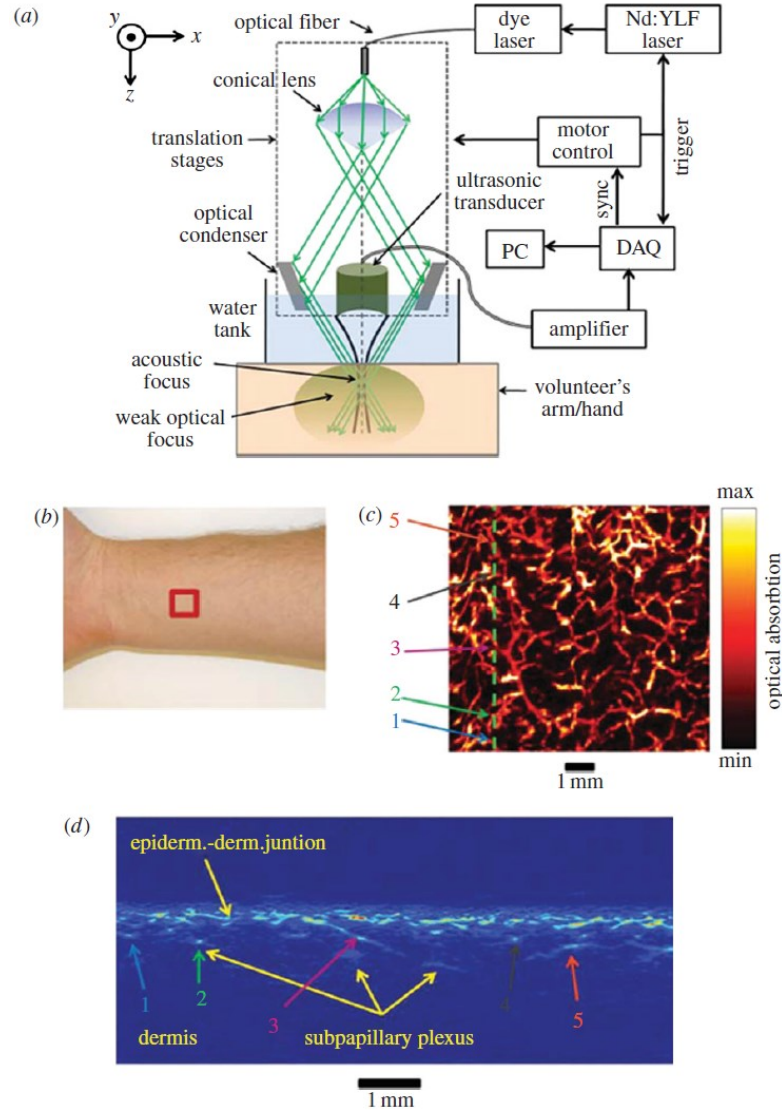


Fig. 2.19. Acoustic-resolution photoacoustic microscopy (AR-PAM) system for imaging the skin vasculature. (a) System schematic, (b) region of forearm scanned, (c) lateral x-y MIP image, (d) vertical x-z slice image taken along vertical line in (c) [90].

It also needs to be mentioned that FPGA can now support efficient backend processing for US imaging or PA imaging in a configurable and convenient way [113]. As demonstrated in Fig 2.20, a low-cost, compact, high-speed, and programmable imaging system based on FPGA is used for dual-mode forward-looking vascular US and PA imaging. Fig. 2.20 (a) demonstrates the PA/US system's schematic where the FPGA is used to control the laser, and the imaging process is achieved by the FPGA backend, where the system is implemented in the register-transfer level. The FPGA, ADC board, and CMU sensing front-end used in the system are demonstrated in Fig. 2.20(b) [113].

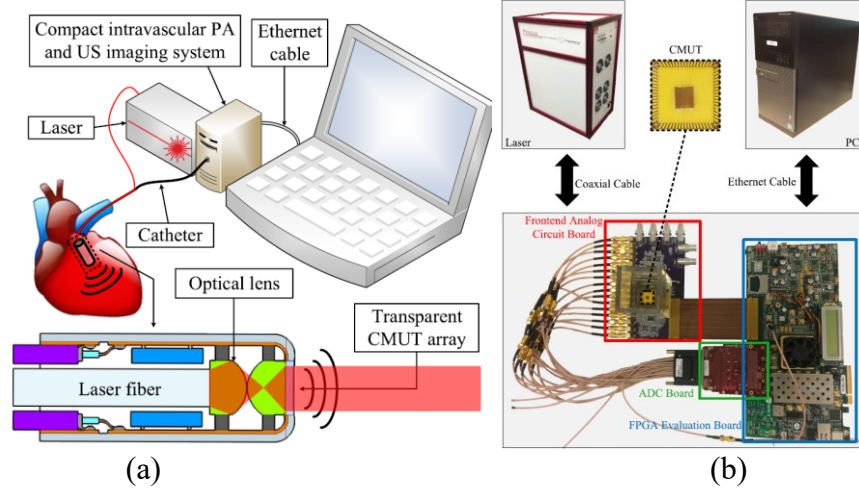


Fig. 2.20. (a) Compact PA and US system. (b) FPGA-enabled system [113].

2.4 Summary of Review

In this chapter, the design considerations and the challenges for the efficient compact-sized biosensors for the IoE era are presented by reviewing the papers on the radar sensors for noncontact health status monitoring and the photoacoustic sensor platforms for non-invasive physiological signs detection such as temperature monitoring, vessel imaging for potential disease diagnosis. Moreover, effective and efficient algorithms for sensor data processing are reviewed. The thesis will present a chip-based solution towards seamless pervasive healthcare monitoring and accurate potential disease diagnosis, leveraging the radar sensor and photoacoustic sensor's advantages. The CMOS-integrated radar sensors are deployed to monitor multimodal vital signs and detect specific movements like falling. The chip-based photoacoustic sensors are designed in a portable or wearable format for blood core temperature monitoring and *in vivo* vessel imaging, which is essential for the potential disease diagnosis. The healthcare monitoring with low power consumption and efficient near-sensor signal processing capabilities can be realized in an integrated edge sensing chip platform.

Chapter 3

CMOS-Integrated Radar Sensor Design for Multimodal Vital Sign Monitoring, Falling Detection, and Versatile Sensing

The aging of the world's population leads to increasing requirements for healthcare monitoring [1]. Through the global aging, chronic diseases are becoming the world's critical health problem; where, according to the World Health Organization (WHO), the number of deaths caused by cardiovascular diseases is estimated to be 17.9 million per year [1]. Continuous health monitoring meets the great interest of doctors and healthcare practitioners for a long time as physiological signs can be used as critical indicator disease conditions. Moreover, continuous monitoring of multimodal vital signs can be preventive to many severe life attacks [2], which is essential for the elderly or patients care. The vital signs related to abnormal respiration, heartbeat rate, and falling are expected to be monitored continuously to prevent possible disease-induced accidents, which are complementary to the clinical settings [2], [3]. In the COVID-19 pandemic, it is more essential to realize pervasive and convenient health status monitoring.

Among the possible sensor solutions for pervasive healthcare, considering that radar sensors are superior in detecting range and movements, it is suitable to be used to monitor various kinds of health indicators, including micro physiological signs like respiratory ailments [4], [5], heartbeat disorder [6], [7], and human activities like falling, etc. Moreover, as radar signals can penetrate through plastic, the radar sensors can be mounted behind a façade, enhancing the aesthetics of the solution for pervasive healthcare monitoring [7]-[9].

This chapter is organized as follows; the radar sensor techniques for healthcare applications are illustrated explicitly in Section 3.1. Section 3.2 describes the system architecture of the novel CMOS-integrated phased-array radar sensor and the algorithms used for subject localization and physiological signs monitoring. The accurate beam-steering (ABS) is enabled by the two-stage phase tuning at the transmitter (Tx), and the steered signal is transmitted via the Vivaldi antenna array. The interferometric time-phased analysis (ITPA) algorithm is implemented to monitor various kinds of physiological signs. Section 3.3 illustrates the experimental verifications of the system's capabilities to locate the subject, detect the falling, and monitor various physiological signs, including respiration rate and heartbeat rate at various beam-steering angles. Comparison and discussion are shown in Section 3.4. The 1TX-1RX *Ku*-band radar chip applications are explored in Section 3.5. A vernier DLL based clock generator design for phased array is demonstrated in Section 3.6. A mixed-signal *I/Q* based radar sensing method is discussed in Section 3.7. Finally, the summary is given in Section 3.8.

3.1 Chip-Scale Radar Sensors for Healthcare Application

As illustrated in Fig. 3.1(a), conventional healthcare sensors consisting of one-transmitter one-receiver radar need to be deployed at various positions to cover the wide monitoring angle range [10]. However, this method requires many radar sensors, introducing complex networking, over-sampled data, low efficiency, high power consumption, and high cost. Furthermore, it remains challenging to design a radar sensor that can be applied for ubiquitous health monitoring with a wide coverage range, low cost, compact size, and easy deployment.

In general, there are several kinds of radars for monitoring vital signs. For the narrowband Doppler radar technique, a continuous sinusoidal wave is sent to the subject

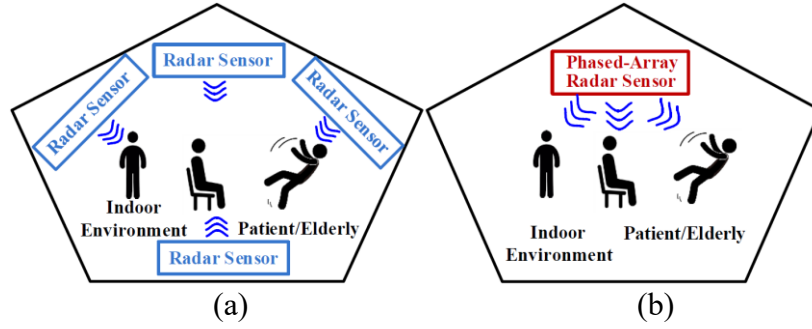


Fig. 3.1. Radar-based wide field-of-view health status and chronic disease monitoring: (a) Conventional radar sensors, and (b) proposed CMOS-integrated phased-array radar sensor [117].

person [11]-[13]. The reflected signal from the subject's chest surface contains the phase modulation, which is proportional to the micro-movements induced by heartbeat and respiration. Through demodulating this phase at the receiver, the vital signs like heartbeat and respiration signatures can be extracted and recovered [9], [12]. Another approach is to employ the ultra-wide bandwidth (UWB) pulses to detect the heart rate and breath rate by sending very short and repetitive waveforms toward the target person's chest surface [14]-[19]. The echoes will be received carrying a round-trip time delay proportional to the movement of the chest surface with respect to the transmitted waveform, which can focus on the phase information introduced by the modulated time delay, acquiring both high-resolution range profile and Doppler characteristics, enabling accurate multi-modal vital sign monitoring [20], [21], [35]. On the other hand, frequency-modulated continuous-wave (FMCW) radars are capable of monitoring various kinds of physiological signs, including heartbeat rate and respiration rate [22], [23]. Since the phase of the FMCW radar signal at the receiver is extremely sensitive to micro-movements of the subject, the tiny displacements induced by respiration or other physiological-relevant movements can be extracted and monitored precisely by processing the phase variations of the echoed signals at the receiver [22]-[24].

With the development of complementary metal-oxide-semiconductor (CMOS) technology, essential electronic components of the radars can be integrated into a single

chip [26]-[31], [92]. Radar sensors with a high-level integration can be embedded in a large quantity in the ceilings, walls or corners at various scenarios [25]-[27], boosting the cost-efficient noncontact solution for healthcare monitoring. Moreover, it is imperative to deploy the beam-steering technique to monitor the subjects, where the noncontact devices and algorithms are optimized jointly to enable the efficiency and effectiveness on healthcare monitoring in a wide field-of-view (FoV) [19], [31], [32], [36], [81].

Leveraging the advantages of the FMCW radar to enhance the spatial and temporal resolution for detection as well as the CMOS phased-array technique, a chip-scale phased-array radar sensor is presented, which is shown in Fig. 3.1(b). The radar sensor can achieve the localization on subjects, monitoring on physiological signs, and detection on falling within a wide FoV with low power consumption and compact size compared to conventional radar sensors realized by bulky and discrete instruments.

3.2 CMOS-Integrated Radar Sensor Design

For healthcare monitoring, considering the signals related to physiological signs are usually very weak, and some specific displacements need to be discerned accurately, a radar sensor with electronic beam control is preferable to align the beams to the subject, which enhances the signal-to-noise ratio (SNR) at the selected spatial direction [30]-[32]. Besides, the chirped signal transmitted by the radar is suitable for detecting the physiological signs with improved range resolution. Hence, the CMOS-integrated phased-array radar, which can generate a chirped waveform on-chip, is adopted to realize broad spatial coverage with fine steering precision. Fig. 3.2 demonstrates the architecture of the proposed CMOS-integrated phased-array radar sensor, where the four-channel transmitter and the one-channel receiver are integrated on-chip. Deep N-wells and metal fence walls are used as shielding wall to isolate RF building blocks from the substrate-

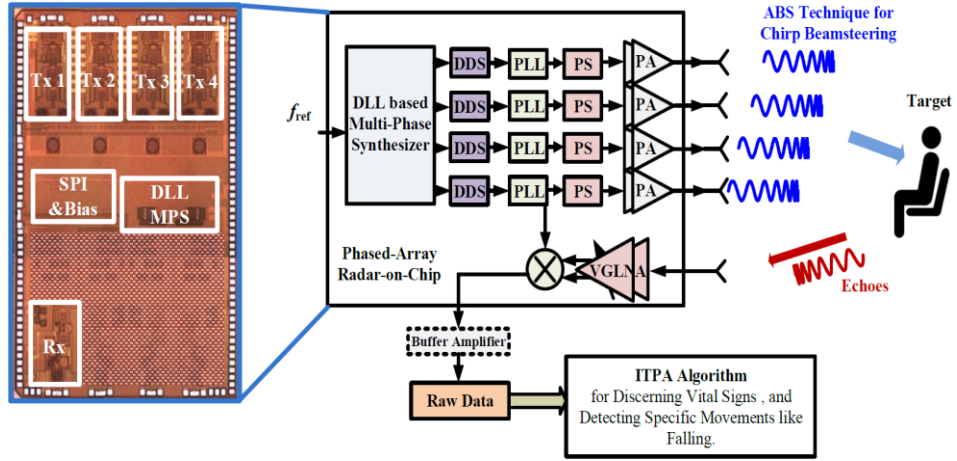


Fig. 3.2. CMOS-integrated phased-array radar sensor for vital sign monitoring and falling detection [117].

coupled noise. Combined with the ITPA algorithm, the chip-scale phased-array radar sensor can enable a high-performance solution on subject localization, multimode vital sign monitoring, and falling detection.

The CMOS-integrated phased-array radar occupies only 5.8 mm^2 silicon area and can cover 60° FoV with 740.7 mW power consumption. To generate fast chirp signal with high linearity, a DDS is typically adopted considering its open-loop nature for fast response. However, it normally works at low frequency from several tens to several hundred megahertz (MHz) with narrowband chirp for enabling the low power consumption [94], [95]. Therefore, the output frequency and bandwidth of DDS are multiplied by using a PLL-based chirp synthesizer converting it into the RF frequency range. By the phase control on-chip, the four transmitters send signals simultaneously with the coherent superposition; thus, the amplitude of the transmitted signal is enhanced. To obtain spectrally efficient chirps, transmitters need stringent linearity and low noise across the process corner, supply voltage, and temperature (PVT) variation.

X-band chip-scale radar sensors have been explored widely nowadays [96]-[103]. The broadband Vivaldi antennas are employed for transmitting and receiving the X-band chirped signals. By using the four-antenna array, the signal gain is enhanced by the array

factor. With the echoed waveforms from the subject being received, the coherent de-chirping is firstly performed to the signal. Then the de-chirped signal, which is coherent to the RF signal, is amplified by an intermediate frequency (IF) amplifier and processed by the ITPA algorithm to realize localization on the subjects, monitoring on various kinds of vital signs, and detection on the falling movements [104], [117].

3.2.1 Link Budget Analysis for the Proposed Integrated Radar Sensor

The link budget analysis for the radar system is illustrated in Table 3-1. According to radar theory [40], the returned power to the receiver antenna is expressed as

$$\frac{P_R}{P_T} = \frac{G_T G_R \lambda^2 \sigma}{(4\pi)^3 R^4 L_s} \quad , \quad (3.1)$$

where the estimated parameters are listed in Table 3-1. P_T and P_R represent the transmitted power and the power returned to the receiver antenna. G_T represents the transmitter antenna gain and G_R represents the receiver antenna gain. L_s is the term accounting for the total system loss, which is estimated to be about -5 dB. σ is the radar cross-section of the chest. The range R is 1.5 m, and the wavelength λ of the transmitted signal is 3 cm corresponding to the 10 GHz center frequency. The echoed power P_R is estimated based on the parameters in Table I and is calculated according to (3.1), which is about -70 dBm when detecting vital signs where the signal is reflected from the chest. The noise figure of the receiver is around 6 dB. Considering that the receiver bandwidth B is about 10 MHz, the thermal noise floor is estimated as [39]

$$P_n = -174dBm + NF + 10 \log_{10}(B) \approx -98dBm. \quad (3.2)$$

Table 3-1.
Link Budget Calculations.

Transmitter Output (P_T)	0 dBm
Center Frequency (f_c)	10 GHz
Tx Bandwidth (BW)	1 GHz
Rx Bandwidth (B)	10 MHz
Average Tx Antenna Array Gain (G_T)	12 dBi
Average Rx Antenna Gain (G_R)	8 dBi
Thermal Noise Floor (P_n)	-98 dBm
System Loss (L_s)	-5 dB
Radar Cross Section (σ)	-15 dBsm for the chest
* Received Power from Antenna (P_R)	Min: -70 dBm
Noise Figure (NF)	6 dB
De-chirping Gain (G_{De})	20 dB

*Estimated based on the distance of one-side range at 1.5m.

The compression gain of the de-chirping process realized by the mixer on-chip is estimated as $G_{De} = 10 \log(\frac{BW}{B}) = 20 \text{ dB}$. The gain G_{FE} of the receiver frontend, which is composited by the VGLNA and the mixer, is tunable up to 25 dB. A programmable gain amplifier (PGA) is employed after the mixer as an output buffer, which can provide a variable gain G_{IF} between 0 dB and 42 dB to boost the IF signal to a suitable level for further signal processing. The amplified de-chirped output signal P_D is estimated to be

$$\begin{aligned}
 P_D &= P_R + G_{FE} + G_{De} + G_{IF} \\
 &= P_R + (G_{VGLNA} + G_{mixer}) + G_{De} + G_{IF} .
 \end{aligned} \tag{3.3}$$

As the receiver frontend can provide the gain G_{FE} with 25-dB dynamic range, the de-chirping gain G_{De} is about 20 dB, and the PGA buffer at the receiver output can enable the gain G_{IF} with 30-dB dynamic range, the total gain provided by the receiver can be tuned to detect the minimum echoed signal P_R of -70 dBm. The echoed signal is amplified to around 0 dBm by the tunable receiver frontend and the buffer amplifier.

3.2.2 Accurate Beam-Steering Technique for the Subject Localization in a Wide Field-of-View (FoV)

The ABS technique is realized by the two-stage beam-steering in the CMOS-integrated phased-array radar. Based on the architecture illustrated in Fig. 3.2, the two-stage beam-steering is achieved by configuring both the true-time delay in the delay-locked loop (DLL)-based multiphase synthesizer (MPS) as coarse-tuning and phase delay in the RF phase shifter as fine-tuning [30]. In the MPS, two DLLs are used to lock for the cell delay of ΔT_{d1} and ΔT_{d2} , respectively, by setting the corresponding number of voltage-controlled delay cells (VCDCs), which is illustrated in Fig. 3.3 (a). The control voltages of the VCDCs of two DLLs, V_{c1} and V_{c2} , are used to tune the two groups of identical VCDCs in the Vernier delay matrix as the ones in DLLs to generate the true-time delay. Hence, four channels of reference clocks with delay difference of ΔT_{MPS} (i. e. $\Delta T_{d2} - \Delta T_{d1}$) between two adjacent channels are generated, and this delay will be preserved after going through the DDS and the phase-locked loop (PLL) [93]-[95]. The circuit of the basic delay cell in the voltage-controlled delay lines (VCDLs) is shown in Fig. 3.3(b). The gate voltage V_{tune} is utilized to regulate the tail current to perform different time delay. In the locked loops, V_{tune} is provided by a low-pass filter (LPF) that is charged or discharged through a charge pump (CP), which is determined by the cell number in VCDLs. In this implementation, a 400-MHz reference clock is used. The measurement results show that the operating voltage is from 0.4 to 1 V with delay time from 884 to 47 ps, which achieves a wide tuning range at a coarse time resolution and provides an overdesign to tolerate the fabrication uncertainties. Note that although the absolute delay of the individual cell in the DLL VCDL is nonlinear as shown in Fig. 3.3(b), the difference in two delays (i.e., the Vernier delay) generated by two DLLs individually is linear as the cell delay of each DLL can be digitally configured to

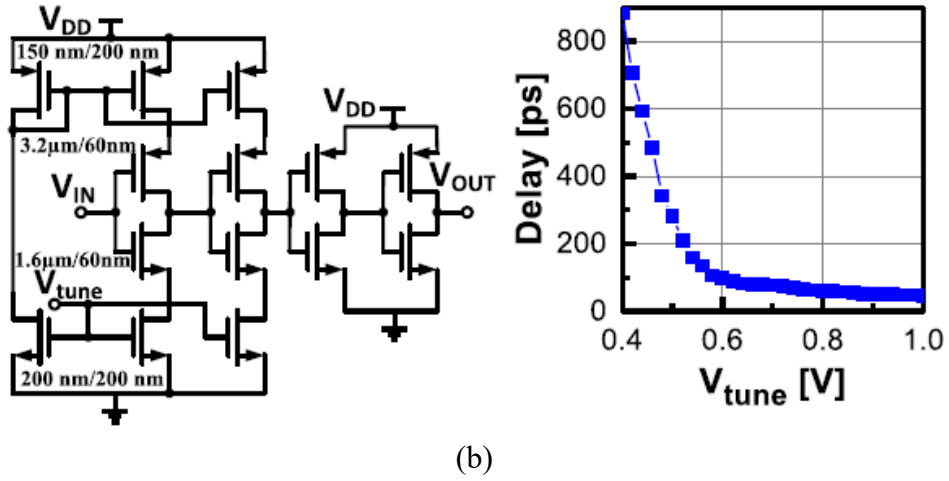
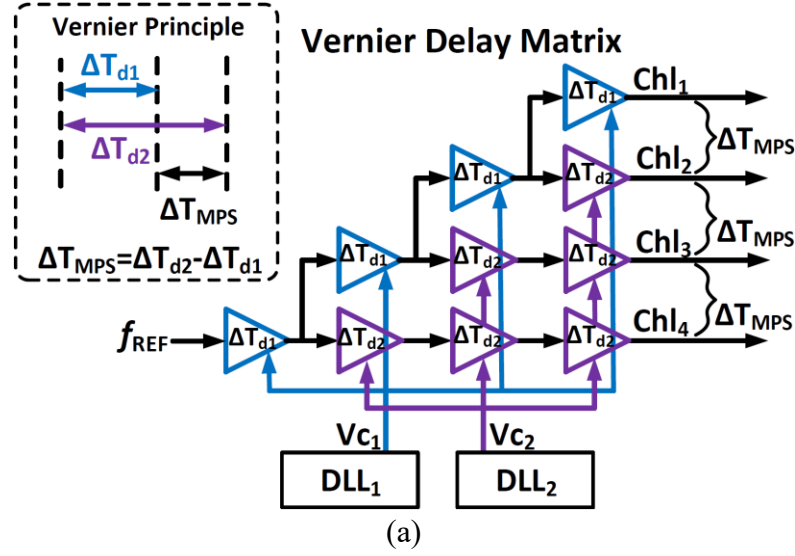


Fig. 3.3. (a) True time delay generated by the Vernier Delay Matrix [117]. (b) Schematic of VCDL cell and measurements [129].

coordinate with the other DLL of certain delay. Also, in the implementation, the two DLLs are configured accordingly for the linear Vernier delay in operation, hence the beam-steering is controlled linearly [129].

The effective beam-steering angle Φ is related to ΔT_{MPS} , the antenna pitch and the light speed [37]. For example, to generate ΔT_{MPS} for 30° beam-steering of the chirp signal at 10 GHz center frequency, the MPS needs to generate clocks with $\Delta T_{MPS} = 25ps$ in the Vernier delay matrix. Similarly, MPS provides four channels of reference clocks with a delay of adjacent channels up to $43.3ps$ to cover the field of view of $\pm 60^\circ$. On the other hand, phase shifter (PS) is employed for the fine-tuning of the RF phase to

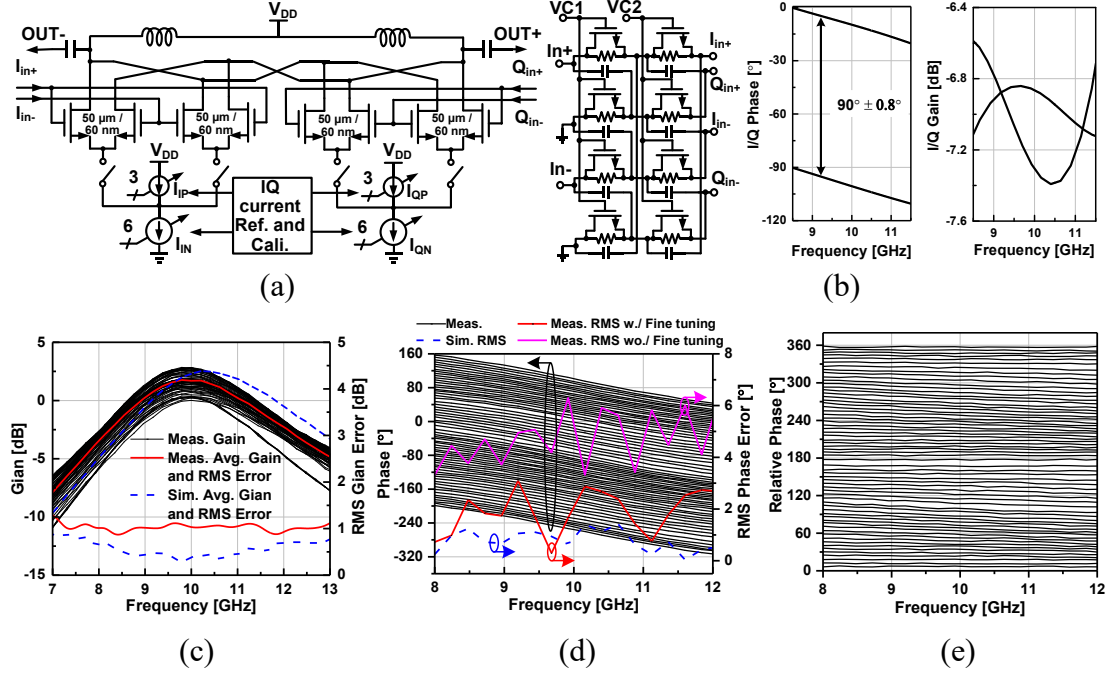


Fig. 3.4. (a) X-band phase shifter. (b) Circuit of the I/Q current generator. (c) Measured phase shifter gain. (d) Phase shifter phase state. (e) Relative phase [129].

enable the precise beam-steering. In the fine-tuning implementation with a 6-bit phase shifter, the phase shifter resolution is expressed as $\phi_{PS} = \frac{2\pi}{2^6} = 0.03125\pi$, which can enable the beam-steering resolution of around 1° at 0° steering angle. The circuit of the phase shifter is demonstrated in Fig. 3.4(a) and the circuit implementation of the IQ current generator is illustrated in Fig. 3.4(b). In this implementation, a 6-bit current-steering PS is implemented to provide a 5.625° phase-shifting resolution for the RF signal. A compact 6-bit binary-weighted current source array associated with a 3-bit current bleeding current source array is implemented for constant-current calibration and phase trimming. The output phase is configured by the difference of I and Q current sources rather than the absolute values of them, where I_{IN} and I_{QN} are 6-bit tuning DC bias current and I_{IP} and I_{QP} are 3-bit fine-tuning DC bias current for I and Q path respectively, where the 3-bit current source serve as trim bits to improve the root mean square phase error when required. The measured phase shifter gain, phase state, and relative phase are demonstrated in Figs. 3.4(c)-(e). Voltage-controlled MOSFET resistors are adopted in

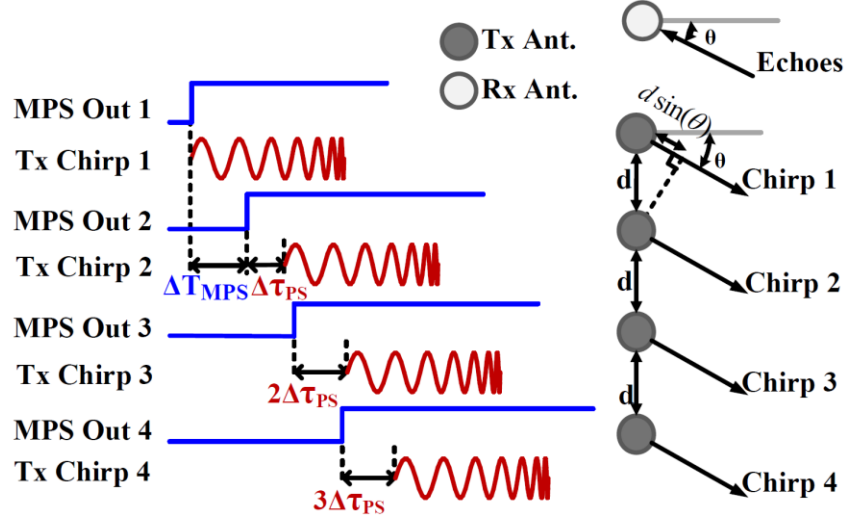


Fig. 3.5. Two-Stage Beam-steering for the proposed chip-scale radar sensor [117].

parallel with each resistor to compensate for the resistance variation and process variations [129]. The RF signal is then sent to the antenna through the power amplifier (PA) on-chip. A 1.7° beam-steering precision can be attained when the beams are focused on the 0° direction [38]. The derivation of the fine-tuning is illustrated below

a) Derivation of delay requirement for beam-steering resolution

To achieve certain beam-steering resolution, the phase delay to be fulfilled by phase shifter can be derived by

$$\Delta T_{step} = \Delta T_{MPS}(\phi_{i+1}) - \Delta T_{MPS}(\phi_i) = p \cdot \frac{\sin(\phi_{i+1}) - \sin(\phi_i)}{c}$$

b) Derivation of phase shift requirement for generating the fine delay

For a chirp signal, where ω_0 is the chirp starting frequency, and k is the chirp rate, the phase change rate is expressed as: $\omega = \omega_0 + kt$. ω is considered as $2\pi \times 10$ GHz for derivation, thus the corresponding phase change is

$$\Delta \phi = \omega \cdot \Delta T_{step}$$

In the implementation using a 6-bit phase shifter, the phase shift resolution is 0.03125π , which represents the phase shifter resolution. When $\Delta \phi = \phi_{PS}$, the ΔT_{step} is

1.5ps, corresponding to 1.7° beam steering resolution at 0° steering direction, meaning that the phase shifter can enable the beam-steering resolution of 1.7° . Note that as ΔT_{step} is proportional to $\cos(\phi)$, the achievable beam-steering resolution may vary under different beam steering angles.

As illustrated in Fig. 3.5, the delay configuration between the adjacent chirps is set by both the MPS and the phase shifter to achieve the accurate true-time delay beam-steering, which can finally enable the localization on the subject and monitoring the micro vital signs and specific macro displacements. The chirp signal is configured at the transmitter with a tunable duty cycle, where the signal can be configured as the FMCW mode or the pulsed chirp mode, enabling the enhanced time-phase resolution for detecting the target signals. Considering that the beam is steered to the subject by the phased-array radar, the transmitted power is focused to sense the target's vital signs; thus, the detection efficiency is enhanced. Compare to the MUSIC [2], where the direction of arrival (DoA) is ensured at the receiver side, in our method, the target direction is selected by the initiatively accurate beam-steering of the phased-array radar sensor [117].

For the chirp waveform, the beam-steering pattern at the desired steering angle θ is formulated as

$$P_{TX}(\theta) = 10 \cdot \log\left(\frac{1}{T_s} \int_{t=0}^{T_s} \left| \sum_{m=1}^4 s_m(t) e^{j(m-1)\pi \sin(\theta)} \right|^2 dt\right), \quad (3.4)$$

where $s_m(t) = \cos 2\pi \left[f_0(t + \Delta\tau_{MPS} + (m-1)\Delta\tau_{PS}) + k_s \int (t + \Delta\tau_{MPS} + (m-1)\Delta\tau_{PS}) dt \right]$ represents the generated chirp signal from the m^{th} transmitter when m is greater than one, k_s is the chirp rate, T_s is the chirp sweeping time, and f_0 is the starting frequency of the chirp. The $\Delta\tau_{MPS} + (m-1)\Delta\tau_{PS}$ is the time delay at the m^{th} transmitter, which is set by the DLL

in MPS and the phase shifter to be equal to $(m - 1) d \sin(\theta)/c$, where d is the distance between the antennas, and θ is the steering angle.

The beam-steering pattern is shaped by the antenna array, in the form of the multiplication of the power spectrum between beam-steered signal and the antenna array pattern. Since the transmitted signal is pointed to the subject direction, the antenna at the receiver acquires the superimposed echoes from the subject. The received echoed signal from the angle θ can thus be formulated as [40]

$$P_{RX}(\theta) = 10 \cdot \log\left(\frac{1}{T_s} \int_{t=0}^{T_s} |r(t, \theta)|^2 dt\right), \quad (3.5)$$

where the term $r(t, \theta) = \sigma \sum_{m=1}^4 s_m(t - \tau_m, \theta)$ represents the received superimposed echoed signals from the four transmitters steered at θ direction. σ is the amplitude of the received signal normalized to the transmitted signal. τ is the time delay between the transmitted signal and the received signal, which can be represented as

$$\tau = \frac{2R}{c}, \quad (3.6)$$

where R is the range between the subject and the radar, by finely configuring the MPS and the phase shifter, the echoed signal from each transmitter is approximately same.

3.2.3 Vivaldi Antenna Array for Broadband Radar Transmitter Beam-Steering

The broadband antenna element is a Vivaldi antenna with an exponentially tapered slot, which can be employed in the system to support the X-band ABS technique with improved gain [82]-[88]. As shown in Fig. 3.6(a), the elements are respectively fabricated on the substrate of Rogers RO4350B with a size of $3.07 \text{ cm} \times 4.1 \text{ cm}$ and

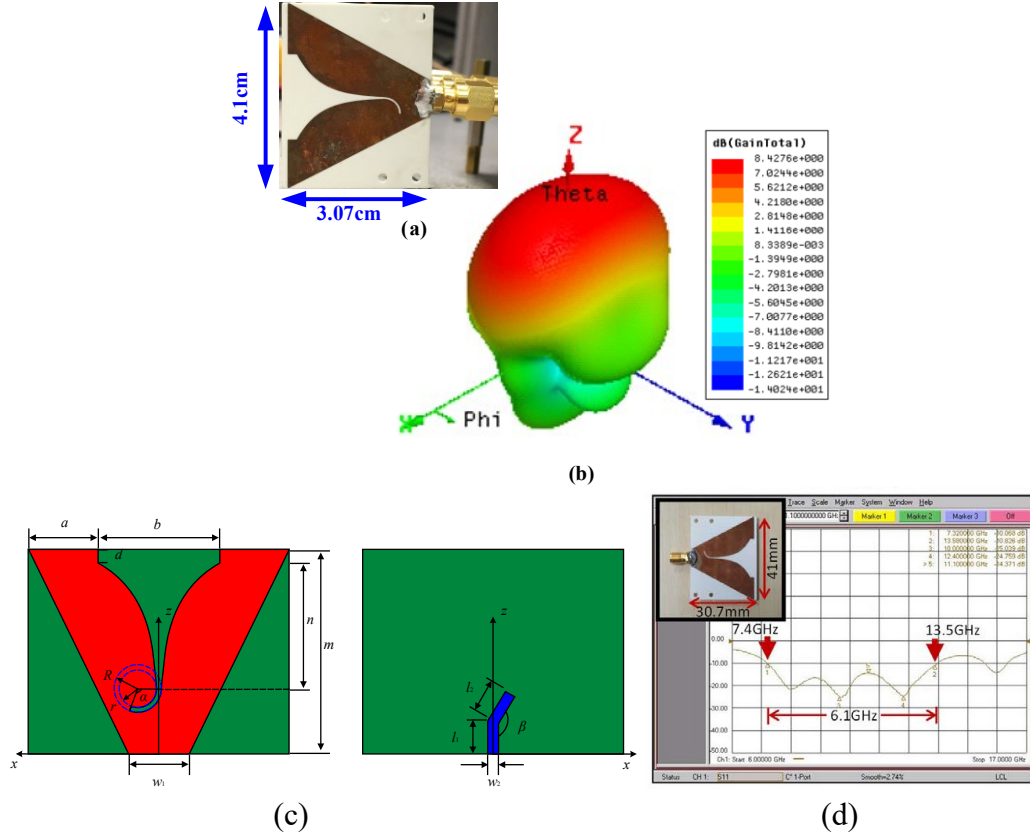


Fig. 3.6. Antenna implementation: (a) Element photo, and (b) radiation pattern at 10 GHz [117], and (c) Geometry of the antenna element, left: front view, right: bottom view, and (d) antenna size (top left) and measured S11 (bottom right) [31].

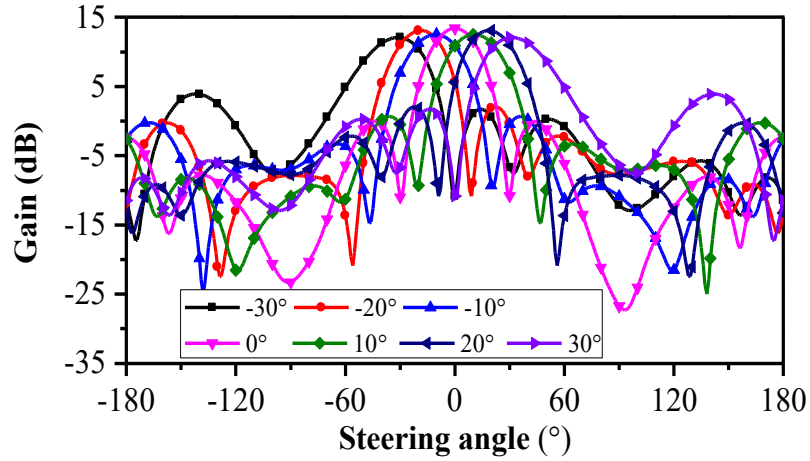


Fig. 3.7. Antenna array patterns at 10 GHz with steering angles from -30° to 30° with 10° interval [117].

located with a distance of 1.5 cm between adjacent ones, corresponding to the half a wavelength at 10 GHz in the free space. The antenna array operates at the X -band range [33]. Fig. 3.6(b) demonstrates the three-dimensional radiation pattern at the frequency

of 10 GHz, which is the center frequency of the radar, and the corresponding gain is 8.43 dB. The phase shift $\Delta\varphi_m$ at the m^{th} port relative to the first port is expressed as

$$\Delta\varphi_m = -\frac{2\pi f}{c} \cdot (m-1) \cdot d \cdot \sin \theta, \quad (3.7)$$

where d is the antenna pitch, c is the light speed in the free space, f is the operating frequency, and θ is the steering angle. The geometry of the antenna is shown in Fig. 3.6(c). The antenna size and measured S11 are demonstrated in Fig. 3.6(d) [31].

The value of the phase at each port is configured according to equation (3.7). At 10 GHz centre frequency, the simulated antenna array patterns versus the steering angle from -30° to 30° with 10° angle interval are demonstrated in Fig. 3.7. By the simultaneous adjustments on the phases of the four ports, the EM beams are steered to the dedicated directions with the antenna array, where the peaks of gain appear at the corresponding steering angles.

3.2.4 ITPA Algorithm for Discerning Multimodal Vital Signs

The working principle of a chirped radar is illustrated in Fig. 3.8, where the term τ is the time interval between the transmitted chirped signal and the echoed waveform from the object to the receiver. The intermediate frequency f_{IF} is generated by mixing the local chirp with the echo as the coherent de-chirping process, which is obtained by [23]

$$f_{IF} = \frac{BW_c}{T_s} \cdot \tau, \quad (3.8)$$

where T_s is the time span for chirp sweeping. The chirp rate is expressed as $k_s = BW_c/T_s$, where BW_c stands for the bandwidth of the received signal; thus, the transmitted chirp waveform in one chirp period is approximately expressed as

$$s_T(t) = \cos[2\pi f_0 t + \pi k_s t^2 + \phi_0]. \quad (3.9)$$

The received waveform from the target is expressed as

$$s_R(t) = \cos[2\pi f_0(t - \tau) + \pi k_s(t - \tau)^2 + \phi_1], \quad (3.10)$$

where the different value of ϕ_0 and ϕ_1 can be set to a constant $\Delta\phi \approx 0$ when the radar system is finely configured to the optimum coherent working status through the serial peripheral interface (SPI), thus the phase noise of the transmitted signal and received signal are correlated and eliminated in the mixing process for short-range monitoring. The four transmitters operate simultaneously to transmit the waveform to the target direction θ through phase-shifting and true-time delay between the channels.

The range resolution, qualifying the radar's capability on separating two objects, is decided by $\frac{c}{2BW_c} = 15\text{cm}$ under the 1 GHz bandwidth at the center frequency f_c of 10 GHz of the chirp, which is too coarse to be leveraged directly to detect the micro physiological movements [25]. However, the phase differences between the chirps, which are the time-domain integration of the frequency shift, are highly sensitive and indicative of the physiological-related micro-movements and displacements of the subjects [34]. In the presented radar system, the four-channel transmitter is used for accurate beam-steering. The one-channel receiver is used to acquire the echoed signals, which are then processed by the ITPA algorithm to realize the accurate monitoring on the vital signs in the time-phase domain.

The flow chart of the ITPA algorithm is shown in Fig. 3.9. The de-chirped signal at the receiver, which is expressed as $B(t)$, firstly undergoes the phase alignment to form a 2D matrix. Then the fast Fourier transform is applied to the de-chirped signal to extract the intermediate frequency f_{IF} , which equals to $2k_s R_n/c$. R_n is the normal range between the subject and the radar. The localization of the subject is realized by the range and the direction determined based on the ABS technique.

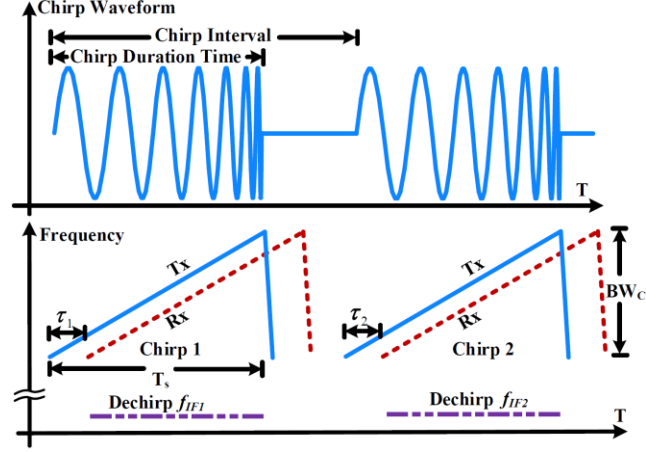


Fig. 3.8. Transmitted chirp waveform and the de-chirping process at receiver.

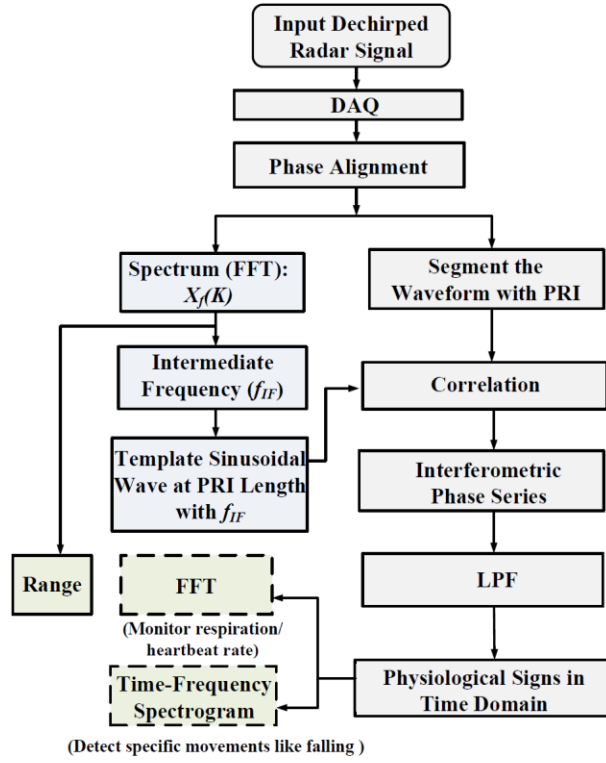


Fig. 3.9. Flowchart of the ITPA algorithm for ranging and vital sign monitoring [117].

When monitoring the micro-movements, the time delay between the transmitter and the receiver under this circumstance is expressed as

$$\tau = \frac{2(R_n + \Delta R(t))}{c}, \quad (3.11)$$

where the term $\Delta R(t)$ represents the micro-movements of the subject, indicating the time-varying physiological signs related displacements in our cases.

After the de-chirping, the de-chirped signal at the receiver is approximately expressed as [39]

$$\begin{aligned} B(t) &= \sigma \cos \left[2\pi f_0 \tau + \pi k_s (2t\tau - \tau^2) \right] \\ &\approx \sigma \cos \left[2\pi \left(\left(\frac{2k_s (R_n + \Delta R(t))}{c} \right) t + \frac{2f_0 (R_n + \Delta R(t))}{c} \right) \right], \end{aligned} \quad (3.12)$$

where the second order term is ignored considering the small value of τ under the short-range biomedical radar sensing scenario. For example, when the subject is at 1.5 m distance, the corresponding τ equals to 10^{-8} second and the second-order term $\pi k_s \tau^2$ is 10^6 times smaller than the first-order term $2\pi f_0 \tau$. The phase information at each chirp interval can be utilized to monitor the corresponding physiological signs like heartbeat rate and respiration rate or to detect specific movements such as falling. The motion of the subject in the time domain can be represented as

$$\begin{aligned} \Delta R(t) &= R_m(t) + R_M(t) \\ &\approx r_h \cos(\omega_h t) + r_r \cos(\omega_r t) + r_M(t). \end{aligned} \quad (3.13)$$

Where $R_m(t)$ represent the micro-movements induced by heartbeat and respiration, and $R_M(t)$ stands for the macro movements such as falling. When monitoring respiration rates and heartbeat rates, $R_M(t)$ is zero as the subject is still. The heartbeat and respiration are approximately represented as sinusoids with amplitudes r_h and r_r , and frequencies ω_h , which is usually between 1 Hz to 3 Hz, and ω_r , which is usually between 0.1 Hz to 0.5 Hz, respectively [6], [12], [13]. When detecting the falling, $R_m(t)$ is negligible and $R_M(t)$ represents the range variation caused by the falling, which is modeled as $r_M(t)$.

The interferometric phase variation is induced by the superposition of the displacements from the subject, and the spectrogram of the signatures can be obtained by applying Fourier transform to the time-domain interferometric phase. To extract the

interferometric phase, the de-chirped signal will be correlated with a sinusoidal template waveform. The template waveform is as the same length as the span of chirp sweeping time T_s . The template waveform is expressed as

$$temp(t) = \sum_{i=1}^{\infty} \cos[2\pi f_{temp}(t - i \cdot T_s) + \varphi_{temp}] \cdot [u(t - i \cdot T_s) - u(t - (i+1) \cdot T_s)], \quad (3.14)$$

where the frequency of the template is expressed as $f_{temp} = \frac{2k_s R_n}{c}$ and the initial phase of the template is expressed as $\varphi_{temp} = \frac{4\pi f_0 R_n}{c}$, which are same to the static frequency and the static phase of $B(t)$ in (3.12). Since the displacements $\Delta R(t)$ caused by heartbeat and respiration are limited within a small time span of the detection, $\Delta R(t)$ at the i^{th} chirp period is considered as a constant $\Delta R(i \cdot T_s)$. Considering that the vital sign signal is typically lower than 10 Hz, the low-pass filter (LPF) is applied to suppress the high-frequency spurs. The cross-correlation result $\hat{P}_i(\eta)$ with time shift η at the i^{th} period is represented in continuous time domain as

$$\begin{aligned} \hat{P}_i(\eta) &= \int_{i \cdot T_s}^{(i+1) \cdot T_s} B(t) \cdot temp(t + \eta) dt \\ &\approx \frac{\sigma}{2} \int_{i \cdot T_s}^{(i+1) \cdot T_s} \cos \frac{4\pi k_s}{c} (\Delta R(i \cdot T_s)t - R_n \eta) dt \\ &= \frac{c\sigma}{8\pi k_s \Delta R(i \cdot T_s)} \left(\sin \frac{4\pi k_s}{c} (R_n \eta) - \sin \frac{4\pi k_s}{c} (R_n \eta - \Delta R(i \cdot T_s)T_s) \right). \end{aligned} \quad (3.15)$$

To obtain the maximum value of the correlation result between the template and the de-chirped signal of the i^{th} period. We make the partial derivation of $\hat{P}_i(\eta)$ to η , which is expressed as

$$\frac{\partial \hat{P}_i(\eta)}{\partial \eta} = \frac{\sigma}{2\Delta R(i \cdot T_s)} \left(\cos \frac{4\pi k_s}{c} (\Delta R(i \cdot T_s)T_s - R_n \eta) - \cos \frac{4\pi k_s}{c} (R_n \eta) \right). \quad (3.16)$$

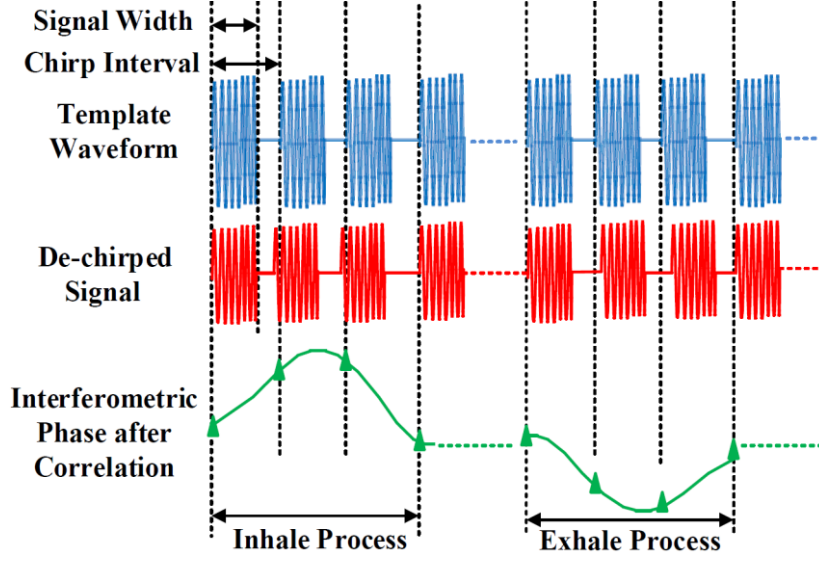


Fig. 3.10. Illustration of the interferometric time-phase analysis algorithm [117].

The maximum value of $\hat{P}_i(\eta)$ occurs when (3.16) is zero, and correspondingly

$\eta(i) = \frac{\Delta R(i \cdot T_s) T_s}{2R_n}$. We define the term interferometric phase, which is expressed as

$$\phi_{\text{int}}(i) = f_{\text{temp}} \cdot \eta(i) = \frac{2\pi k_s T_s \Delta R(i \cdot T_s)}{c}$$

to demonstrate the phase shift corresponding to the relative time shift $\eta(i)$ at the i^{th} period.

The amplitude of the extracted interferometric phase is linearly proportional to $\Delta R(i \cdot T_s)$, which is the displacement caused by the superposition of the movements caused by the vital signs such as heartbeat and respiration, or macro displacements such as falling during the i^{th} period. The phase shift at the i^{th} period induced by the Doppler effect is expressed as $\phi_{\text{Doppler}}(i) = \frac{4\pi}{\lambda} \Delta R(i \cdot T_s)$, where λ is the wavelength of the chirp [39].

Thus, $\phi_{\text{int}}(i) = \frac{BW \cdot \lambda}{2c} \phi_{\text{Doppler}}(i)$, indicating that the interferometric phase is consistent with

the Doppler phase. Information of the motion can be extracted accurately from the interferometric phase, enabling the monitoring on the vital signs such as respiration and heartbeat. Considering that the ITPA method is realized based on coherent detection on phase, the sensitivity of the radar sensor is enhanced compared to the detection using

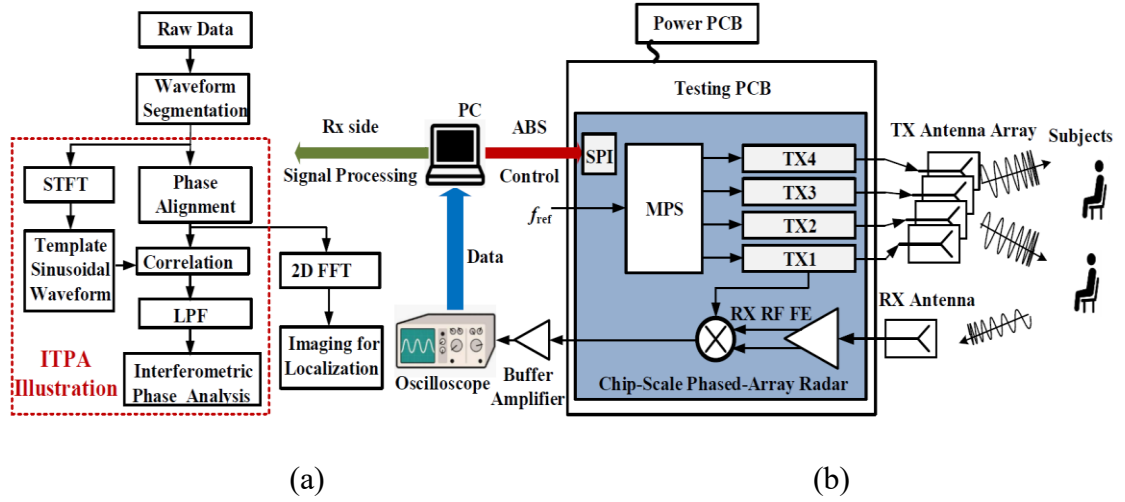


Fig. 3.11. Experiment illustration: (a) Algorithm implementation in the experiment, and (b) systematic configuration of the radar sensor [117].

Doppler frequency shift [41]. Moreover, the interferences and noise are suppressed in the correlation process.

The algorithm is illustrated in Fig. 3.10. In the time domain, when the movement is approaching towards the radar (e.g., inhale process), the interferometric phase difference will increase with a positive value; when the movement is moving backward from the radar (e.g., exhale process), the interferometric phase will decrease with a negative value. When the subject keeps still, the interferometric phase will be at zero value. Through monitoring the interferometric phase in the time domain, the time-varying characteristics of physiological-related movements can be detected and based on the frequency-domain processing of the interferometric phase series, the respiration rate and heartbeat rate can be obtained.

3.3 Experimental Verifications and Analysis

For transmitter beam-steering, the chirp ramping 1 GHz per 1.2 milliseconds is adopted, and the chirp repetition frequency is 800 Hz. The algorithms and the entire radar sensor system in the experiments are illustrated in Fig. 3.11. By applying the ITPA algorithms in Fig. 3.11(a), the collected de-chirped IF baseband signals are processed to

realize the extraction and the monitoring of physiological signs. Imaging was realized in the experiment to demonstrate the localization of the subjects in different directions. The systematic configuration is shown in Fig. 3.11(b), which consists of the CMOS-integrated phased-array radar, the power PCB, and the broadband Vivaldi antenna array. A programmable gain amplifier with high input impedance (above $k\Omega$) and moderate output impedance (several tens Ω) is leveraged to amplify the de-chirped signal at the receiver output as a buffer. In the experiments, the ABS control is realized by the combined configuration on the phase shifter for the RF phase-shifting and the MPS for the true-time delay through the SPI, which is illustrated in Fig. 3.11. The SPI on-chip operates at 4 MHz for read/write, and each full configuration for the CMOS-integrated phased-array radar sensor in the experiment will be done within 400 μ s. The IF signal after buffer is acquired at the 1 MHz sampling rate by the oscilloscope, which is synchronized by a trigger signal generated in the phased-array chip indicating the start of each chirp. Finally, the acquired raw data is transferred to a computer for processing.

With antennas placed 1.5 cm apart from each other, which correspond to $\lambda/2$ of the 10 GHz center frequency, the transmitted beams are steered to the subject angle by PS and MPS, and the receiver can continuously receive the echoed signals from the subject, enabling both the spatial resolution and the usability of the radar sensor. The ABS technique is implemented to firstly scan the scene to acquire the angular directions of the subjects. The measured spectrum of the transmitted chirp signal is shown in Fig. 3.12, given the transmitted signal is centered at 10 GHz with 1 GHz bandwidth. The spectrum of the de-chirped IF signal after the mixer is shown in Fig. 3.13, where the peak appears at 8.3 kHz, indicating a 1.5-m distance between the radar and the subject. Through configuring the VGLNA and the PGA buffer, the IF signal is amplified to about 0 dBm for acquisition and processing by the ITPA algorithm.

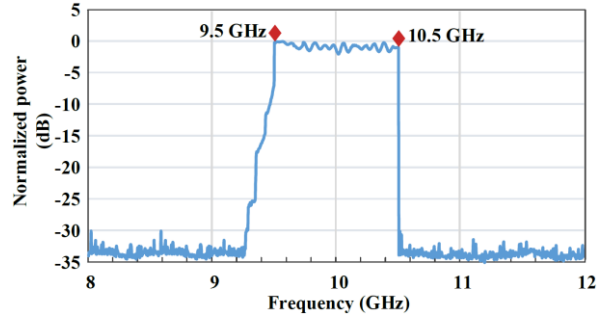


Fig. 3.12. Measured spectrum of the chirp signal from transmitter antenna [117].

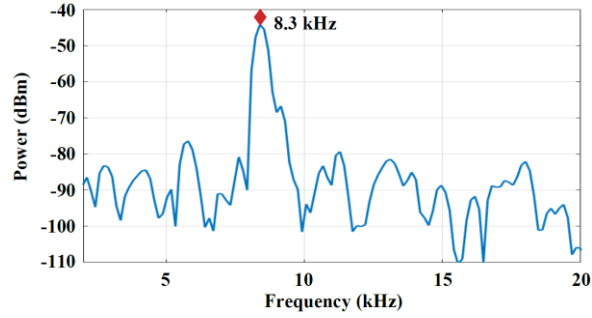


Fig. 3.13. Measured spectrum of the de-chirped IF signal after the mixer [117].

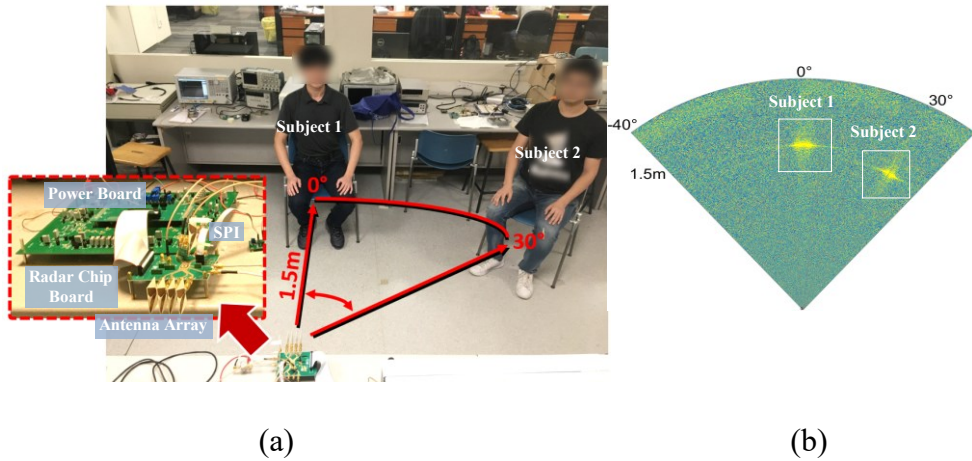
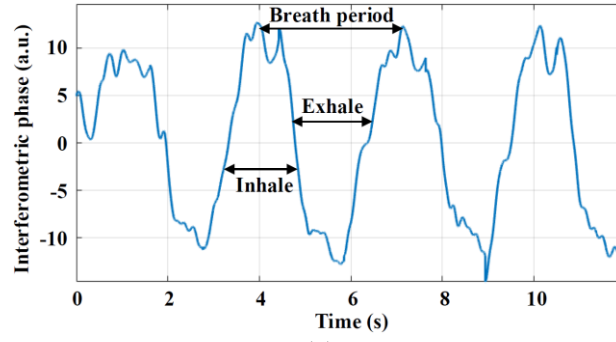


Fig. 3.14. Experimental setup and environment: (a) Radar system and subjects in the scene with illustration, and (b) localization of subjects in the experiment [117].

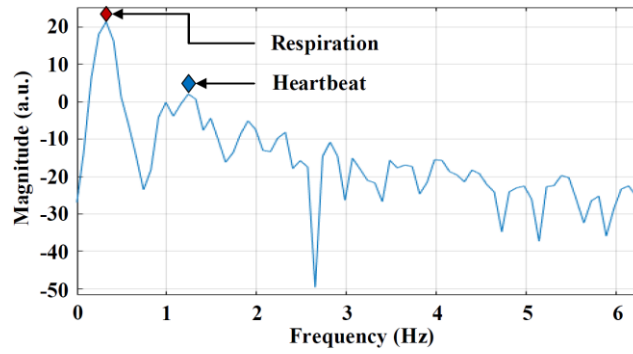
The experimental setup and the environment were shown in Fig. 3.14, where the two subjects under monitoring were seated at the direction of 0° and 30° , respectively. The radar sensor system is shown in the red dashed box in Fig. 3.14(a), where the phased-array radar chip is mounted on PCB connected with the Vivaldi antenna array. The location of the subject was determined by both the azimuth angle and the range. The synthesized imaging of the subject localization adopting ABS technique is

Table 3-2.
Phase Shifting Settings at Each Channel for Steering Angles of 0° and 30° .

θ	0°	30°
$\Delta\phi_1$	0°	0°
$\Delta\phi_2$	0°	-90°
$\Delta\phi_3$	0°	-180°
$\Delta\phi_4$	0°	-270°



(a)



(b)

Fig. 3.15. Respiration and heartbeat measurement at 0° : (a) Phase pattern in time domain, and (b) spectrum of the interferometric phase after ITPA processing [117].

illustrated in Fig. 3.14(b). In the experiment, the acquired data with the subjects in the environment was calibrated by the prior background data so that the effects induced by the clutters were suppressed. In the physiological signs monitoring experiments, the beams were steered to the subject based on the prior location information. In the imaging experiment, the subjects were in the directions of 0° and 30° in the FoV. Table 3-2 illustrates the equivalent phase-shifting at each channel output for the corresponding steering angle, where the parameters were calculated according to (3.7).

The transmitted beam was firstly steered to the targeted direction of 0° , where a human subject was seated in front of the radar sensor with the normal range of 1.5 m.

The respiration rate and heartbeat rate of the subject were monitored, and experiments were conducted multiple times to acquire the representative results.

The monitored subject in the experiments is a 24-year-old male with 184 cm height and 75 kg weight. As shown in Fig. 3.15(a), the interferometric phase series extracted from the ITPA algorithm reflect the micro-movements due to respiration and heartbeat, where the inhale process, exhale process, and the breath period are indicated. The amplitude of the recovered interferometric phase is proportional to the respiratory amplitude. As shown in Fig. 3.15(b), the extracted respiration rate in the experiment was 21 beats per minute corresponding to the first peak frequency of 0.35 Hz. The heartbeat rate was 73 beats per minute corresponding to the second peak frequency of 1.22 Hz. When the respiration signature of the subject changes, the amplitude of the interferometric phase at each period interval will change accordingly. Furthermore, the analysis on the interferometric phase in frequency domain is performed to monitor the respiration rate and heartbeat rate so that the variations on respiration rate and heartbeat rate are recorded, which are indicative to the health status of the subject. When the transmitted beams were steered to the subject at 30° direction, the vital signs were recognized, as shown in Fig. 3.16(a). However, the extracted signatures were with some distortions, which were induced by the clutters in the experimental environment as well as the antenna pattern. The extracted respiration rate was 22 beats per minute, corresponding to the peak frequency of 0.37 Hz, which was shown in Fig. 3.16(b). There was a peak at the frequency of 1.2 Hz, corresponding to the heartbeat rate of 72 beats per minute. Compared to the results at 0° direction, the heartbeat frequency was relatively ambiguous at the direction of 30°.

Fig. 3.17 shows the continuous results of the monitored respiration rate and heartbeat rate of the subject sitting at 0° direction, where the respiration rate and the

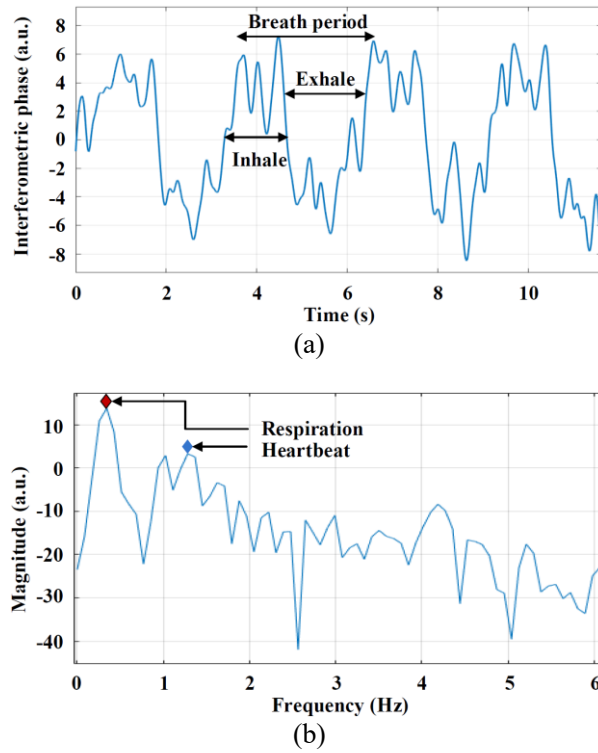


Fig. 3.16. Respiration and heartbeat measurement at 30° : (a) Phase pattern in time domain, and (b) spectrum of the interferometric phase after ITPA processing [117].

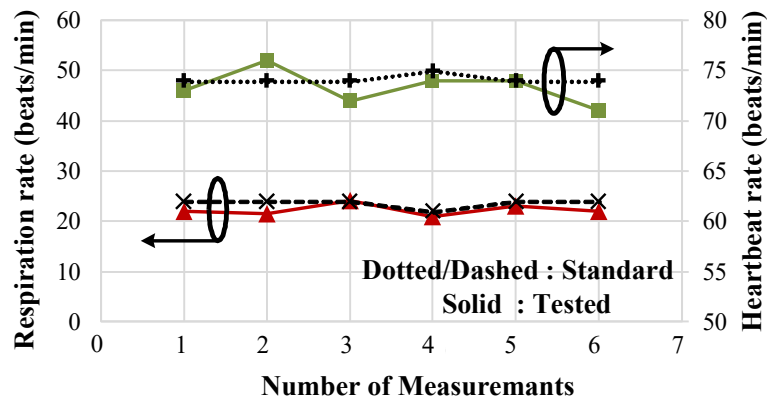


Fig. 3.17. Tested respiration/heartbeat rate from radar system for the subject at 0° direction, and standard measurement results [117].

heartbeat rate was obtained by a series of measurements and processing using the ITPA algorithm. To compare intuitively with the standard value, the respiration rate and heartbeat rate of the same subject were measured using medical appliances as the references, which were reported as the dotted and dashed black lines in Fig. 3.17. The heartbeat rate obtained with the radar sensor, which was illustrated as the solid green

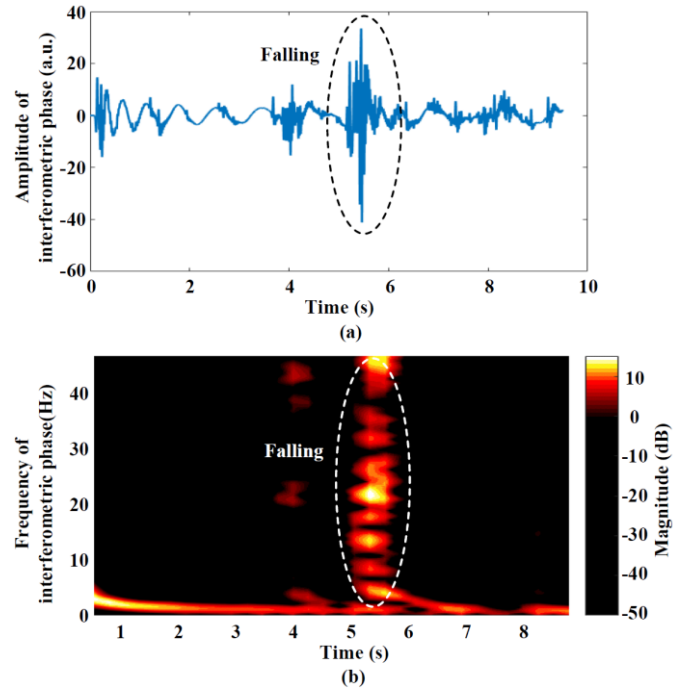


Fig. 3.18. Detected falling at 0° using the ITPA algorithm: (a) Signatures in time domain, and (b) spectrum of the interferometric phase signature [117].

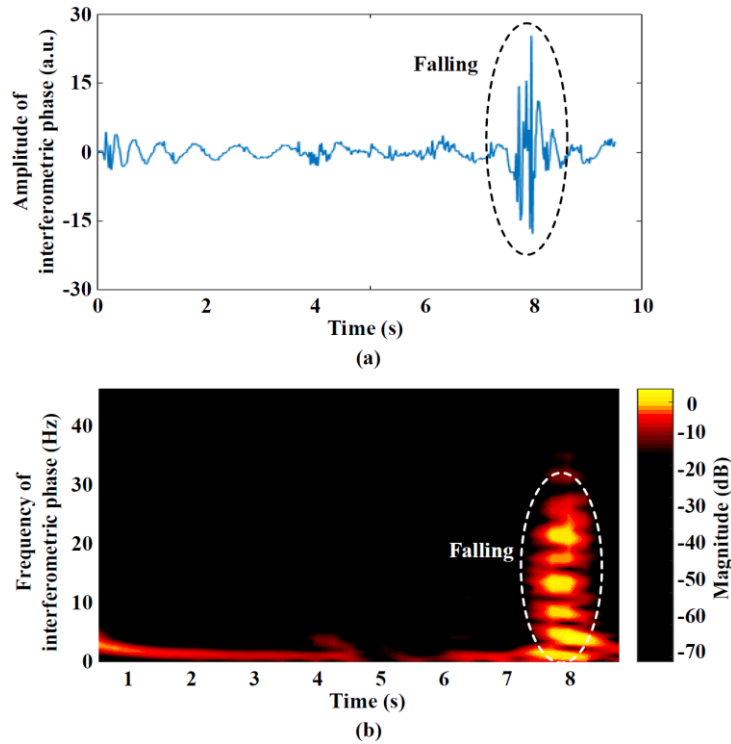


Fig. 3.19. Detected falling at 30° using the ITPA algorithm: (a) Signatures in time domain and (b) spectrum of the interferometric phase signature [117].

line in the figure, was around 73 beats per minute. The respiration rate illustrated as the solid red line was around 22 beats per minute. The respiration rate and heartbeat rate

obtained by the ITPA algorithm agree well with the reference respiration rate and heartbeat rate, respectively.

In Section 3.3, the integrated radar sensor has verified its capability on monitoring weak vital signs. Moreover, the monolithic system can be used to detect falling, which is essential for comprehensive elderly care applications. The experimental fallings at 0° were carried out, and the interferometric phase obtained from the ITPA algorithm was shown in Fig. 3.18(a), where the abrupt phase change was observed occurring at 5 s to 5.5 s, indicating the experimental falling-forward process at the time. By the time-frequency analysis, the spectrogram of the falling signature is illustrated in Fig. 3.18(b), where the falling process was reflected in the time-frequency domain as an abrupt change on the interferometric phase in both the time domain and the frequency domain. For detecting the falling at 30° direction, as illustrated in Figs. 3.19(a) and 3.19(b), the abrupt phase change was observed at 8 second, indicating the human falling-forward process at that time.

3.4 Discussion and Comparison

As shown in Figs. 3.18 and 3.19, the detection of falling in a wide field-of-view has been validated, demonstrating the potential of the proposed CMOS chip-scale phased-array radar sensor to detect the anomaly such as falling. The performance summary and comparison with prior art healthcare radar sensors are shown in Table 3-3. Compare to [7], [8], [37], and [24], this work realized the integrated chip solution. With the combined implementation of the accurate beam-steering technique and the ITPA method, localization on the subjects in a wide FoV is achieved. Moreover, the accurate monitoring of vital signs including respiration rate and heartbeat rate, and the detection on the falling, are achieved based on the compact CMOS-integrated radar

Table 3-3.
Comparison with the State-of-the-Art Radar Sensors.

Properties		IMS 2013 [37]	JSSC 2014 [26]	TMTT 2017 [24]	TMTT 2018 [7]	TMTT 2018 [8]	This Work
Integrated Functions on Chip		n.a.	Tx+Rx+DLL+Control Logic	n.a.	n.a.	BGT24 MTR11 (Commercial Product by Infineon).	Multi-Phase Synthesizer+ Tx Array + Rx FE+ SPI Control Logic
Range of Modulation Period		n.a.	n.a.	n.a.	n.a.	n.a.	Digital Tunable:0.5ms~10ms
Measured Tx Output Bandwidth		n.a.	2 GHz	320 MHz	n.a.	n.a.	1 GHz
Center Frequency		n.a.	4 GHz	5.8 GHz	2.4 GHz	24 GHz	10 GHz
Modulation Type		UWB Impulse	Impulse Radio	FMCW/ Doppler Mode	Single-Tone Continuous Wave	Single-Tone Continuous Wave	FMCW/ Pulsed Chirp
Antenna Type		Vivaldi Antenna	Horn Antenna	Patch Antenna	Patch Antenna	Series-feed Patch Antenna	Broadband Vivaldi Antenna Array
Technology		Discrete components in PCB-level	130-nm CMOS	Discrete components in PCB-level	Discrete components in PCB-level	Discrete components in PCB-level	65-nm CMOS
Active Channel		1Tx+1 Rx	1Tx+4 Rx	1Tx+1 I/Q Rx	1Tx+1Rx	1Tx+1 I/Q Rx	4Tx+1Rx
Beam-Steering Methodology		n.a.	n.a.	n.a.	n.a.	n.a.	Two-stage Beam-steering
Signal Processing Algorithm		Synthesized Processing	Fourier Transform	ISAR/ Micro-Doppler	Gaussian Pulse Train/ FTPR	Linearized Doppler Phase Demodulation	Interferometric Time-Phase Analysis
Monitoring Functions	Localization	YES	n.a.	YES	n.a.	n.a.	YES
	Respiration	YES	YES	YES	YES	YES	YES
	Heartbeat	n.a.	n.a.	YES	YES	YES	YES
	Falling	n.a.	n.a.	n.a.	n.a.	n.a.	YES

sensor, enabling versatile sensing in chip scale compared to [26]. It needs to be noted that the ITPA method doesn't achieve the same performance in differentiating the

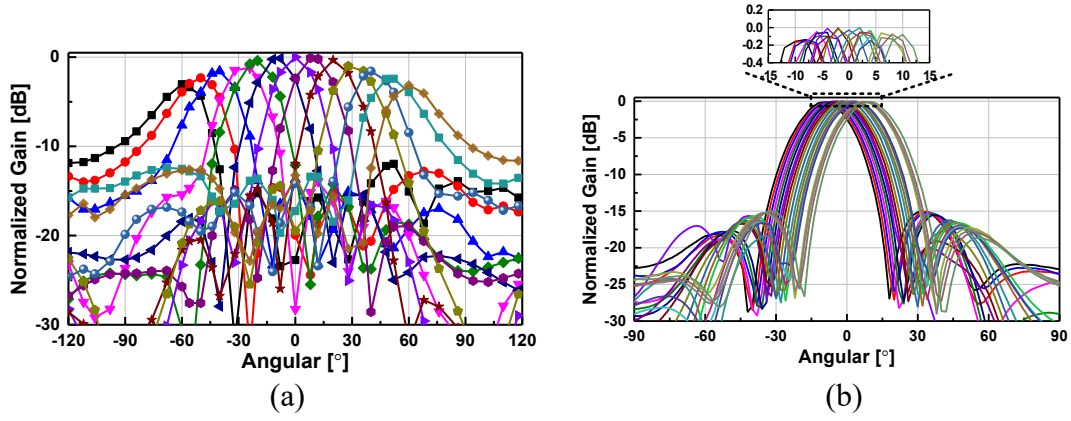


Fig. 3.20. Measured 4-element TX beam-steering radiation pattern at 10 GHz with: (a) $\pm 60^\circ$ scan angles with coarse scanning of 10° steps and (b) Fine beam control of $\sim 1^\circ$ steps at 2λ antenna pitch [129].

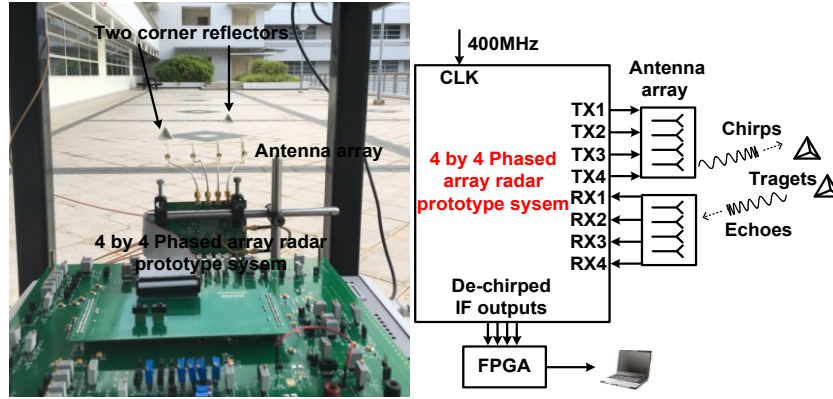


Fig. 3.21. A testing setup of the phased-array chip-scale radar system [129].

characteristic dynamics of the falling process compared to a brilliant method presented in [42] based on the technique, where the range-Doppler profile is fully utilized. However, the specified chip-algorithm co-design enables both discerning vital signs and alerting the falling when sudden phase changes are detected. For a more advanced movement detection such as classifying various kinds of movement patterns (e.g., squat and bend), specific signal processing algorithms and completed digital processing unit are essential, which are not the focus of the current Chapter and will be discussed and explored in the future work.

Generally speaking, the phase controlled in RX by beamforming and in TX by beam-steering are equivalent. For example, using 4T1R is of same performance as 1T4R

theoretically. 4T1R is used here for two purposes, 1) to demonstrate the two-stage beam-steering for wide field of view (FoV) localization and vital sign sensing, 2) to avoid the mismatch between multiple RX channels as the phase of the de-chirp signal is crucial in the vital sign sensing. 1TnR solution with digital beamforming would be a good choice given all the baseband, such as VGA/Filter/ADC/interface to digital baseband are integrated together. As our prototype bio-radar is currently a proof-of-concept without full integration of analog baseband and digital baseband, to ensure there is no issue on phase misalignment of the received signals of multiple RXs for vital sign detection, 4T1R is adopted for this experiment. We have tested the digital beamforming of 4TX-4RX phased-array radar sensor with 2λ distance between the antenna at each channel and demonstrated the imaging function [129]. The measurement result of the digital beamforming of coarse scanning is shown in Fig. 3.20(a) and the digital beamforming of fine beam control is shown in Fig. 3.20(b). A testing setup of the phased-array chip-scale radar system is shown in Fig. 3.21, where each module is indicated.

In this work, the beam-steering of the phased-array radar sensor is achieved through manually configuring the SPI to control both the delay-locked loop (DLL)-based multiphase synthesizer (MPS) and phase shifter (PS) on-chip to steer the beams to the targeted direction, and then set to another direction after data acquisition. The automatic and adaptive scanning hasn't been implemented in the current radar sensor. In the current radar sensor, the focus is on demonstrating the potentials of a CMOS radar chip for locating the subjects and detecting the movement and vital signs of the subjects. In the future work, the automotive and adaptive scanning can be implemented on-chip. The performance is summarized and compared with the other published monolithic phased-array or multichannel *X*-band radar TRXs in Table 3-4. It shows that the

TABLE 3-4.

CIRCUIT PARAMETERS OF THE *X*-BAND PHASED-ARRAY PROTOTYPE AND COMPARISON

	[83]	[97]	[98]	[99]	[100]	[101]	[102]	This work
Technology	0.13- μ m SiGe BiCMOS	0.18- μ m CMOS	0.13- μ m CMOS	0.13- μ m CMOS	0.13- μ m SiGe BiCMOS	0.18- μ m CMOS	0.13- μ m SiGe BiCMOS	65-nm CMOS
Channel No.	RX+TX	2RX+TX	4RX	4TX	RX+TX	RX+TX	RX	4RX+4TX
Operating Frequency (GHz)	9-11	10.5	8.5-10.5	7.9-9.6	8-9	8.5-10	8-10.7	9.1-10.6
Modulation method	N. A.	FMCW	N. A.	FMCW	FMCW	N. A.	N. A.	Pulsed chirp
Modulation Period (ms)	N. A.	N. A.	N. A.	N. A.	N. A.	N. A.	N. A.	0.2-1
TX chirp output BW (GHz)	N. A.	N. A.	N. A.	0.5	0.15	N. A.	N. A.	1
Stretch Processing	N. A.	N. A.	N. A.	N. A.	YES	N. A.	N. A.	YES
PS No. of bits	5	N. A.	4-5	4 (+ trim-bit)	N. A.	6	5	6 (+ 3 trim-bit)
RMS phase error	3.8°	N. A.	4.5°	6°	N. A.	2°	9°	3.1°
Beamsteering	N. A.	N. A.	N. A.	N. A.	N. A.	N. A.	N. A.	$\pm 60^\circ @ \sim 1^\circ$
TX P_{out} (dBm)	28	1	N. A.	13.6	N. A.	11.5	N. A.	~ 10
Phase Noise @ 1MHz offset	N. A.	-93	N. A.	N. A.	-114	N. A.	N. A.	-116.4
RXFE Gain (dB)	25	-4.5	10.1	N. A.	10.7-44.7	12	11.5	22.5-24.1
RXFE NF (dB)	3	11.5	3.4	N. A.	2.4-4.5	8.5	4.1	4.8-6.2
RxFE IP1dB (dBm)	-24	-29	-12.5	N. A.	-35	0	-23	-33.6
RX/TX Power/channel (mW)	352/4128	N. A./N. A.	36/N. A.	N. A./217	326/333	670/640	33/N. A.	65.9/162.2
Total Power (mW)	4480	350	144	870	659	1310	33	950
Die Size (mm ²)	5.2 \times 3.0	2.6 \times 3.3	2.5 \times 2.9	2.9 \times 3.0	3.5 \times 2.5	4.4 \times 2.9	3.8 \times 3.5	4 \times 2.65

implemented phased-array radar TRX chip prototype achieves the beam-steering angle of $\pm 60^\circ$ with the best 1° step at 2λ antenna pitch, the better TX chirp output BW up to

1 GHz at 10 GHz, and the best power efficiency [129].

3.5 DLL-based Multi-Phase Clock Generator for True-Time-Delay Wideband FMCW Phased-Array Radar Sensor

The CMOS-integrated phased-array radar sensor for multimodal vital signs monitoring has been presented in detail, where Vernier-based delay-locked loop (DLL) is served as an essential component to enable the wide FoV sensing. In this chapter, the Vernier-based DLL design for multi-phase clock generation for the phased-array radar sensor is presented in detail, where the TSMC 40-nm CMOS process is used to fabricate the DLL-based clock generator as a separate circuit and block, and it is tested.

3.5.1 Principle of DLL

Delay-locked loop (DLL) can be served as an essential circuit component in transceiver due to its stable structure, avoiding the jitter accumulation and achieving fast locking. Most studies of DLL focus on achieving wide operating range, high time resolution, low jitter, fast locking and flexible phase delay [43]-[46]. In addition, highly integrated DLL-based architectures have been widely used for the generation of the on-chip clocks and timing applications, such as reference clock generator, clock and data recovery circuit and frequency synthesizer [47]-[49]. Phased array technique is widely used in RF/mm-wave frequencies to compensate for high path loss and to suppress interference from the undesired direction [50]. In a beam-steering system, multiple wideband beams are essential for achieving high directivity transmission. Although conventional phase shifters exhibit good performance in narrowband applications, a wideband phased array transceiver (TRX) is needed to support multiple bands.

However, they are naturally not able to provide a constant time shift across a wide

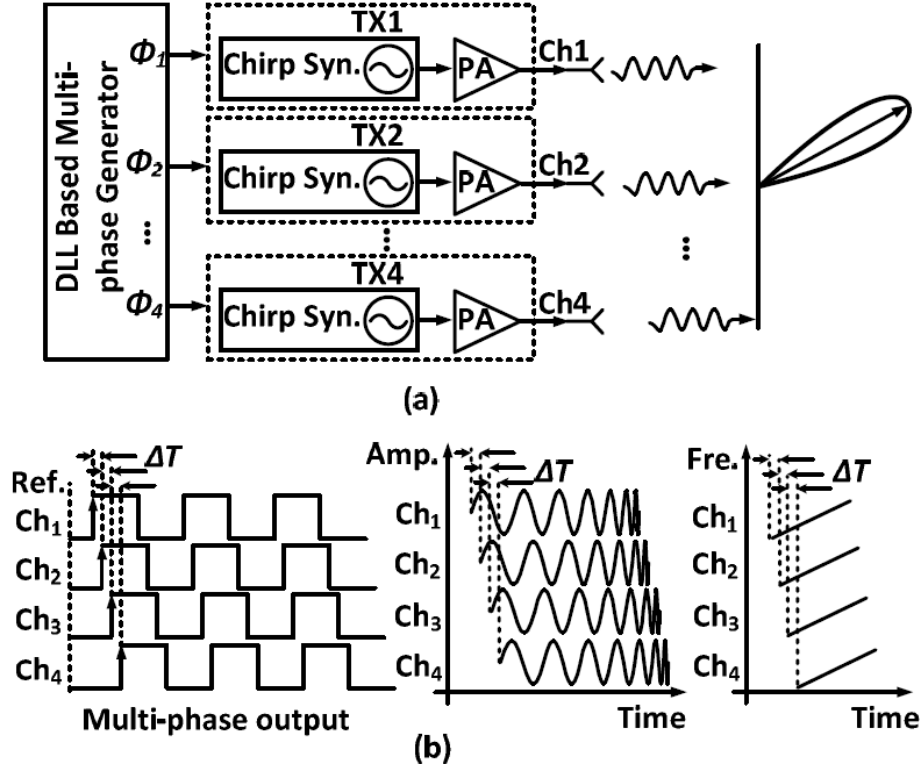


Fig. 3.22 (a) A 4-channel TX (b) True-time-delay in multi-phase output [123].

frequency range covering different bands, which is essential in wideband phased array systems. The true-time-delay phase shifters, on another hand, offer variable time delays over large bandwidth at the cost of structure complexity (e.g., micro-electromechanical system (MEMS), optical, etc.), power consumption and chip area. Therefore, a clock generator generates multi-phase signals with true-time delay based on CMOS process is preferable. A 4-channel transmitter (TX) is shown in the Fig. 3.22(a), where the proposed clock generator generates multi-phase signals serving as the reference by the chirp synthesizer and then amplified by the power amplifier before transmission for beam-steering. The clock signals with time delay of ΔT are reflected by the voltage and frequency of the chirp signals in 4 channels, which is demonstrated in Fig. 3.22(a) and the true-time-delay in multi-phase output is shown in Fig.3.22(b) [123].

As large bandwidth and configurable delay are highly required for the phased array system. The Vernier DLL-based clock generator is proposed to generate multi-phase clocks for the applications in true-time delay wideband FMCW phased array radar. The

phase delay, time resolution and operating frequency are programmable to meet the variable requirements of phased-array transceivers [123].

3.5.2 Vernier-Based DLL Architecture

Generally, a typical DLL consists of voltage-controlled delay line, phase/frequency detector (PFD) and charge pump (CP). VCDLs are used to generate a series of delayed signals. And then the phase difference between the reference clock and the delayed signal at the end of the delay line is compared by PFD. According to the phase difference, CP generates the corresponding voltage to control the delay of the delay line. If a delay difference from one clock period is detected, the feedback of the loop will tune the delay to ensure the locking status of the loop. The resolution of the DLL is therefore limited by the delay time of voltage-controlled delay cells (VDCs) in the delay line. To obtain a better time resolution, the concept of an array of DLL has therefore been proposed. The proposed chip implementing Vernier DLL architecture is fabricated by TSMC 40nm CMOS process. The proposed design adopts the principle and can be considered as an improved version of the topology. As shown in Fig. 3.23, it consists of five DLLs with the same configuration and very small phase difference between each other. One DLL works as the primary loop and the others are used as the secondary loops. In each loop, the stage number of the VDCs can be adjusted from 7 to 20 by the block multiplexer (MUX), which is controlled by digital bit SEL_0 , SEL_1 , SEL_2 and SEL_4 . Assuming the stage number in the primary loop is J and K , L , M , N in the secondary loops, respectively. When the loops get locked, the corresponding delay steps in the VCDLs are

$$T_J = T_{ref}/J, T_K = T_{ref}/K, T_L = T_{ref}/L, T_M = T_{ref}/M, T_N = T_{ref}/N, \quad (3.17)$$

where T_{ref} is the period of the reference clock. Equation (3.17) demonstrates the potential

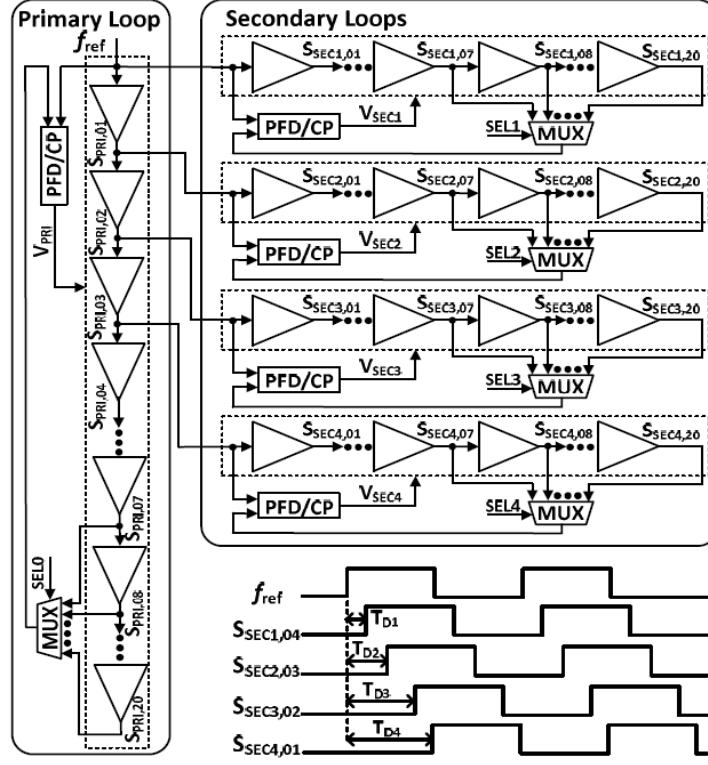


Fig. 3.23. The structure of the Vernier architecture DLL [123].

of the flexibility of the multi-phase generator design. For example, when the loops get locked, the time delay between SSEC1,04, SSEC2,03, SSEC3,02, SSEC4,01 in the secondary loops are provided as follows:

$$TD_1 = 4T_{\text{ref}}/K, \quad (3.18)$$

$$TD_2 = 3T_{\text{ref}}/L + T_{\text{ref}}/J, \quad (3.19)$$

$$TD_3 = 2T_{\text{ref}}/M + 2T_{\text{ref}}/J, \quad (3.20)$$

$$TD_4 = T_{\text{ref}}/N + 3T_{\text{ref}}/J. \quad (3.21)$$

Therefore, the delay difference between two adjacent secondary loops is expressed as:

$$TD_2 - TD_1 = T_{\text{ref}}/J + 3T_{\text{ref}}/L - 4T_{\text{ref}}/K, \quad (3.22)$$

$$TD_3 - TD_2 = T_{\text{ref}}/J + 2T_{\text{ref}}/M - 3T_{\text{ref}}/L, \quad (3.23)$$

$$TD_4 - TD_3 = T_{\text{ref}}/J + T_{\text{ref}}/N - 2T_{\text{ref}}/M. \quad (3.24)$$

Equations 3.22 to 3.24 demonstrate the mechanism that high time resolution can be achieved by adjusting the value of J , K , L , M , N and configuring reference frequency f_{ref} . Specifically, to generate equally spaced 4-channel clock signals, the value of K , L , M , N can be set the same. Then the delay difference between two adjacent channels is expressed as

$$\Delta T = TD_2 - TD_1 = TD_3 - TD_2 = TD_4 - TD_3 = T_{\text{ref}}/J - T_{\text{ref}}/K. \quad (3.25)$$

According to (3.25), when the reference frequency is 1GHz, the calculated relationship between J , K , and delay time is shown in Fig. 3.26. By adjusting the values of J and K , the delay time is configurable from 2.63 ps to 92.86 ps.

3.5.3 Circuit Implementation

The key circuit blocks including the delay cell and the charge pump are investigated in detail in this section, where the simulation results are demonstrated. The circuit of the basic delay cell in the VCDLs is shown in Fig. 3.24(a). The gate voltage V_{tune} is utilized to regulate the tail current to perform different delay time. In the locked loops, V_{tune} is provided by CP and is determined by the cell number in VCDLs. Fig. 3.24(b) presents the simulation results of V_{tune} versus delay time, which exhibit a reverse relationship between them. The operating voltage is from 0.4 V to 1 V with delay time from 884 ps to 47 ps, achieving a wide tuning range with coarse time resolution. Fig. 3.25. shows the structure of charge pump in this work, which covers the operating voltage of VCDC and exhibits good linearity between phase difference and output voltage. Transistors MP1, MP2, MP3, MP4 and MN1, MN2, MN3, MN4 work as current mirrors to provide currents I_{up} and I_{dn} , respectively. Four CMOS switches

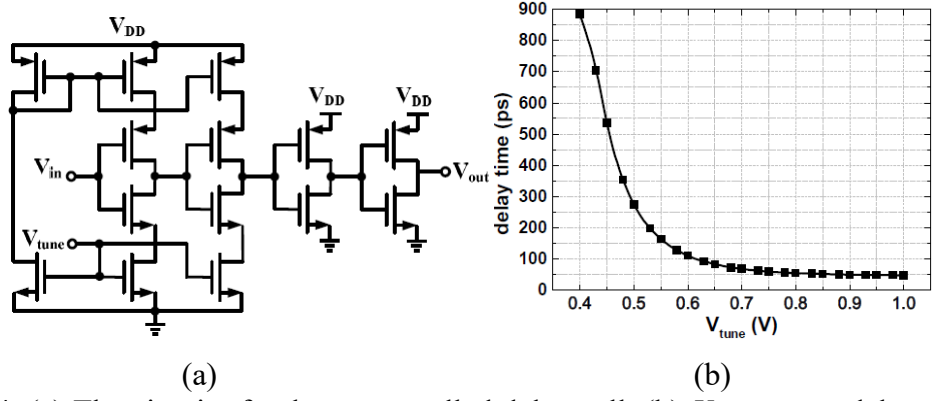


Fig. 3.24. (a) The circuit of voltage controlled delay cell. (b) V_{tune} versus delay time in VCDC [123].

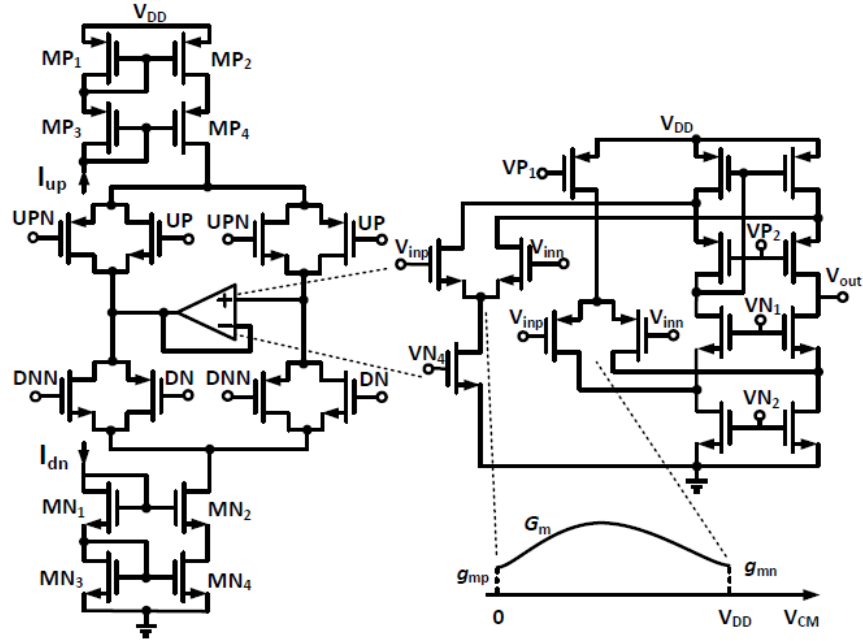


Fig. 3.25. The circuit of charge pump [123].

reducing charge injection effect and a unity-gain feedback amplifier are composed of bootstrapping circuit to remove charge sharing effect. A folded-cascode amplifier is employed to enable enough gain, wide output voltage range as well as stability. To extend the input common mode range, both NMOS and PMOS differential pairs are used to provide high transconductance G_m , which is a combination of g_{mp} and g_{mn} .

3.5.4 Testing and Measurement Results

The measured error from test ports caused by chip package and bonding wire of the test PCB board is taken into consideration, which is about 9ps. Therefore, the

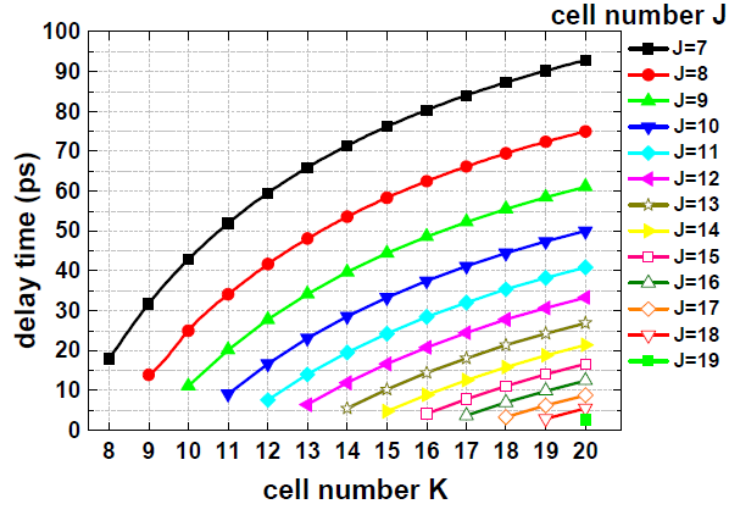


Fig. 3.26. Cell number vs. delay time (J is the cell number in primary loop and K in secondary loops) [123].

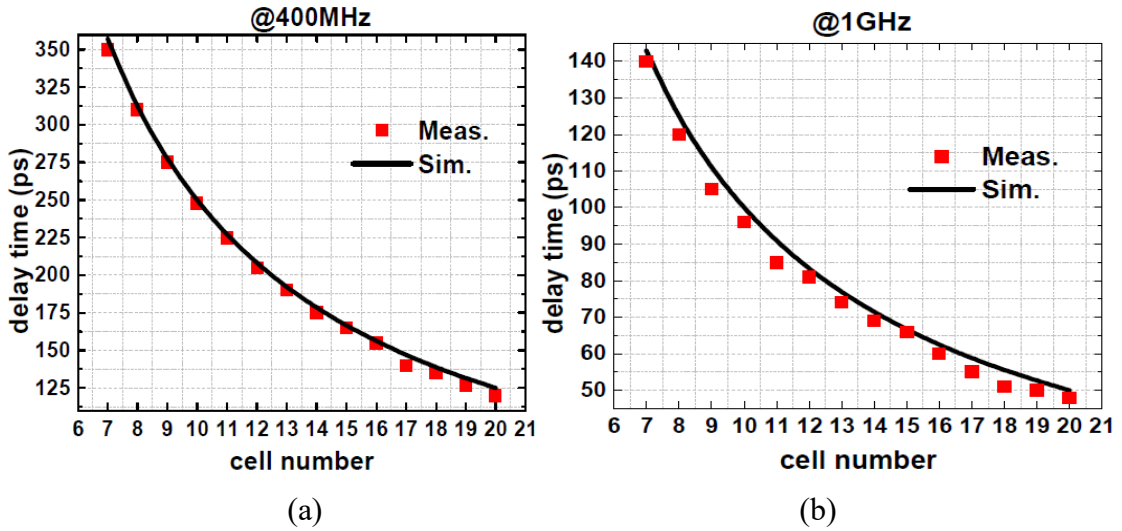


Fig. 3.27. The simulated and measure delay time (a) at 400MHz, the simulated and (b) measure delay time at 1 GHz [123].

calibrated delay time is 141 ps which highly meets the simulation results. Fig. 3.27 gives the measurement results as well as simulation results when the frequency of reference clock is 400 MHz and 1 GHz, respectively. When the operating frequency is extended to 2.5 GHz, the measured maximum cell number working in the VCDL is 10 with a minimum delay time of 40 ps.

For the application in real scenarios, the output signals of the 4-channel true-time-delay for wideband FMCW phased array radar are measured. When the frequency of reference clock is 1GHz, Fig. 3.28 shows the measured delay time of a single DLL with



Fig. 3.28. Measured delay time at 1GHz with 7-stage VCDL [123].

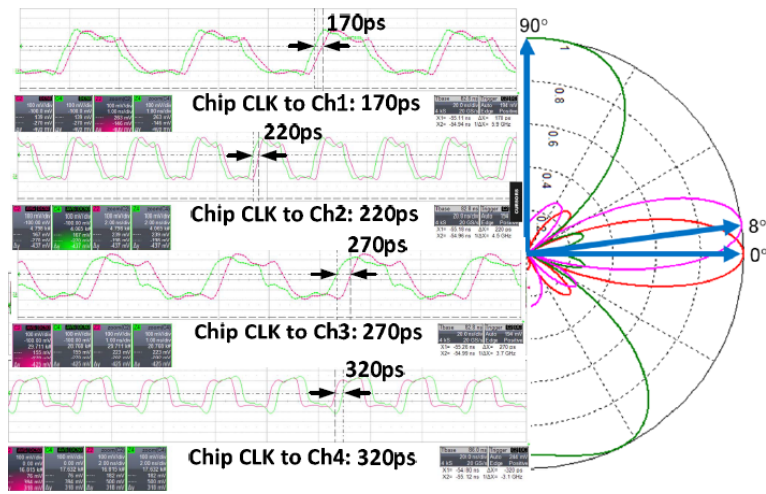


Fig. 3.29. The measured 4-channel outputs and the synthesized radiation pattern [123]. a 7-stage VCDL. When the frequency of reference clock is 400 MHz, the measurement results with 7-stage VCDL in the primary loop and 8-stage in the secondary loops are shown in Fig. 3.29. It is meaningful to calculate the delay time difference between the adjacent channels, which is measured to be 50 ps. Therefore, the calibrated difference is about 41 ps comparing to the simulated result of 42.5 ps, which agrees well. By configuring the cell numbers in VCDLs and adjusting the reference frequency, the measured delay time difference is in the range from 7 ps to 108 ps. When employed in *X*-band phased array radar sensor applications, the true-time delay can be mapped into a radiation pattern. The synthesized radiation pattern for a 10 GHz phased array system

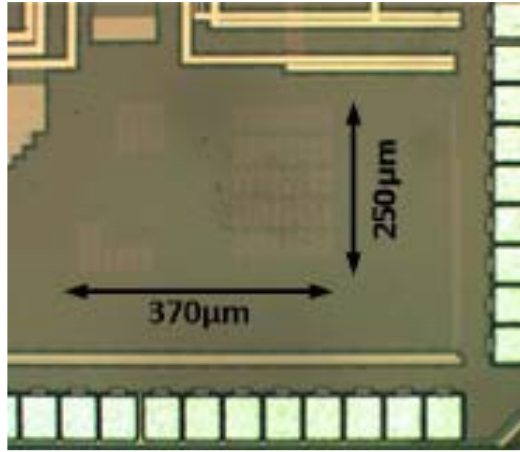


Fig. 3.30. Die photograph of the Vernier DLL [123].

Table 3-5. Performance Comparison of the DLL Clock Generator.

Feature	JSSC 1996 [78]	JSSC 2012 [79]	JSSC 2013 [80]	This Work
<i>Architecture</i>	DLL Phased Array	Vernier Delay Line	DLL with Interpolation	DLL Phased Array
<i>Supply Voltage (V)</i>	n.a.	1.2	2.5	1.1
<i>Power (mW)</i>	n.a.	n.a.	n.a.	20.9
<i>Reference Frequency (MHz)</i>	65	200	1470	400-2500
<i>Resolution (ps)</i>	154	10	6	7@0.4GHz
<i>Tuning Range (ps)</i>	Fixed	700	425	230@0.4GHz 400@ 1GHz
<i>Multi-Phase output</i>	Yes	Yes	No	Yes

with $\lambda/2$ antenna pitch is shown in Fig. 3.29. To reduce the quantity of layout PADs on chip, all digital bits are controlled by SPI. The die photograph is shown in Fig. 3.30. The performance comparison of clock generators used in the transceiver is summarized in Table 3-5 [78]-[80]. It has to be noted this is a preliminary prototype for verifying functions of multi-clock generation for the phased-array systems.

3.6 Chip-Scale 1TX-1RX *Ku*-Band FMCW Radar Sensor for Respiration Monitoring, Falling Detection, and Motion Recognition

In this section, the one-channel *Ku*-band FMCW radar sensors for respiration monitoring, falling detection, and motion detection are illustrated. Compared to the

phased-array radar sensors, one-channel radars do not need the Vernier DLL to generate multiple clocks for different channels of the phased-array; thus, they can operate with a reduced complexity, lower power consumption, and easier deployment. The main tradeoff is that the detection FoV and the range of the one-channel radar is limited; therefore, multiple radar sensors need to be deployed to cover wide FoV sensing.

3.6.1 Chip-Scale *Ku*-Band Radar Sensor Architecture

It is observed that the Doppler frequency shift will happen when the objects move away or toward the radar [6]. As a rule of thumb, for a radar operating at 15 GHz (i.e., wavelength of 2 cm), a micro-movement of 2 cm maximum displacement with about 2 cm/s velocity can only induce a micro-Doppler frequency shift of 2 Hz, (according to the equation: $f_d = \frac{2}{c} f_t V_{(t)}$), which is too tiny to be directly detected with high accuracy in the frequency domain. However, such micro physiological movements induced micro-doppler frequency shift will accumulate in the time domain, generating a corresponding phase variation, which can be utilized to recover the corresponding micro physiological movement information with high sensitivity compared to the micro-doppler frequency analysis method. The returned signal phase contains the information of distance between radar and object, radial velocity, and the corresponding micro-doppler frequency shift. To extract these parameters simultaneously with high accuracy, the linear frequency-modulated continuous-wave (i.e., FMCW) micro-radar in this design transmits the wide-bandwidth (1 GHz) chirp signal with 15 GHz center frequency and receives the returned microwave signals which possess different spectral contents. The signals are co-registered to the same object, which can provide separate records [9] on the target object's parameters. However, the complexity of the radar front end and signal processing unit increases significantly with the use of high speed, high power circuits

working at several gigahertz. Such complexity results in difficulty on realizing the accurate and real-time tracking of the micro-physiological signals. The returned chirp signal is first mixed with the transmitter signal to de-chirp itself into an IF waveform while still holding the phase information, since the transmitted and returned waveforms are highly correlated. Then the blocks in the receiver front end will work at IF frequency, reducing the design complexity of the RoC and the power consumption [35].

An FMCW micro-radar successively transmits chirps to the target and receives echoes, followed by the dechirp process to extract IF beat frequencies, f_b . The frequency of the IF signal is proportional to the detecting range R . Practically, to make the RoC work in optimum condition, several degradation effects need to be addressed. Since the transmitter and receiver antennas are close to each other, one important issue is the strong IF interference from the direct antenna leakage at de-chirped beat frequency. To eliminate the effect, the de-chirped waveforms will first undergo a low-pass filter before the phase analysis [35]. Another issue is the amplitude ripples of the RF signals at the transmitter and the receiver front end, which will result in the deterioration of the spectrum at the beat frequencies. The inferior ripple performance impedes the radar's ability on distinguishing tiny object movements. The ripple of the output chirp signal in the radar chip is mainly caused by the accumulation of variations in the VCO output voltage as well as the variations of PA gain at different frequencies of the chirp waveform. In this work, the ripple effects are minimized through using the two-stage, saturated driven amplifier power amplifier (DA-PA) in the Tx frontend and low noise amplifier (LNA) chain circuits in the Rx frontend. A two-stage input-load peak-staggering LNA is used in the radar RXFE to enhance the flatness of the signal [110].

The whole radar sensor architecture is demonstrated in Fig. 3.31, starting from the VCO in the chirp synthesizer, the output signal is divided by eight from the three

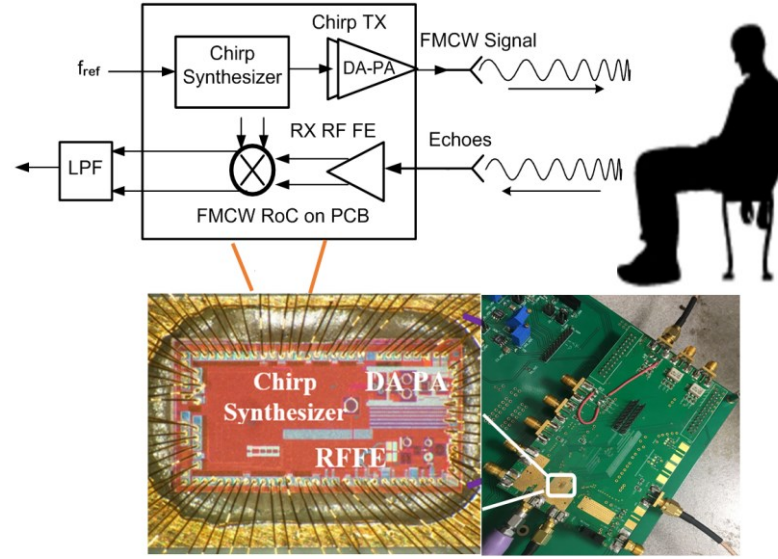


Fig. 3.31. Chip-scale FMCW radar sensor architecture [35].

cascaded current mode dividers [35]. Thereafter, the phase of the divided signal is captured and digitized by the digital phase detector consisting of a counter and a fractional time-to-digital converter. The phase difference is transformed into a frequency word by a time-to-digital converter in the chirp synthesizer. Then the signal is transmitted from the driven amplifier, power amplifier chain. The prototype radar transceiver chip is implemented in 65 nm CMOS process. The chip was wire-bonded onto a testing print circuit board (PCB) using chip-on-board technology. R4350B material is used for the PCB substrate to ensure high-frequency performance for the healthcare applications. As the physiological micromovements induced signal is very tiny with low frequency, it is difficult to be detected directly using doppler frequency shift or ISAR imaging [38]. Considering that the phase information, which is the integration of frequency shift in the time domain, is highly sensitive and correlated to the tiny movements of the objects [37], the phase information is analyzed in time domain to recover the corresponding essential physiological signals.

3.6.2 Experiments on Monitoring Breathing and Falling

The physiological signals like heartbeat and respiration, ΔR_t can be approximately expressed as a sinusoidal waveform with the same frequency to the period of physiological signs, which is between 0.2 Hz to 0.5 Hz for respiration and between 1 Hz to 2 Hz for heartbeat. The de-chirped signal from the receiver by coherent mixing will be further correlated to the sinusoidal signal generated from the DFS, which is at the same frequency to the de-chirped signal's center frequency. In the time domain, when the micromovement is towards the chip-scale radar sensor such as inhale process, the phase rate gradient will increase, when the micromovement is away from the radar sensor such as exhale process, the phase rate gradient will decrease. In the experiments, the chirp repetition rate takes 960 Hz and the chirp waveform takes 15 GHz center frequency with 1 GHz bandwidth. The reference signal for the de-chirped signal is a sinusoidal waveform whose frequency is same to the de-chirped signal's center frequency, taking the cable into account, which is 34.67 KHz, which is obtained by the multiplication of the chirp rate and the time delay caused by the two cables. The interferometry phase waveforms in time domain exactly correspond to different kinds of vital sign induced micro-movements. To ensure the chip-scale radar to work in the optimum status, an off-chip crystal oscillator is used to generate the 250 MHz reference clock to the chirp synthesizer. With the setting of 15 GHz center frequency, the measured TX output power is 9 dBm, where around 4.3 dB aggregate loss is estimated from the PCB metal trace, the SMA connector and the coaxial cables used in this experiment. The chip-scale radar sensor system setup is illustrated in Fig. 3.32, where the wireless healthcare monitoring applications are verified. A pair of horn antennas with 14 dBi gain and about 30° 3-dB beam-width were pointed towards the subject in this experiment. A person was seated in front of the radar at 1 m distance to test the

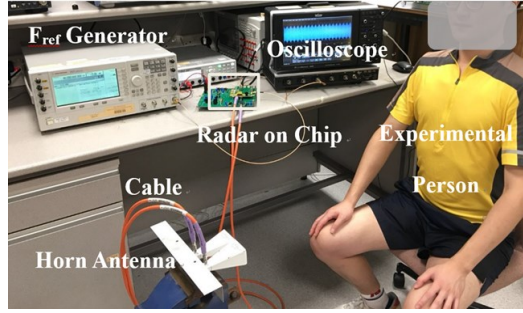


Fig. 3.32. Radar sensor experimental setup [35].

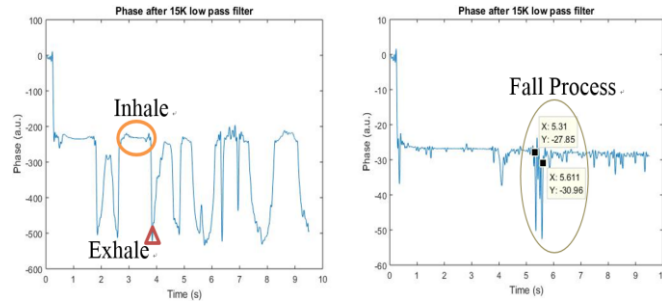


Fig. 3.33. Preliminary results on respiration rate and falling monitoring [35].



Fig. 3.34. An illustrative indoor scenario of the one-channel chip-scale FMCW radar sensors deployed for pervasive healthcare monitoring.

radar's function on monitoring the heartbeat, respiration rate and detecting the falling.

The acquired de-chirped intermediate-frequency signal after the mixer in the receiver is further processed by the interferometry phase analysis algorithm to extract the features of micro physiological movements in real time. Clearly, the phase shift in Fig. 3.33 (left) reflects the respiration micro-movements in the time domain where the circle in the figure represents an example of the inhale process and the triangle represents an example of the exhale process, which is shorter in time compared to the inhale process. The respiration rate of the person in the experiment is higher during the period from the 4th

second to the 7th second, which is reflected in the phase figure. The emulated falling process can also be clearly seen from the time domain phase shift in Fig. 3.33 (right), where the abrupt phase change occurring at 5.31 second to 5.61 second corresponding to the experimental fall-forward process at that time. Particularly, the combination of both the chip-scale FMCW radar frontend and the backend phase analysis algorithm in our design realizes the wireless sensing on the micro physiological signals with high accuracy and low power. Since the computation complexity of interferometry phase analysis algorithm is relatively low, the algorithm can be further integrated into the chip-scale radar system as a DSP module to further miniaturize the sensor system. Multiple chip-scale radar sensors can be deployed in different positions in the room to achieve wide field-of-view sensing coverage, where the scenario is illustrated in Fig. 3.34.

3.6.3 Chip-Scale Radar Sensor for Noncontact Motion Detection

Noncontact motion detection can be enabled by chip-scale radar sensor. In this chapter, two radar transceivers operating at *Ku*-band are used for accurate noncontact motion detection. These radar transceivers are of complete design employing blocks from frontend to backend and support high-resolution synthetic aperture radar imaging, aiming at the application in human activity sensing. Frequency-modulated continuous wave scheme is adopted for both radar transceivers, free of range-ambiguity while taking the advantages of narrow IF for low-power consumption.

The radar sensor can be leveraged to detect the motions, showing the potential on seamless noncontact human-machine interface applications. The radar chip is mounted on a PCB for evaluation. The blocks and chips were tested individually, and the results are presented and discussed in [3]. The human motion detection experiment is setup as in Fig. 3.35(a). The subject is located about 1.5 m away from the antenna of the radar

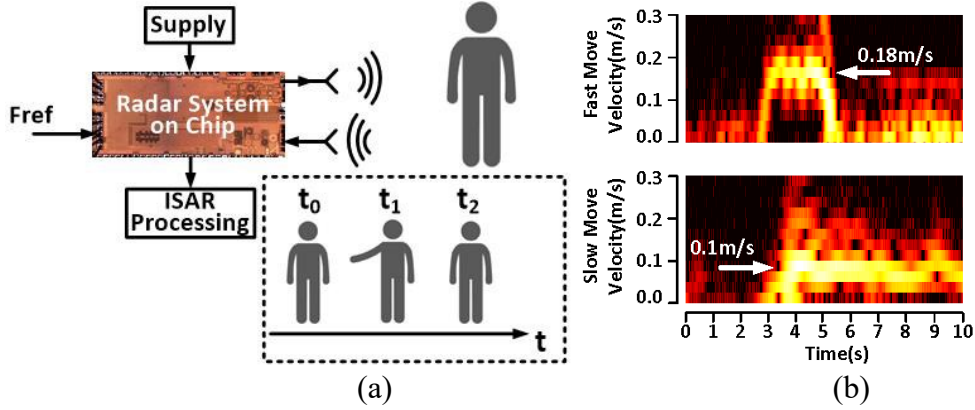


Fig. 3.35. (a) The setup of the motion detection using the chip-scale radar sensor and (b) The detection on the hand motions [121].

system prototype based on the chip presented above. The one of the arms is move towards and away from the antenna. The Doppler information can be extracted from the de-chirp IF signal, indicating the movement velocity. As shown in Fig. 3.35(b), the arm moving in different velocity can be sensed. The phase change of the de-chirping IF signal is mapped into the velocity versus time as the bright traces in the figures. A fast move with a velocity about 0.18 m/s and a slow move with a velocity about 0.1 m/s are observed, showing that the arm motions are correctly recorded by the chip-scale radar system. The human motion experiments are conducted, where the Doppler information of the motion is recorded and mapped to sense the motions. The recognizing on the two different motion patterns was attained in the experiments with Doppler processing [121].

3.7 *I/Q*-based Coherent Radar for Enhanced Detection Capability

To enhance the radar's capability on detecting tiny signals, a digital-enhanced chip-scale radar sensor prototype is proposed in this section, where a novel quadrature interferometric phase analysis algorithm is proposed to be leveraged to improve the performance of the radar system. The radar sensor demonstrated the potential to achieve localization on target subject and monitoring of multi-modal physiological signs through the interferometric phase analysis method. In-phase and quadrature templates

are adaptively generated and correlated with the de-chirped signal at the receiver to extract the micro physiological signs, which can be realized by an FPGA [122]. To extract the phase information, the de-chirped signal from the receiver will be further correlated with template sinusoidal and cosine waveforms respectively, where the templates are with the same frequency to the intermediate frequency of the de-chirped signal. Then, the processing of the correlation results of the received signal with I and Q template are implemented every modulation period, which is indicative of the interferometric phase information related to healthcare information.

$$I_{temp}(t) = \cos(2\pi f_{IF}t), \quad (3.26)$$

$$Q_{temp}(t) = \sin(2\pi f_{IF}t), \quad (3.27)$$

$$\varphi(t) = \arctan\left(\frac{I(t)}{Q(t)}\right), \quad (3.28)$$

The phase information is obtained by processing the I channel and Q channel signal. In the time domain, when the micromovement is approaching the radar, the extracted phase difference after quadrature interferometric phase analysis algorithm will increase, when the micromovement is moving away from the radar, the achieved interferometric phase difference will decrease. Through the I/Q detection, the effects from interferences and noise would be further suppressed. It has to be noted that this is a proposed promising direction for future mixed-signal chip-scale radar design while the complete mixed-signal system hasn't been completed [122].

3.8 Summary

A complete CMOS-integrated phased-array radar sensor for subject localization, multimodal vital sign monitoring, and falling detection is presented. The accurate beam-steering is realized by configuring both the true-time delay clock in MPS and the RF

phase shifters on-chip. As the radar sensor works in coherent mode for short-range detection, the effect of phase noise is small. The broadband Vivaldi antenna array is employed to support the high gain and the directivity of *X*-band chirp beam-steering. The effective ITPA algorithm is leveraged to discern multimodal vital signs and detect falling. The experiments with human subjects have demonstrated that the highly-integrated coherent radar sensor can enable the localization of subjects and monitor healthcare conditions in a wide FoV, paving the way for pervasive edge health status monitoring applications in current COVID-19 pandemic and future intelligent IoE era.

A configurable DLL-based clock generator fabricated in TSMC 40-nm CMOS technology with high resolution and wide operating range for true-time-delay wideband FMCW phase-arrayed radar sensor is presented. The chip consumes about 20.9 mW at a 1.1 V power supply. The measurement results demonstrate that the Vernier-based DLL can operate from 400 MHz to 2.5 GHz. The DLL-based clock generator can enable a 7 ps resolution at 400 MHz operating frequency. By adjusting the cell numbers in the VDCs, the clock generator can be configured flexibly to cover the operating frequency of the phased-array transceivers.

The 1TX-1RX FMCW radar sensor chip for vital signs detection and falling detection is presented, which achieved 1 GHz chirp bandwidth at 15 GHz center frequency. With a 1.2 V supply, the radar front end consumed 238 mW power consumption. A simple interferometry phase analysis algorithm has been proposed to accurately detect the micro-movements based on the signal from the radar sensor's receiver. The experiments reveal that the prototype radar sensor chip can distinguish the respiration rate, falling, and hand motions of the subject.

Chapter 4

Digital-Enhanced Chip-Scale Photoacoustic Sensor System for Blood Core Temperature Monitoring and *In Vivo* Imaging

In Chapter 3, CMOS-integrated coherent radar sensor systems have been presented to enable the noncontact detection on vital signs like respiration rate and heartbeat rate, and the monitoring of specific movements like falling and gestures. Moreover, to ensure the continuous, pervasive monitoring on health status and the potential disease diagnosis, non-invasive sensing on blood cell temperature and *in vivo* imaging on vessels are essential. Monolithic integration of photoacoustic (PA) sensor with compact size, lightweight, and low power consumption is promising for realizing portable or wearable medical devices. By the coherent detection techniques enabled by the proposed novel mixed-signal ICs, *in vivo* blood temperature sensing and imaging with improved SNR and suppressed interferences can be achieved.

This chapter is organized as follows: Section 4.1 presents the background of PA sensor for physiological signs monitoring. In Section 4.2, the digital-enhanced silicon-based PA sensor system's analysis and design considerations are elaborated. Section 4.3 shows the implementation of the photoacoustic sensor frontend, and the digital algorithm realized on a field-programmable gate array (FPGA) is illustrated. In Section 4.4, the chip characterizations and the experimental results are presented. A coherent quadrature I/Q tracking PA sensing system is demonstrated in Section 4.5. A 4-channel fully integrated PA SoC is shown in Section 4.6. The summary is drawn in Section 4.7.

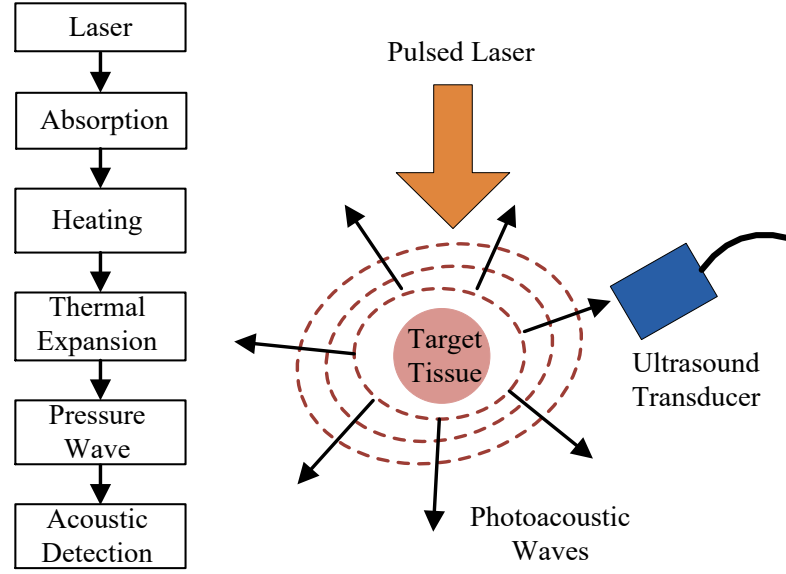


Fig. 4.1. Illustration of photoacoustic effect.

4.1 Photoacoustic Sensor for Physiological Sign Monitoring

This chapter presents a miniaturized chip-scale mixed-signal photoacoustic sensor system which can achieve coherent lock-in function to detect weak target PA signals noninvasively at *in vivo* scenarios of poor signal to noise ratio (SNR) and strong interferences. A low-noise amplifier (LNA), a 3rd order Butterworth low-pass filter (LPF), and a variable-gain amplifier (VGA) chain with 10 MHz cutoff frequency are implemented on-chip to attain a high-quality sensing performance with 50-dB dynamic range. A Gilbert-cell type multiplier is integrated on-chip to fulfill the coherent lock-in process on acquired PA signals in a closed-loop process with an embedded FPGA system. Fabricated in 65-nm CMOS technology, the prototype PA sensor system demonstrated 50 μV sensitivity. The functions of the chip-scale PA sensor system enhanced by coherent lock-in process were validated through the experiments on temperature monitoring and vessel imaging. The PA receiver chip occupies 0.6 mm² area and consumes 20 mW including testing buffers at a 1.8-V supply. For one-channel

PA sensing operation, the minimum power consumption can be configured at 16.1mW. For *in vivo* PA sensing and in-depth imaging applications, several specifications like detection depth, sensitivity, specification, and the safety requirements need to be considered seriously. Photoacoustic (PA) sensor technology is going to play a more and more critical role on *in vivo* healthcare applications considering its capability to achieve the high optical contrast based on the PA effect, which can enable the high-quality imaging [44]-[56]. The PA effect is illustrated in Fig. 4.1, the absorption of the laser by the target will induce a transient thermoelastic expansion with an associated ultrasound emission. Photon absorption and subsequent nonradiative relaxation by chromophores will induce a rapid rise in temperature inside the target. If using a pulsed laser with a pulse duration shorter than the target's thermal and stress confinement time, the thermal energy exchanging with the surroundings will not happen. The energy deposition occurs within a shorter timescale compared to the mechanical displacements, which are caused by the strain within the target [44]. The isochoric heating will raise the pressure within the target, which can be expressed by $\Delta p = \Gamma \mu_a F$, where Γ is the Gruneisen parameter, μ_a is the optical absorption coefficient of the tissue, and F is the incident laser fluence [53]. The pressure rise will lead to a thermoelastic expansion, and the emission of a pressure wave called a photoacoustic wave. The broadband photoacoustic wave carries the information correlated to the geometrical properties of the absorbing structures, which can be expressed as the inhomogeneous wave equation expressed as

$$\left(\nabla^2 - \frac{1}{v_s^2} \frac{\partial^2}{\partial t^2} \right) p = -\frac{\beta}{C_p} \frac{\partial H}{\partial t}, \quad (4.1)$$

where β is the thermal expansion coefficient of the target, v_s is the propagation speed of the ultrasound waveform, C_p is the specific heat capacity, and H is the function describing the heating of the target in time and space [46]–[48]. The solution to the wave equation is derived from the Green function, which is expressed as

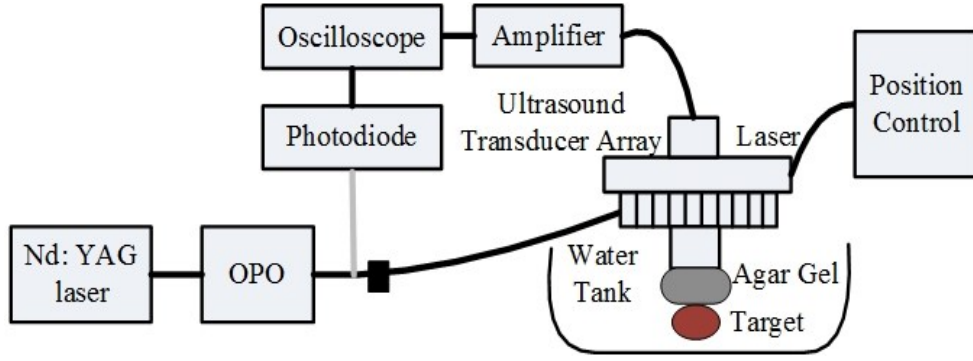


Fig. 4.2. A conventional photoacoustic sensor system with commercial transducer.

$$p(r,t) = \frac{1}{4\pi v_s^2} \frac{\partial}{\partial t} \left[\frac{1}{|r-r'|} \int dr' H(r', t - \frac{|r-r'|}{v_s}) \right], \quad (4.2)$$

which describes the pressure from the sources at location r and time t over a spherical shell target centered at r with a radius of $|r-r'|$. Considering the ultrasonic scattering at *in vivo* scenarios is about one thousand times weaker than optical scattering, PA sensor can achieve images with the acoustic resolution at a depth beyond the limitation from the effect of optical diffusion [51].

A conventional PA sensor system is shown in Fig. 4.2, where a tunable laser is used to illuminate the target, an ultrasound transducer array is used to acquire the echoed pulse signals and form the PA images, and a motorized stage is used to move the transducer [51]. However, the imaging and sensing functions are implemented using commercial discrete components in the system, which is bulky in size and is at a high cost. To achieve the portable and configurable characteristics for compact-sized wearable devices, a digital-enhanced chip-scale PA system with the coherent lock-in for detection enhancement is presented in the paper. The pulsed laser is adopted in the system to induce ultrasonic signals from the in-depth tissue considering that pulsed excitation can generate much stronger PA signals. In the reported ultrasound/PA sensor systems [45]-[50], [61]-[65], multi-channel circuits are leveraged to realize the detection

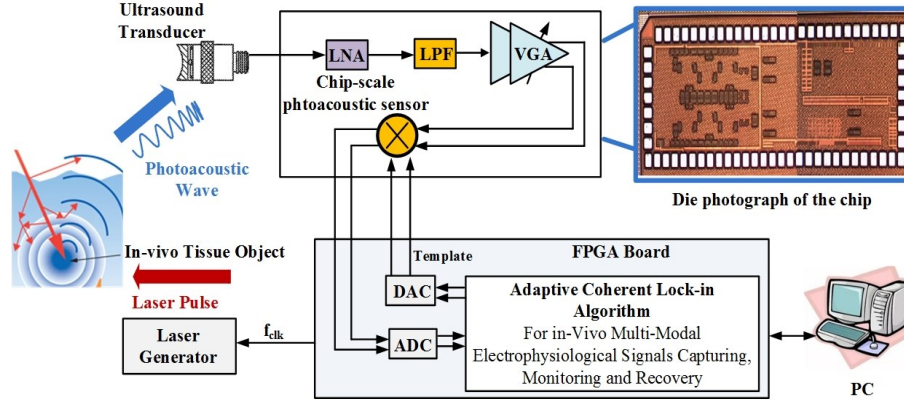


Fig. 4.3. System diagram of the proposed chip-based coherent lock-in photoacoustic sensor system for *in vivo* physiological signal sensing and in-depth imaging [120].

on the signal with beamforming, which requires a large area and is with high power consumption. The sensor systems are working in an open-loop way where the analog frontend and digital processing are designed separately.

Different from the reported techniques, a novel digital-enhanced coherent lock-in technique is implemented in the proposed system, where the implementations of the template waveforms are configurable in the digital domain to enhance the sensing and imaging performances for different application scenarios. The proposed technique will improve the sensitivity, specificity, and accuracy of the chip-scale PA sensor system. The prototype mixed-signal PA sensor chip has been fabricated in 65-nm CMOS technology with an area of 0.6 mm^2 , where most of the electronic functions of the PA sensing system are integrated on-chip. At 1.8-V supply, the front end of the sensor chip consumes 20 mW, which is configurable. Besides performance analysis on the circuit, the prototype sensor system is validated through temperature sensing and *in vivo* imaging experiments.

4.2 Chip-Based PA Sensor System Architecture

As illustrated in Fig. 4.3, the diagram of the proposed novel chip-scale PA sensor

system contains the sensor analog front end (AFE), the FPGA board, the analog-to-digital/digital-to-analog (AD/DA) board, the pulsed laser, and the PC. The coherent lock-in and recovering on the target PA signals can be fulfilled in a closed-loop way, demonstrating the capability of *in vivo* monitoring on various kinds of physiological signs such as blood core temperature, oxygen saturation and imaging with improved SNR and contrast, enhanced specificity and small form factor.

4.2.1 Sensor System for Coherent Photoacoustic Detection

A 1064 nm Nd: YAG laser is implemented to irradiate the target, and the emitted photoacoustic waves were acquired with the ultrasound transducer connected to the PA sensor chip. The transducer is attached to the tested tissue immersed in a water tank. For example, in the experiments for imaging, the transducer is pressed against the hand blood vessel. The interferences produced by tissues reflections and surrounding noise are suppressed by a 3rd order Butterworth low-pass filter (LPF) considering its flat frequency response characteristic within the passband. A variable gain amplifier (VGA) is integrated on-chip to support up to the 50-dB dynamic range for input signals with different amplitudes. The on-chip Gilbert cell multiplier reduces the system's requirement on bandwidth, sampling rate, and clock frequency in both the analog front end and the digital processing enabled by the FPGA board.

The capturing and recovery on target PA signals are achieved by the mixed-signal closed-loop processing, enhancing the SNR and specificity of the PA sensor for detecting the weak target signals employing the coherent lock-in technique. The coherent lock-in for photoacoustic signals is realized in two phases. The first phase is to capture the target photoacoustic waveform, aiming at obtaining the initial and coarse timing synchronization. The second phase is the tracking, aiming at fine-tuning the delay

to locate the target signal position in the time domain continuously. In our design, the coherent lock-in for the photoacoustic signal is realized based on the combination of the analog front end and the digital algorithm implemented in FPGA through the high-speed mezzanine card (HSMC) interface. The depth of the target is determined by the time delay between the laser trigger and the echoed PA signals to the transducer. Practically, the following design methodologies and parameters are addressed for the chip-based *in vivo* temperature monitoring as well as imaging applications.

As derived from (4.2), τ is the time interval from the moment that the induced ultrasound signal is transmitted to the moment that the corresponding ultrasound waveform from the target reaches the transducer, which is calculated as

$$\tau = \frac{R}{v}. \quad (4.3)$$

Here R is the range between the target and the transducer, v is the velocity of the ultrasound waveform in the tissue. The photoacoustic signal $p(t)$ after the transducer can be considered as composed of three parts: the target PA signal, the interference signal, and the noise, which can be modeled as

$$p(t) = p_{target}(t) + p_{interference}(t) + p_{noise}(t). \quad (4.4)$$

To extract the target waveform from the received signal, the template waveform is leveraged for matched filtering. By multiplying the template waveform and the received signal through Gilbert cell, the achieved waveform is expressed as

$$R(t) = p(t) * Temp(t), \quad (4.5)$$

where $Temp(t)$ is the template waveform stored in the random-access memory (RAM) on FPGA. It has to be noted that the template waveform can also be stored in read-only memory (ROM). Since a broad range of the target tissue depth leads to a wide dynamic range of $p(t)$. Also, various of vessel depths and physiological conditions of a subject

lead to changes of $p(t)$, thus the time delay τ of the template waveform generation needs to be adjusted adaptively to achieve the real-time alignment between the template and the target signal. For PA sensing applications, a depth typically ranges from 1 mm which corresponds to the skin surface, to 6 cm which corresponds to the in-depth target tissues, is favorable and the corresponding time interval τ is in the range from 0.64 μ s to 38.9 μ s. To provide a sufficient sampling rate to achieve the fidelity on the received signals, the analog to digital converter (ADC) board operating at 50 MHz with 14-bit effective number of bits (ENOB) is employed, which can provide sufficient timing and proper signal resolution for the proposed sensor system.

As indicated from (4.5), the received signal $R(t)$ after the Gilbert cell is determined by both the photoacoustic signal $p(t)$ and the template waveform $Temp(t)$. Thus, the overall dynamic range of the sensor is extended since the template waveform is configurable at the digital side. To alleviate the requirement of the ADC sampling rate and the data throughput, the highest frequency of the PA waveform after multiplication with template waveform is determined as 10 MHz. In this work, an iterative RAM-based lookup table (LUT) on FPGA is used to generate the template waveforms, which are then coherently aligned with the target signals in different application scenarios. The pulse repetition frequency (PRF) of the laser pulse is determined by the clock signal f_{clk} generated from the FPGA, which is configurable from 10 Hz to 2000 Hz, covering the range for different application scenarios including sensing and imaging on targets at different depths. The calibration is implemented on the digital side.

4.2.2 In Vivo Digital-Enhanced Coherent Photoacoustic Signal Detection Technique

The template waveform can be configured when the system works in the closed-

loop form enabled by mixed-signal circuits for target signal capturing and recovery, which is realized by the following three phases.

Phase 1 Template waveform extraction: To obtain the template waveform, the received PA signal is processed by the CPU in PC through the open-loop PA sensor. By summing N periods of the received pulsed PA signals, the weak target PA signal, which is initially masked by noise, can be recovered with improved SNR. The template PA waveform is stored in the RAM of FPGA. Considering the target signal presented within the gate window is added coherently while the noise is added randomly as the square root of the number of shots, the averaging with N shots will improve the signal-to-noise ratio (SNR) by a factor of \sqrt{N} , which is derived as [132]

$$SNR_{out} = \frac{S_1 + S_2 + \dots + S_n}{\sqrt{(N_1^2 + N_2^2 + \dots + N_n^2)}} \approx \frac{nS}{\sqrt{(nN^2)}} = SNR_{in} \sqrt{N}, \quad (4.6)$$

where the term S_i represents the target PA signal, and N_i represents the noise within each pulse period. After the summation and the gated function extraction, the unique template window with enhanced specificity and sensitivity for personal physiological PA signal is obtained. The critical issue related to the photoacoustic sensor system is the strong interferences due to the unnecessary reflections from the objects.

A typical received PA signal is illustrated in Fig. 4.4, where the weak target PA signal excited by a low-power laser is masked with noise and interferences. To extract the target PA profile as the template waveform, a high-power pulsed laser is leveraged to induce the PA signal from the blood vessel and the coherent summation of a tunable number of pulses, which ranges from 50 to 200 pulses depending on the applications, is implemented to obtain the template PA signal with enhanced SNR and suppressed interference. A normalized template PA waveform profile is illustrated in Fig. 4.5. For each application scenario, the template waveform needs to be acquired under strong

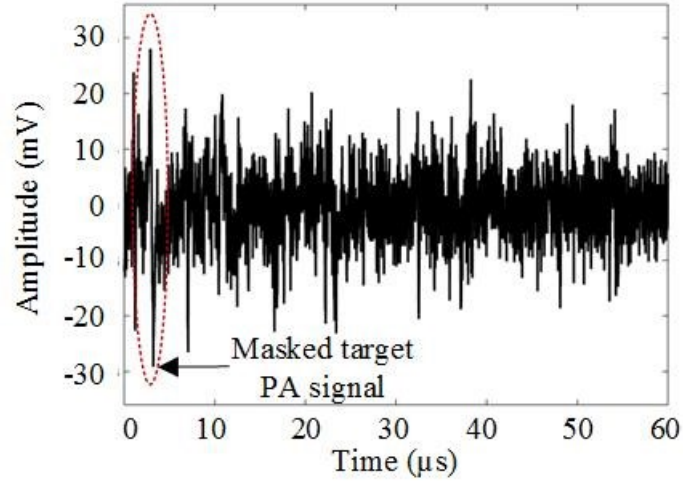


Fig. 4.4. Measured PA signal induced by a low-power laser under poor SNR and interferences environment.

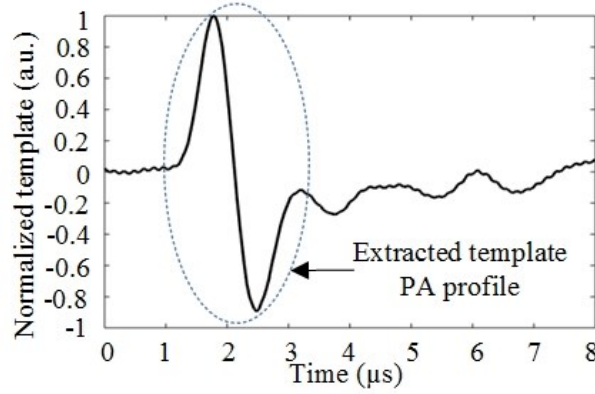


Fig. 4.5. Extracted target PA waveform profile under strong laser excitation processed by coherent summation and averaging.

laser excitation firstly, then the template waveform with high correlation coefficient to the target PA signal is leveraged to achieve the capturing and recovering on the target signal at *in vivo* scenarios.

Phase 2 Coherent lock-in on target PA signal: In real PA-based healthcare applications at *in vivo* scenarios, continuous and in-depth monitoring on target PA signals is required, where the digital-enhanced feedback needs to be implemented to enable the adaptive target waveform capturing, locking and recovery as illustrated in Fig. 4.6. For PA signal sensing applications, when the target's position is ensured, a processing window with configurable length is generated at a pulse repetition rate same to the pulsed laser; thus, only the target PA signal will be captured and processed,

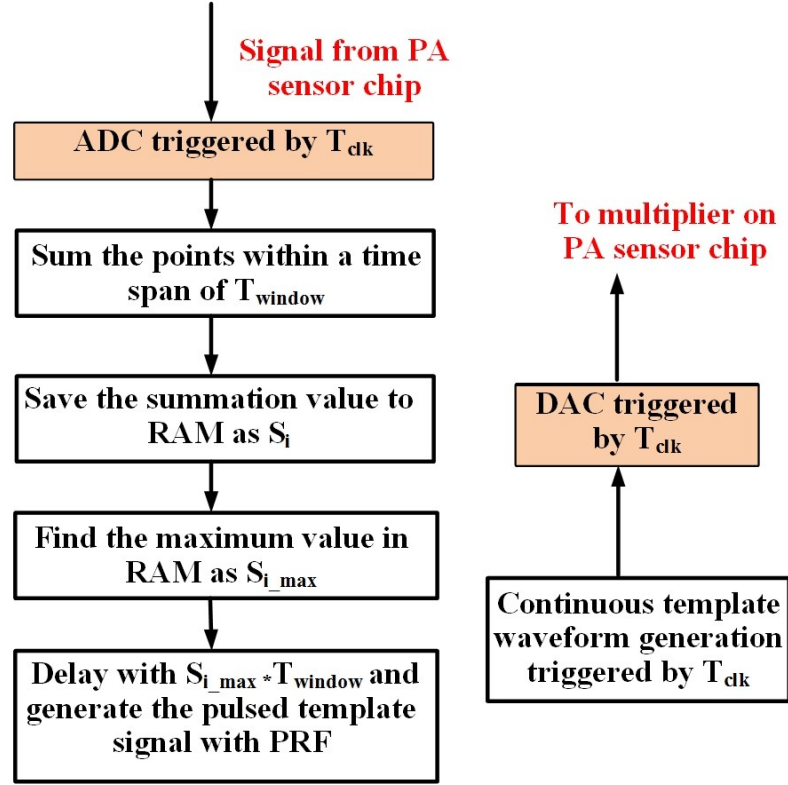


Fig. 4.6. Target PA signal capturing [120].

decreasing the overall computation complexity of the algorithm and decreasing the power consumption of the whole PA sensing system.

The continuous template waveforms are used for target signal capturing. After the capturing, the pulsed template trains are used to lock the target pulsed PA waveforms with the synchronized PRF. The FPGA and the PA sensor chip are implemented coordinately to lock and recover the repetitive and weak target PA signals. In the applications for sensing weak PA signals, a gate window with predetermined width T_{window} is tuned with a delay to align the template waveform with the target PA signal, which is of the pulse repetition interval (PRI) equaling to $1/PRF$. A gated integrator will amplify and integrates the signal within the time window while the noise and interference which are out of the window are ignored; thus, the computation complexity of the algorithms is reduced by PRI/T_{window} theoretically compared to traditional methods which process all the points within the pulse interval. For example, if the

T_{window} is 1 μ s, and the PRI is 0.5 ms, the computation complexity of the algorithm is reduced by 500 times.

Phase 3: Target waveform recovery: To reconstruct the target waveform with high fidelity and SNR, the adaptive reconstruction function is utilized, which can be expressed as

$$R_{rec}(t) = \frac{R(t)}{P_{target_norm}(\tau_{window})}. \quad (4.7)$$

The reconstructed waveform after the decorrelation process demonstrates the 99.69% Pearson correlation efficiency to the PA waveform from the target tissue under simulation when they are aligned accurately. Moreover, the value integrated within a window time can be served as the intensity indicator of the target PA waveform where the noise and interferences are suppressed during the integration process, which can improve the detection sensitivity of the sensor system.

4.3 Photoacoustic Sensing Chip System Implementation

The design and implementation details of the PA sensor system, which consists of the frontend integrated circuit and the digital algorithm implemented in FPGA and the AD/DA module are presented explicitly in the subsections.

4.3.1 Analog Front-End (AFE) of the Sensor Chip

The schematics of the key analog circuit blocks for the chip-scale PA sensor is shown in Fig. 4.7, where alternating current (AC) coupling is implemented between the connection of the blocks. For detecting photoacoustic signals from deep targets with poor SNR, high sensitivity and low noise figure are highly required for the AFE. Meanwhile, considering the input signals may be very strong when the targets are

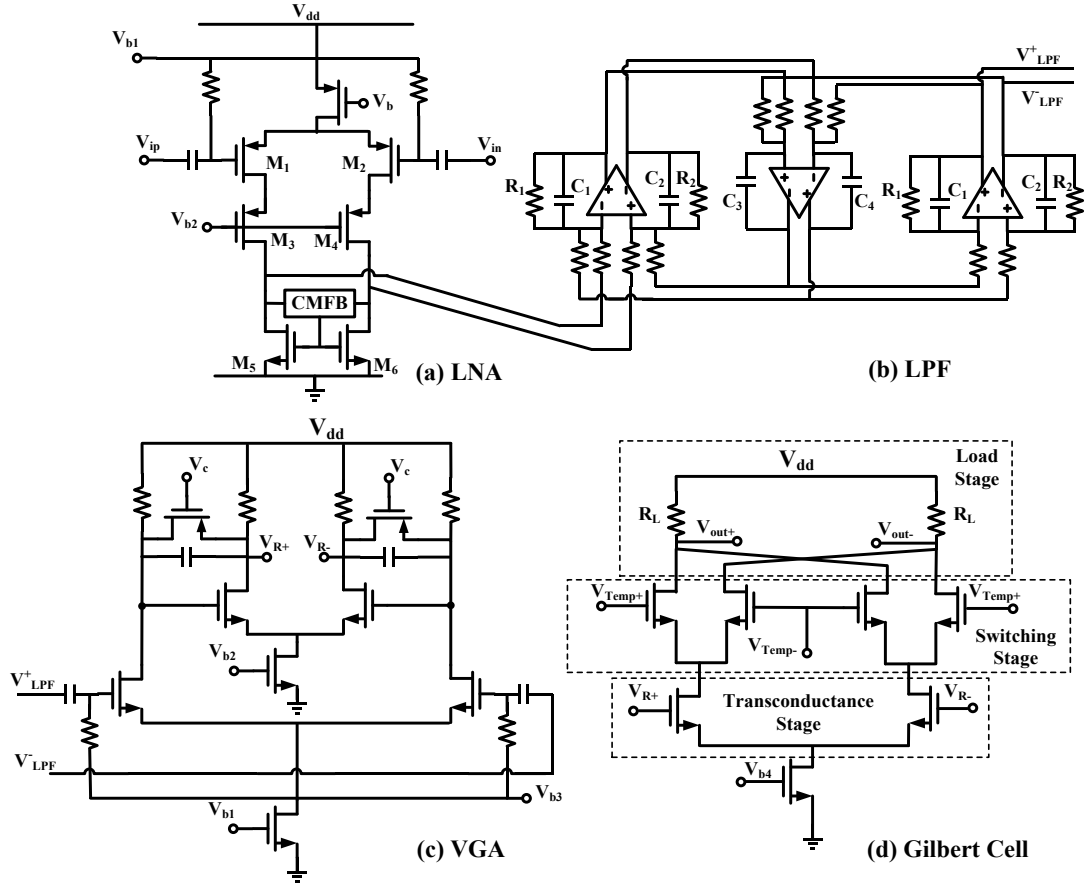


Fig. 4.7. Schematics of key analog frontend circuit blocks of the PA sensor system: (a) Low noise amplifier (LNA). (b) Low-pass filter (LPF). (c) Variable gain amplifier (VGA). (d) Gilbert cell [120].

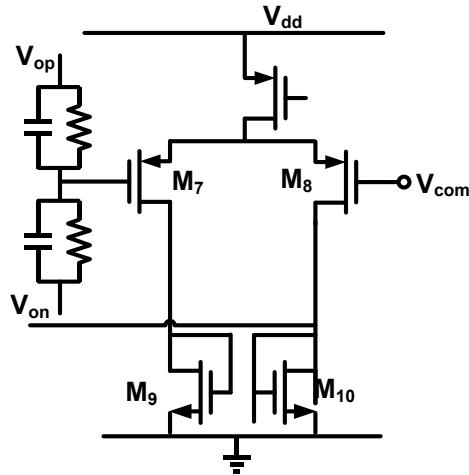


Fig. 4.8. Schematic of the CMFB in the LNA [120].

induced by a high-power laser, the AFE needs a high dynamic range to meet the requirements from different application scenarios.

Starting from the LNA, the output signal is amplified by 30 dB with 10 MHz

bandwidth. The common-mode feedback (CMFB), which is illustrated in Fig. 4.8, is used in the LNA to ensure the stable common-mode output hence the linearity of the system. The amplified signal goes through the 3rd-order Butterworth low pass filter, which can provide the best flatness in amplitude within the filter passband and moderate phase distortion compared with the other topologies (e.g., Chebyshev, Bessel, and Elliptic, etc.). Then the waveform will be boosted by the variable gain amplifier which can provide 0-30 dB gain in 10 MHz bandwidth. Active resistors are employed to achieve a dB-linear wide-range gain for the VGA. Finally, the acoustic signal is multiplied with the template waveform by the Gilbert cell on-chip. The multiplication results of the received PA signal with the template waveforms will go through the ADC to be further processed at the digital backend on FPGA to realize the target pulsed PA signal capturing and recovery.

As demonstrated in Fig. 4.7 (a), to reduce the common-mode noise from the power supply, fully differential topology is applied for the LNA. As the output resistance of piezoelectric transducers is typically low, a common-source amplifier with high input impedance is preferred. PMOS transistors implemented in N-Well are adopted as the input pair to isolate the noise from the substrate. Furthermore, as the frequency of the acoustic signal is from several Kilohertz to tens of Megahertz, the effect of flicker-noise at low frequency dominates the noise characteristic of the LNA over the thermal noise [66]. Thus, PMOS transistors are more attractive considering its characteristic of lower $1/f$ noise corner frequency compared to NMOS transistors. The noise simulation result of the LNA is shown in Fig. 4.9. The input-referred noise density is about 1.58 nV/ $\sqrt{\text{Hz}}$, which contributes 5 μV noise in 10 MHz bandwidth.

The schematic of the 3rd order LPF is illustrated in Fig. 4.7(b), which is used to reduce the out-of-band noise and unnecessary interferences in the acoustic signal. As

the center frequency of the target PA signal is in the range of 1-10 MHz for different applications, and the center frequency of the multiplication waveform of the template and the target waveform is below 20 MHz, the cut-off frequency of the LPF can be set digitally at 5 MHz, 10 MHz and 20 MHz for different application scenarios employing transducers with different bandwidth. To provide enough DC gain, a two-stage differential amplifier is used. The Miller capacitor compensation technique is adopted to secure a sufficient phase margin. The LPF suppresses the harmonics caused by the non-linearity of the LNA and ADC clock spurs via the low cut-off. The 3rd order LPF is composed of op-amp cells with a transfer function of

$$H(s) = \frac{1}{1 + 2s + 2s^2 + s^3}, \quad (4.8)$$

where the values of R_1 , R_2 , and C in Fig. 4.7(b) can be derived from the required Q-factor, center frequency f_c and gain A_G , as

$$\begin{aligned} f_c &= \frac{1}{2\pi R_1 C_1}, \\ 2C_1 &= C_3, \\ R_1 = R_2, C_1 &= C_2, C_3 = C_4. \end{aligned} \quad (4.9)$$

The AC coupling causes the lower roll-off. The roll-off of the low cut-off is 60 dB/decade corresponding to the 3rd order LPF. The cut-off frequency can be tuned from 5 MHz to 20 MHz, where the post-simulation results of the LPF have validated the design as illustrated in Fig. 4.10. The architecture of the VGA is illustrated in Fig. 4.7 (c), where the gain can be configured by adjusting the active resistors [67]. No common-mode feedback circuit is needed in this resistor-load amplifier. Moreover, the VGA does not need buffers as the VGA exhibits high input-impedance. The simulation result of the gain versus control voltage of the VGA is shown in Fig. 4.11, when the control

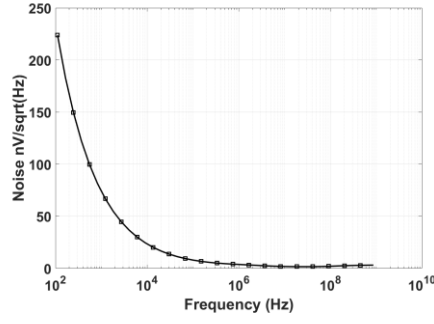


Fig. 4.9. Simulation result of noise versus frequency of the LNA [120].

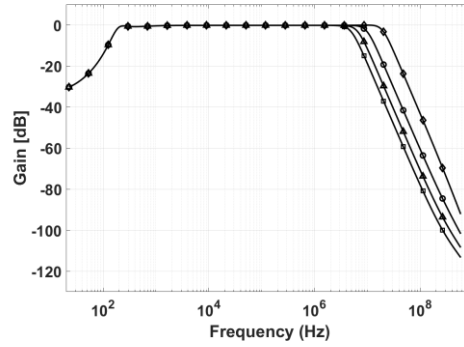


Fig. 4.10. Post-simulation result of gain versus frequency of the 3rd order LPF [120].

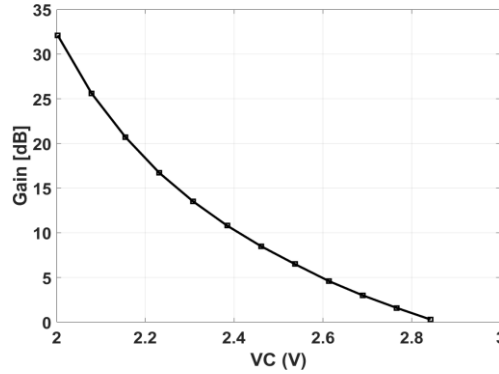


Fig. 4.11. Simulated gain versus control voltage of the VGA [120].

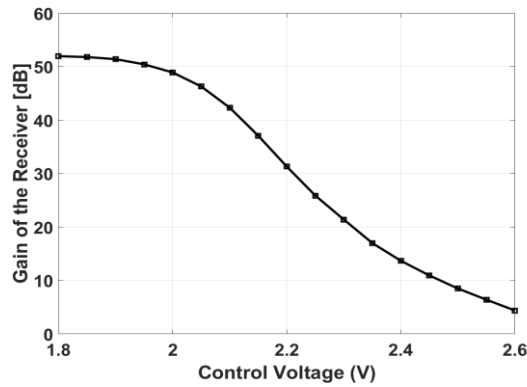


Fig. 4.12. Measured gain versus control voltage of the LNA, LPF and VGA [120].

voltage is tuned from 2 V to 3 V, the gain of the VGA is changed from 0 dB to 30 dB.

The measured overall gain versus the control voltage of the cascade of the LNA, LPF,

and VGA is illustrated in Fig. 4.12, in which about 50 dB dynamic range is attained.

The Gilbert cell is served as the analog multiplier in the PA sensor chip, which is demonstrated in Fig. 4.7 (d). It is comprised of a transconductance stage, a switching stage, and a load stage. In the Gilbert-cell topology, the nonlinearity effects are mostly dominated by the input transconductance. The linearization of the MOSFET transconductance stage requires specific considerations. In this design, the length and width of the transistors in the Gilbert cell are scaled up to reduce the mismatch effect as well as to improve the linearity. The received PA signal from LNA, LPF and VGA are properly amplified and multiplied with the template signal from the DAC by the Gilbert cell on-chip. The multiplied signals will be fed to the ADC and then further processed in FPGA to realize the coherent lock-in and precise recovery on the target PA signals, enhancing the *in vivo* sensing and imaging performance.

4.3.2 System Level Implementation of the Mixed-Signal Coherent Closed-Loop PA Sensor

The schematic of the coherent capturing loop is indicated in Fig. 4.3, where the closed-loop detection is realized with the FPGA board (5CSXFC6D6 by Altera Inc.), the AD/DA board (Terasic THDB_ADA), and the PA sensor chip. The illustration of the template waveform generation for coherent lock-in and target waveform recovery and gated integration is illustrated in Fig. 4.13. The analog circuits and the digital parts are working coordinately to enable the capturing and recovery on the weak target PA signals with enhanced SNR and specificity. The raw received PA signal induced by extreme weak laser is shown in Fig. 4.14(a) and the profile of the reconstructed target PA signal induced by extreme weak laser is shown in Fig. 4.14(b).

The ADC and the DAC in the system are realized off-chip by the THDB_ADA

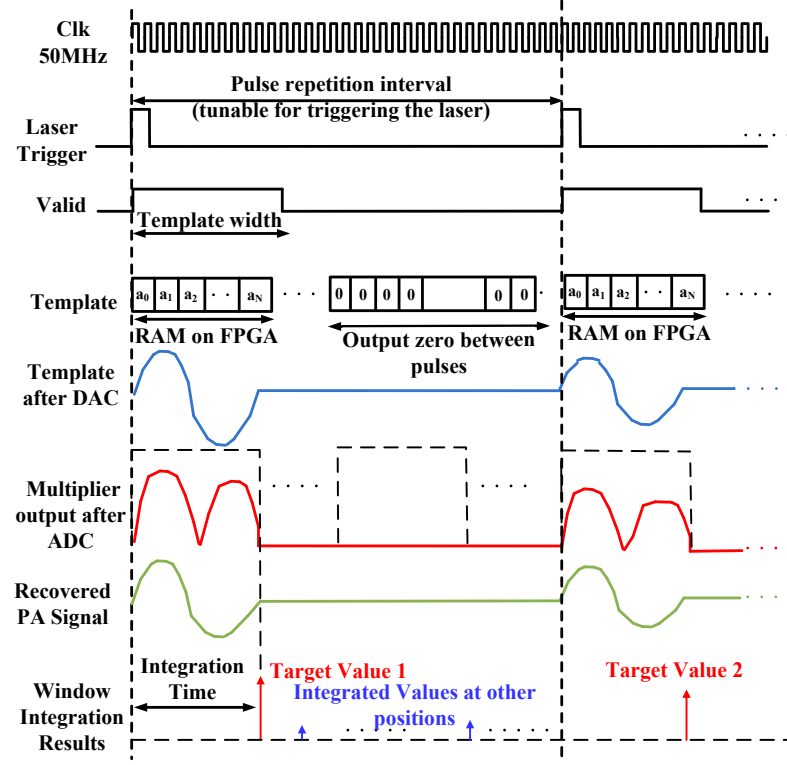


Fig. 4.13. Illustration of the template waveform generation under coherent lock-in, the reconstruction on the target signal and the gated integration [120].

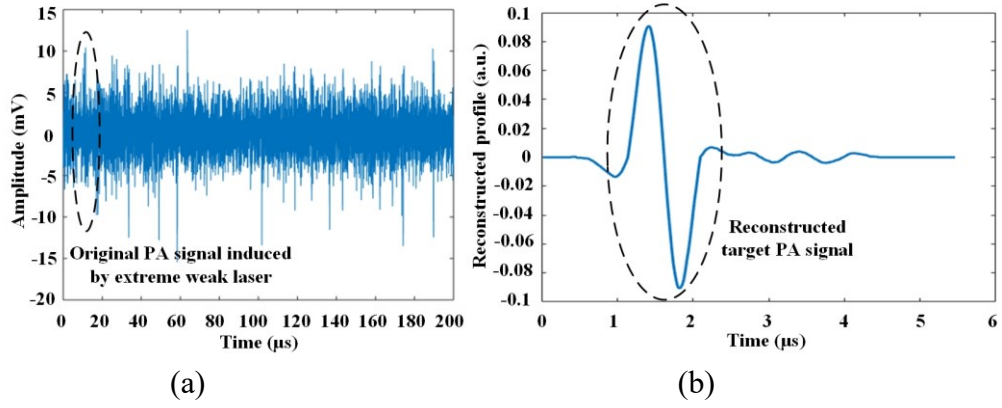


Fig. 4.14. (a) Raw received PA signal induced by extreme weak laser. (b) Reconstructed profile of the target PA signal with SNR enhancement [120].

daughter board. The 14-bit ADC board is implemented to acquire the signals from the chip-scale PA sensor and send the data to the DE-10 standard FPGA board for further digital signal processing through the HSMC interface. For the chip-scale sensor system, the ADC operates at 50 MHz, considering: 1) the sampling rate that is about twenty times of the received signal frequency is enough for temporal and signal resolution; 2)

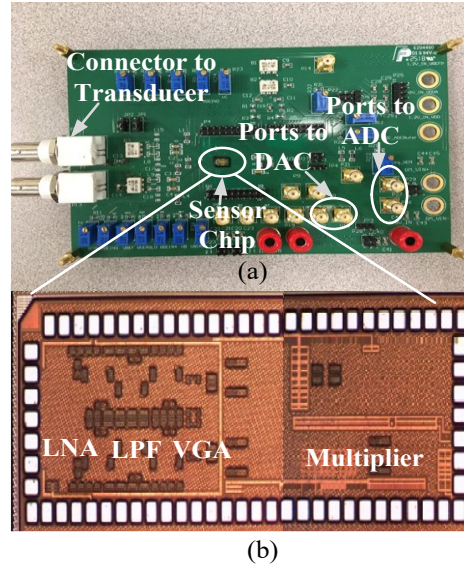


Fig. 4.15. Illustration of the PA sensor chip: (a) PCB testing board. (b) Die microphotograph [120].

the data throughput is moderate for commercial PCs. The reference clock of the ADC and DAC is synchronized to that of the template generator by using the same external crystal synchronized by the DLL of the FPGA board.

The prototype PA sensor chip is fabricated in a GlobalFoundries 65-nm CMOS process. Fig. 4.15 illustrates the printed circuit board (PCB) and the microphotograph of the chip. The connector to the transducer and the differential ports connected to DAC and ADC board are identified in the PCB board in Fig. 4.15 (a). The key analog blocks of the chip are identified in Fig. 4.15 (b). The chip was wire-bonded onto a PCB using chip-on-board technology, where FR4 material is used for the PCB substrate to ensure high-quality performance. At a 1.8-V supply, the sensor chip is within 20 mW power consumption [120]. The system can be configured to operate under 16.1 mW for PA sensing.

4.4 Experiments and Measurement Results

The setup of the chip-scale PA sensor system for the biomedical experiments is illustrated in Fig. 4.16, where the pulsed laser, the PA sensor chip, the FPGA board,

AD/DA board, and the transducer are connected. PZT transducer with 10 MHz bandwidth is used considering the detection depth and losses under various potential physiological conditions [120]. There is a layer of polydimethylsiloxane (PDMS) between the transducer and the object to realize the coupling of light and sound. For the PA-based *in vivo* imaging, considering the effects of attenuation and interferences, the imaging resolution degrades with the increase of depth and the PA signal is very weak from the in-depth target tissue.

The VGA was tuned to configure the gain of the front end to enable the system working in a suitable situation. The amplitude of the template waveform from the FPGA was also configured to enable the optimum sensing property of the whole system. The detecting target's depth was measured with the time delay according to (4.3), where the v is 1540 m/s at *in vivo* environments and is 1480 m/s at the simulated environment in the water. Four sets of experiments were carried out to validate the chip-scale PA sensor system's functions for in-depth temperature monitoring and enhanced *in vivo* imaging under low power laser excitation conditions for various kinds of biomedical applications.

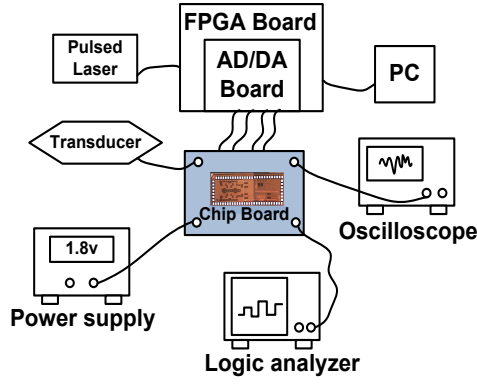
For the PA-based temperature monitoring experiments, since the intensity of the PA signal is linearly proportional to temperature, the temperature can be derived from [68]

$$p = \mu_a \Gamma(T) F, \quad (4.10)$$

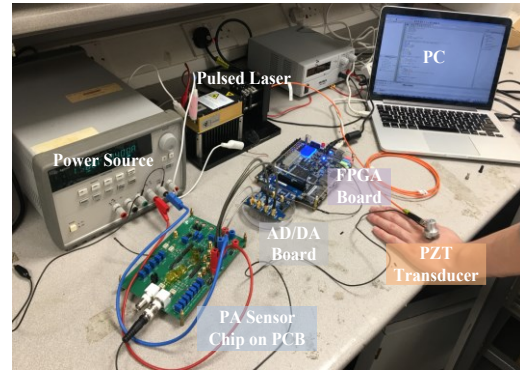
$$\Gamma(T) = \alpha + \beta T, \quad (4.11)$$

$$T = \frac{P}{P_0} \left(\frac{\alpha}{\beta} + T_0 \right) - \frac{\alpha}{\beta}. \quad (4.12)$$

Here μ_a is the absorption coefficient, F is the laser fluence, Γ is the Grueneisen parameter, P represents the measured PA signal, P_0 is the PA amplitude at a baseline, T_0 , α and β are pre-calibration coefficients for different application scenarios [68].

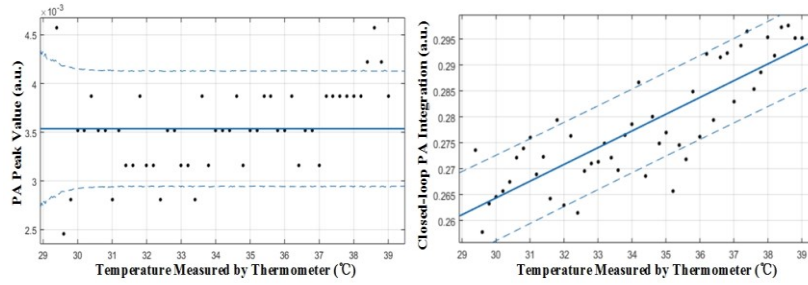


(a)



(b)

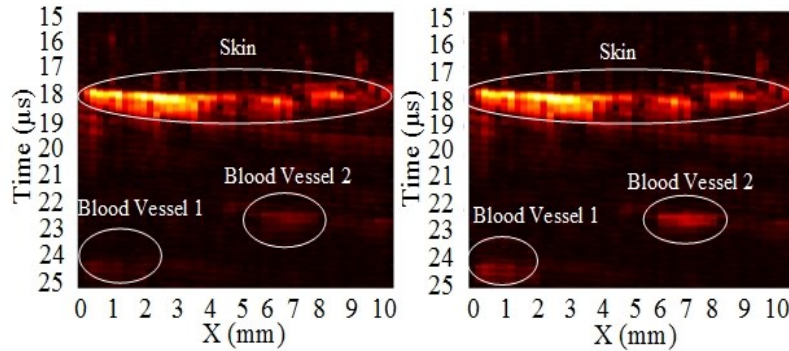
Fig. 4.16. Experimental setup of the chip-scale PA sensor system for the biomedical experiments. (a) Schematic, and (b) test environment [120].



(a)

(b)

Fig. 4.17. Temperature measurement results under the extreme weak laser illumination using the chip-scale PA sensor system. (a) Conventional open-loop measurement results. (b) Closed-loop temperature measurement results under lock-in state [120].



(a)

(b)

Fig. 4.18. *In vivo* vessel imaging under weak laser illumination. (a) Conventional open-loop imaging results. (b) Closed-loop imaging results under lock-in state [120].

Thus, the PA effect can be leveraged to non-invasively monitor temperature with a theoretically linear relationship between the PA peak amplitude and the temperature derived based on equations (4.10) to (4.12).

However, when practically monitoring the temperature with the illumination of a

low-power laser, the induced PA signal is very weak with high noise. Thus, it is hard to acquire the temperature information directly based on the peak values of the PA signal. In the temperature monitoring experiments, the phantom in the water with different temperatures was used to simulate the blood core temperature measurement environment. The first experiment was to measure the temperature using the peak value of the PA signal under the open-loop mode, and the results are illustrated in Fig. 4.17(a), where X-axis is the temperature measured by the standard thermometer while the Y-axis is the corresponding peak PA value measured from the LNA, LPF, VGA, and ADC. The fitted linearity curve is shown as the solid blue line, which is with zero slope rate, meaning that the peak PA value is masked by the noise and cannot be leveraged to detect the temperature directly. The corresponding 80% confidence interval is illustrated as the blue dashed line in Fig. 4.17(a). When the system operated under the coherent closed-loop mode, the template waveform was leveraged to realize the coherent lock-in of the target signal. Under the lock-in state, the multiplier output was integrated within the time span of one template window length. The integration result was leveraged to indicate the non-invasively measured temperature.

The integration PA sensing results under the closed-loop implementation versus the temperature measured from the standard thermometer are illustrated in Fig. 4.17(b), where the temperature trend can be obtained accurately. The corresponding 80% confidence interval is illustrated as the blue dashed line in Fig. 4.17(b). Furthermore, the root-mean square error (RMSE) of the closed-loop PA sensing will be reduced if the PA signals are measured more rounds and processed with coherent averaging.

The function of *in vivo* imaging was validated in the experiments, where a photoacoustic microscopy system was leveraged to implement the linear scan on the vessel. The *B*-mode scan was achieved with a linearized motorized stage scanner (MT3-

Table 4-1.
Technology Summary and Comparison with Prior Arts.

	JSSC 2013 [49]	T-BioCAS 2015 [64]	ISSCC 2015 [63]	JSSC 2017 [65]	This Work
Integrated Functions	Pulser+LNA+Pulse Shaping Logic	Charge Pump+Level Shifter+ Preamplifier+ Digital Control	Charge Pump+Level Shifter+ Preamplifier+ Digital Control	TIA+LPF+VGA+ADC+Digital	LNA+ LPF + VGA+ Multiplier
Laser Type	Not Used	Not Used	Not Used	Pulsed Laser	Pulsed Laser: 20Hz-2000Hz
Bandwidth	5.2MHz	0.5 MHz (Transducer)	N.A.	10 MHz	10 MHz
Center Frequency	4.5 MHz	3.2 MHz	8 MHz	5 MHz	1 MHz
Transducer Type	CMUT	PZT	PMUT	2D CMUT	PZT
Applications	Ultrasonic Imaging	Portable Healthcare Monitoring/Imaging	Body-Fat Composition Measurement	3D PA Imaging	In-vivo Imaging/ Blood Core Temperature Monitoring
Area	0.375mm ² /Ch.	2mm ²	2mm ²	0.0625mm ² /Element	0.06mm²/Ch.
Technology	0.18 um CMOS	0.18 um CMOS HV	0.18 um CMOS HV	28 nm UTBB FD-SOI	65 nm CMOS
Temperature Accuracy	n.a.	n.a.	n.a.	n.a.	~0.5° after calibration
Signal Processing Method	FFT & Velocity Estimation	2D Beamsteering Imaging	2D Beamsteering Imaging	DBF/Imaging	Mixed-Signal Coherent Lock-in
Power Consumption	14.3mW	2.6μJ/Pulse	2.6μJ/Pulse	26.7mW/Pixel	~16.1mW

Z8, Thorlabs). The scanning step is 0.2 mm with a total length of 10 mm, and the sampling rate is 50 MHz. The open-loop imaging on blood vessels was demonstrated in Fig. 4.18(a), where the two blood vessels at a depth under the skin were vague. When operating at closed-loop, the vessel's position was captured firstly; then the vessel-induced PA signal was enhanced by the template waveform and calibrated digitally. The imaging quality on target blood vessels was improved, which is illustrated in Fig. 4.18(b). The color map indicates the target vessel. The system demonstrates enormous potential for COVID-19 monitoring applications as the temperature and in-depth *in vivo* imaging can be obtained simultaneously in a non-invasive way.

The performance of the PA sensor system was summarized and compared with the

other photoacoustic or ultrasound sensor systems in Table 4-1. Considering few chip-scale photoacoustic sensors were reported; several ultrasound-based probe sensors are used for the comparison [49], [63], [64]. The laser is with about per-pulse fluence of 10 mJ/cm², which is below the ANSI limitation for laser skin exposure [69]. Notably, the dedicated design of the chip-scale photoacoustic sensor system with coherent lock-in function is well suited for blood cell temperature sensing and *in vivo* imaging applications with its capabilities on detecting extreme weak PA signals under the typical *in vivo* environments with high noise and strong interferences.

4.5 I/Q-Based Coherent Lock-in Technique for PA Signal Detection Based on Early-Late Tracking

For wearable biomedical devices, it is essential to detect target signals under high noise and strong interferences. Moreover, it is critical to realize the system with compact size and easy implementation. By leveraging the adaptive coherent lock-in technique implementing early-late tracking, high sensitivity and specificity can be achieved for detecting target signals. In-phase and quadrature PA templates are specifically designed based on the profile of the target signal and are generated by the FPGA board and the DAC boards. The received signal is correlated with the templates to capture, track, and recover the target PA signal with a high fidelity [128].

To detect the PA signals under smaller than 0 dB SNR scenario, template waveforms need to be specifically designed and leveraged. The template-based method has been applied in photoacoustic sensing and radar-based vital sign monitoring [47], [48]. Furthermore, leveraging the quadrature properties of the in-phase/quadrature (I/Q) templates will further enhance the accuracy of discerning weak signals in the spatial and temporal domain. Based on the quadrature mixed-signal coherent lock-in technique, the PA effect, and the fast-growing CMOS technology, a chip-based sensor system called

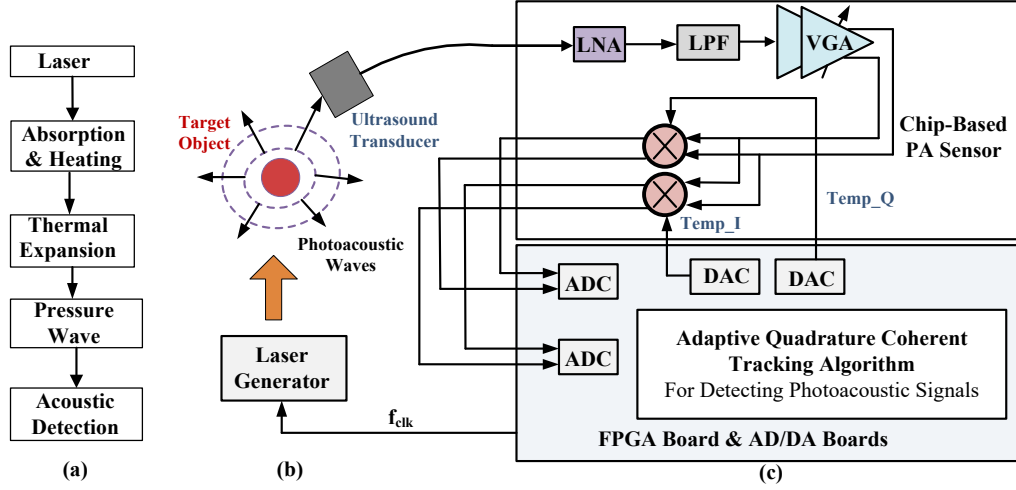
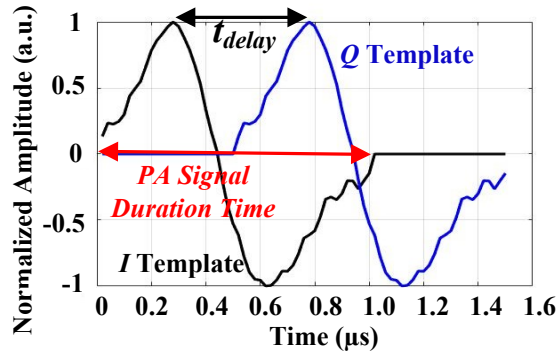


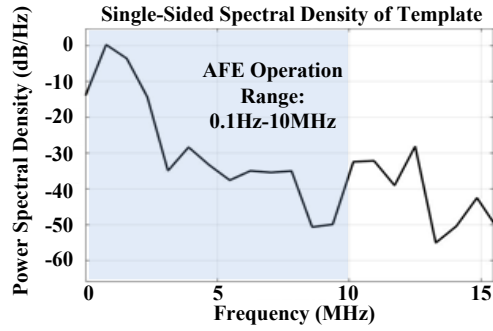
Fig. 4.19. Illustration of the proposed QuACL system: (a) Photoacoustic effect. (b) Pulsed laser for inducing the PA signal at the object. (c) System diagram.

the QuACL is proposed, which is illustrated in Fig. 4.19, demonstrating its capability on monitoring signals at scenarios with high noise and strong interferences based on adaptive quadrature coherent sensing leveraging early-late tracking.

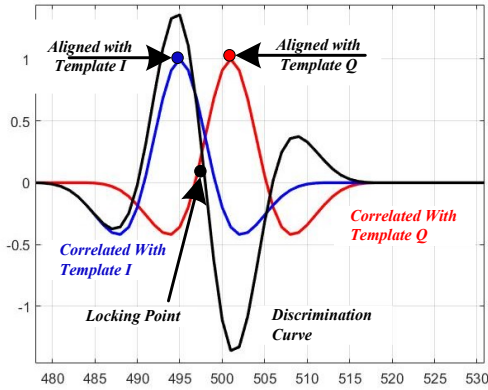
To obtain the template profile, a high-power pulsed laser is used to induce the PA signal from the target object. Then, a coherent summation of a tunable number of pulses is implemented to obtain the template profile. Considering that the noise and interferences are un-correlated to the template signal, the correlation result with noise and interferences are expected to be zero while the correlation result with the target signal component remains, thus the target signal is extracted. In-phase templates and quadrature templates are utilized to enable the coherent lock-in and early-late tracking on the target PA signal. The in-phase and quadrature template waveforms are generated by the FPGA and the DAC. The process of capturing and recovery on the target PA signals is achieved by the quadrature mixed-signal closed-loop processing. The I and Q templates are illustrated in Fig. 4.20(a). The spectrum of the PA template is shown in Fig. 4.20(b), where the signal is within 10MHz range. The process is controlled by the FPGA based on the discrimination curve. The process is completed by three phases.



(a)



(b)



(c)

Fig. 4.20. (a) Illustration of the *I* and *Q* templates. (b) Spectrum of the PA template. (c) Illustration of early-late tracking loop with discrimination curve indicated.

First, the target PA signal is captured with initial timing synchronization to the template signal. Second, the *I/Q* templates, which are with a delay of half a target PA pulse width, are generated adaptively to track the target signal in real-time early-late adjustment determined by integration and subtraction of the received *I*-channel and *Q*-channel signals. Based on the *I/Q* templates, the early-late tracking on the target PA signal can be implemented, which is illustrated in Fig. 4.20(c). Third, the acquired signal under the

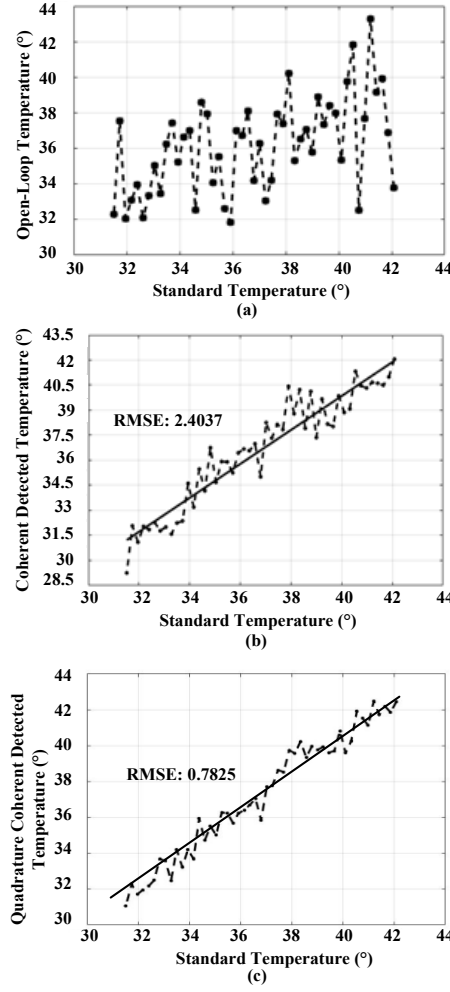


Fig. 4.21. Measured temperature under weak laser irradiating phantom in hot water. (a) Measured result with direct amplitude-temperature mapping. (b) Measured results using one-channel coherent PA detection. (c) Measured results using mixed-signal quadrature coherent PA detection.

coherent lock-in state is digitized by the ADC and is processed by the FPGA to recover the target waveform, obtaining the corresponding physical of physiological information of the object and for the imaging applications.

The ADC operates at 50 MHz with the 14-bit ENOB to enable the required sampling resolution. An iterative LUT on FPGA is used to generate the template I/Q waveforms. The pulse repetition frequency (PRF) of the pulsed laser is determined by the configurable clock signal f_{clk} from the FPGA, depending on the application scenario. By multiplying the template waveform and the received signal through Gilbert cell, the acquired signals $R_I(t)$ at the I channel and the $R_Q(t)$ at the Q channel are expressed as

$$R_I(t) = p(t) * Temp_I(t), \quad (4.13)$$

$$R_Q(t) = p(t) * Temp_Q(t), \quad (4.14)$$

$$Discrimination(t) = R_I(t) - R_Q(t), \quad (4.15)$$

where $Temp_I(t)$ is the in-phase template waveform, $Temp_Q(t)$ is the quadrature template waveform, which is half a period lagged with the in-phase template in the time domain. The target PA signal is discerned, tracked, and recovered based on the $R_I(t)$ and $R_Q(t)$ at the digital side by the FPGA. Based on the Matlab simulation results, the target PA signals can be discerned and recovered robustly under -10 dB SNR and can be tracked and reconstructed at -15 dB SNR. The open-loop PA sensing on temperature is illustrated in Fig. 4.21(a), where the temperature cannot be obtained. In Fig. 4.21(b), the temperature was measured by the method in [120]. The QuACL system was verified by temperature measurements with low-power laser excitation, where the results are shown in Fig. 4.21(c). The X-axis represents the reference temperature measured by thermometer, while the Y-axis is recovered PA signal amplitude after digital processing.

4.6 4-channel Coherent PA SoC Design

In Section 4.5, the chip-based mixed-signal coherent lock-in PA sensor for accurate wake waveform sensing and imaging is presented. The main limitation of the prototype is that the integration level of blocks is still relatively low, where the coherent signal capturing loop needs to be realized with the help of off-chip DAC, ADC, and the FPGA for signal processing. To implement the PA system into a more compact level toward realizing portable *in vivo* sensing and imaging, a 4-channel photoacoustic sensor SoC with the capability of early-late tracking on target PA signals is implemented, where DACs, ADCs, and the digital processing module are integrated on-chip. For the first time, the PA SoC realized the adaptive tracking and precise reconstruction on the in-

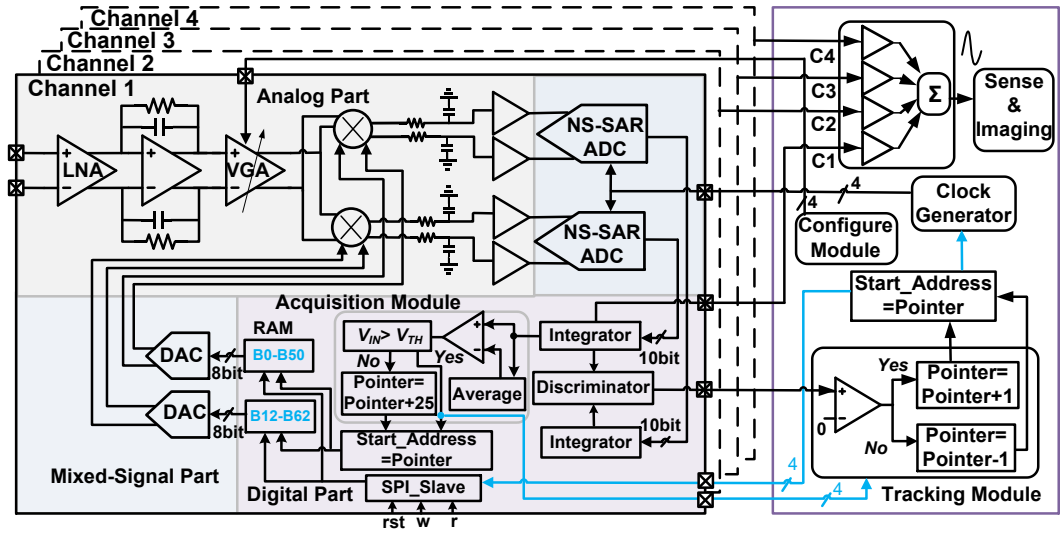


Fig. 4.22. Block diagram of the 4-channel I/Q based coherent PA sensor SoC with early-late tracking function.

depth weak PA signal based on the mixed-signal early-late tracking loop, enabling the PA imaging under in-depth *in vivo* scenario with high noise and strong interferences.

The system architecture of the 4-channel PA SoC sensor system is demonstrated in Fig. 4.22, where the early-late tracking is realized by the analog front end and the digital module on-chip. The laser is triggered by the clock controlled by an FPGA. Four PZT transducers are used to acquire the PA signals; thus, in-depth PA signals, masked by strong interferences and high noise, can be detected. The block diagram of the PA SoC is demonstrated in Fig 4.22, where the analog part, the digital processing module, as well as the AD/DA converters, are illustrated. Two 8-bit current-steering DAC and two 10-bit noise-shaping SAR ADC are leveraged to enable the early-late tracking loop based on the coherent I/Q templates in each channel. The early-late tracking process is realized by the signal acquisition module and tracking module, which are indicated in Fig. 4.20(c). The locked target 4-channel PA signals are summed coherently; thus, the SNR is enhanced, and the interferences are suppressed. The system's circuits include the analog part contained by the LNA, VGA, mixer, and buffer, the digital processing

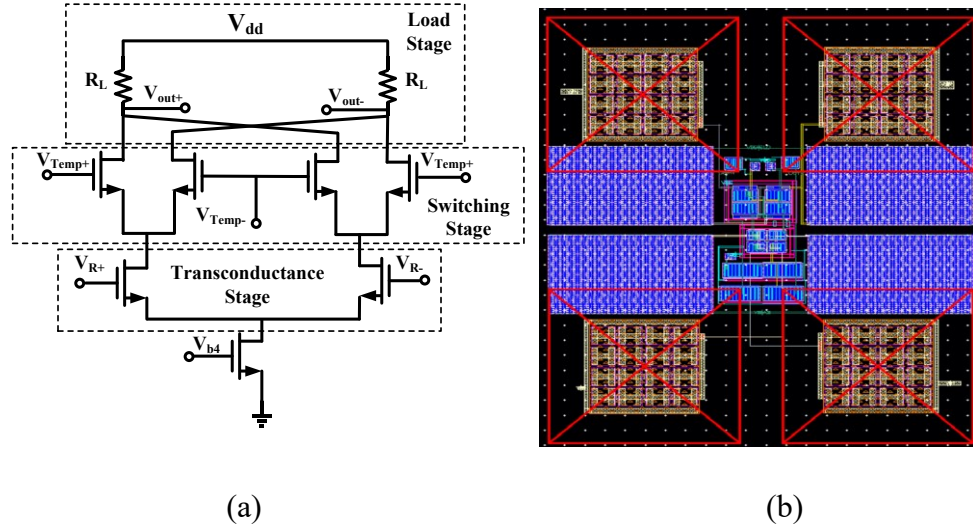


Fig. 4.23. (a) Circuit diagram of the Gilbert cell. (b) Layout of the Gilbert cell. module on-chip synthesized based on Verilog, and the AD/DA converters. The essential critical blocks are illustrated.

4.6.1 Gilbert Cell Implementation

The Gilbert cells are used in the PA SoC to realize the analog multiplication of the template signal with the received signal from the transducer. The circuit diagram of the differential active Gilbert cell is illustrated in Fig. 4.23(a). A buffer is following the output of the Gilbert cell to boost the driving capability. The layout of the Gilbert cell is illustrated in Fig. 4.23(b).

4.6.2 DAC

An 8-bit current steering DAC is used to generate the template waveform, where the system architecture is illustrated in Fig. 4.24. Two 4-bit binary to thermometer converters are used to control the current cells; the binary to thermometer converter is implemented with standard digital cells from TSMC. The low-level bit 0 to bit 3 of the DAC are implemented by controlling one current cell, while the high-level bit 4 to bit 7 are implemented by controlling 16 current cells; thus, the values of the summation of

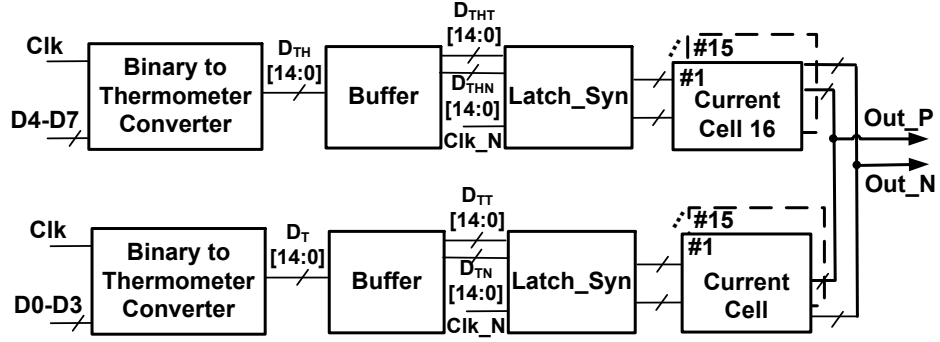


Fig. 4.24. System architecture of the 8-bit current-steering DAC.

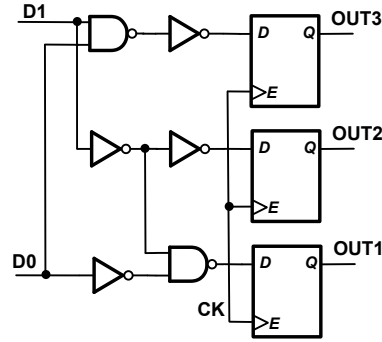


Fig. 4.25. Block diagram of the Decode_1st module.

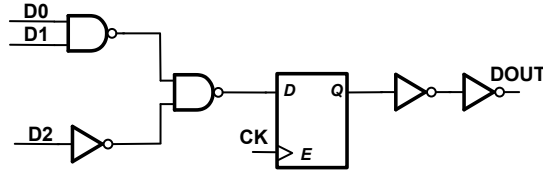


Fig. 4.26. Block diagram of the Decode_2nd module.

the current sources is in the range of 0 to $(15 \cdot 16 + 15)I_{current} = 255I_{current}$; therefore, the 8-bit resolution current steering DAC can be realized.

The clock for the Decode_1st module is illustrated as CKB and the clock for the Decode_2nd module is illustrated as CKN, which is the inverse of CKB. The block diagram of the Decode_1st module is illustrated in Fig. 4.25, where the inputs D0 and D1 are processed by the inverters, NAND gates, and output from the D flip-flops. The block diagram of the Decode_2nd module is illustrated in Fig. 4.26, where the inputs D0 and D1 are processed by NAND, input D2 is processed by inverter. Then the NAND output and the inverter output are processed by a NAND. The output of the 2nd NAND

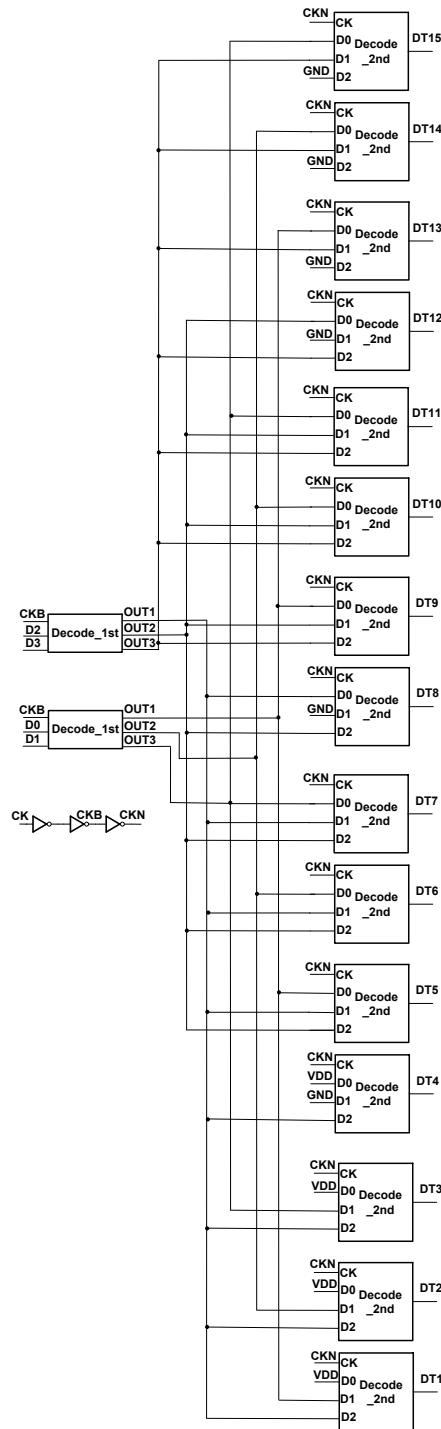


Fig. 4.27. Schematic of the 4-bit binary to thermometer converter.

then undergoes the D flip-flop, and two inverters and the final output DOUT is the and output from the inverter. The outputs of the binary to thermometer converters will go through the buffers implemented by the inverters and be transformed into the differential form for further processing. The schematic of the 4-bit thermometer to binary converter is illustrated in Fig. 4.27, where the 4-bit binary inputs D0, D1, D2, and D3 are converted

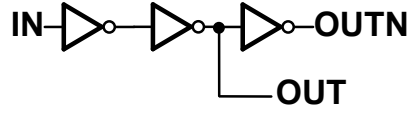


Fig. 4.28. Circuit diagram of the buffer.

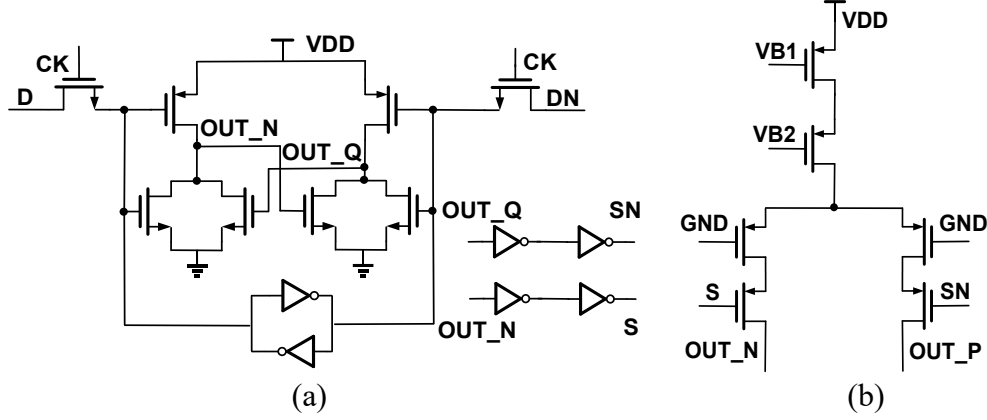


Fig. 4.29. (a) Circuit diagram of the latch synchronizer. (b) Circuit diagram of the current cell.

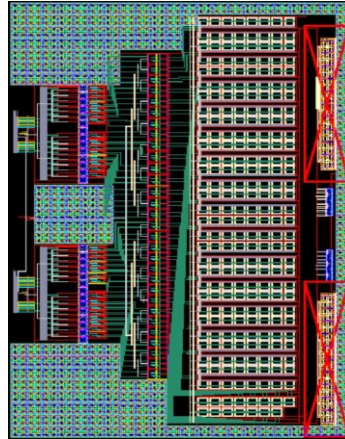


Fig. 4.30. Layout of the 8-bit current steering DAC.

to thermometer outputs DT1 to DT15 through the Decode_1st module and the Decode_2nd module. The buffer is implemented with 3 inverters from standard digital circuit library in TSMC process, which is demonstrated in Fig. 4.28. The circuit diagram of the latch synchronizer is illustrated in Fig. 4.29(a), where the buffers' differential outputs represented as D and DN are going through the latch synchronizer controlled by clock signal CK. The outputs of the latch synchronizer are used to control the current cells to complete the DAC function. The DAC is designed to work at 50 MHz clock frequency. The circuit diagram of the current cell is demonstrated in Fig. 4.29(b), where

the current cell's value can be configured by the biasing voltages VB1 and VB2. The current cell's output is either OUT_N or OUT_P, which is determined by the control signals of S and SN, which is determined by the control signals of S and SN. The layout of the whole DAC is demonstrated in Fig. 4.30. The I/Q correlation is realized based on analog multiplication by Gilbert cell and digital summation implemented on-chip. The I/Q templates are controlled based on the discrimination curve determined by the subtraction of I/Q -channel correlation results, which would enable the adaptive early-late tracking on target PA signal illustrated in Fig. 4.20 and equations (4.13) to (4.15).

4.7 Summary

In this chapter, the design of novel CMOS chip-scale PA sensor systems for *in vivo* imaging and blood core temperature monitoring is presented. The details of the prototype sensor system and the experiments have been presented. The strong interferences and noises from tissues are suppressed by the 3rd order active-RC LPF. The AFE attains a tunable 0-50 dB gain where the LPF can provide a passband bandwidth from 0.1 MHz to 10 MHz. Directly bonding to a PCB, the photoacoustic sensor can achieve 50 μ V sensitivity, enabling continuous, portable blood core temperature monitoring and imaging with enhanced precision. Additionally, the quadrature coherent lock-in sensor chip leveraging early-late tracking has demonstrated its potential to be widely adopted by PA/ultrasound system for wearable healthcare monitoring and disease diagnosis. Moreover, a 4-channel PA SoC implementing early-late tracking and adaptive beamforming is presented with analog front end, ADC, DAC, and digital processing module integrated on-chip. The designs demonstrate the mixed-signal PA sensor SoC's potential for versatile health sensing in current COVID-19 pandemic and future intelligent IoE era.

Chapter 5

Conclusions and Recommendations for Future Work

In this chapter, the thesis's conclusions on coherent chip-scale PA and radar sensor circuits and systems design for pervasive healthcare applications are presented. Moreover, the recommendations for future work are discussed.

5.1 Conclusions

The thesis presents the research on the CMOS-integrated radar sensor for noncontact multimodal vital signs monitoring and falling detection, as well as the chip-based photoacoustic sensor for non-invasive temperature monitoring and *in vivo* imaging, exploring the chip-based sensor systems leveraging multi-physical mechanism to enable pervasive healthcare monitoring and potential disease diagnosis in current global COVID-19 pandemic and for future intelligent IoE era.

A CMOS-integrated phased-array radar sensor prototype fabricated in the GlobalFoundries 65-nm CMOS process for wide FoV multimodal vital sign monitoring and falling detection is presented. The co-design of integrated circuit blocks and efficient signal processing algorithms utilizing the interferometric phase is implemented to enable the accuracy, low power consumption, and reliability of the radar sensor for detecting tiny movements caused by heartbeat and respiration. Vernier-based DLL's design considerations, which is an essential building block for the phased-array radar sensor, are discussed in Section 3.5, where the DLL measurement results are presented. Besides the radar sensors implemented for respiration, heartbeat, and falling monitoring, to further monitor the in-depth blood core temperature and achieve *in vivo* imaging for

potential disease diagnosis, a high-precision CMOS-integrated mixed-signal coherent lock-in photoacoustic sensor prototype realized in GlobalFoundries 65-nm CMOS process is designed to realize the compact-size sensor for potential disease diagnosis in a portable way. Furthermore, a four-channel photoacoustic SoC was fabricated in TSMC 65-nm CMOS process, including the AFE, ADC, DAC, and the digital processing module implementing coherent lock-in and accurate beamforming for precisely detecting target photoacoustic signals with enhanced SNR, improved sensitivity and specificity for *in vivo* subject monitoring as well as enhanced imaging.

To conclude, through the coordinated optimizations on the mixed-signal integrated circuits, energy-efficient sensor signal processing algorithms, and the usage on multi-physical mechanisms including the sensing based on EM, acoustics, and light, the CMOS-integrated mixed-signal coherent radar sensors and chip-based photoacoustic sensor prototypes have verified their capabilities on accurate multimodal vital signs monitoring, falling detection, temperature monitoring, and *in vivo* imaging. The thesis explores the route toward efficient versatile sensing for ubiquitous health status monitoring in the current COVID-19 pandemic and furthermore, personalized potential disease diagnosis for the future intelligent Internet of Everything (IoE) era.

5.2 Recommendations for Future Work

The thesis mainly presents the published work of the chip-based photoacoustic sensors and CMOS-integrated radar sensors for healthcare applications, targeting at sensing and imaging. Besides sensing and imaging, highly energy-efficient ultra-low-power (ULP) communication systems are essential to realize the fully-connected edge bio-devices for ubiquitous and connected healthcare monitoring applications.

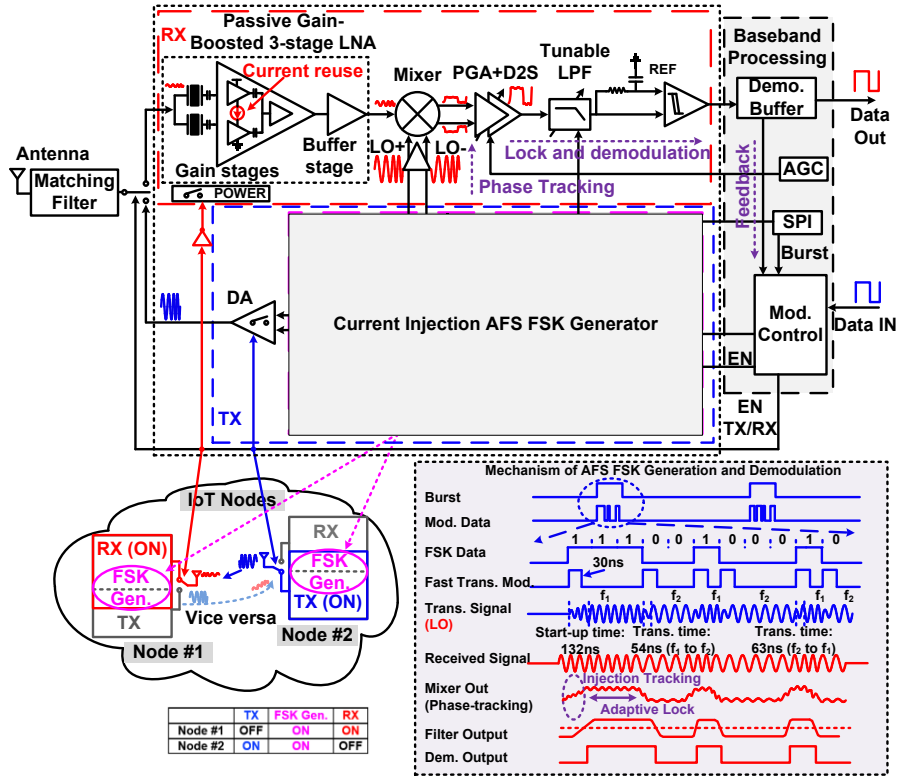


Fig. 5.1. The schematic of the AFS FSK TRX.

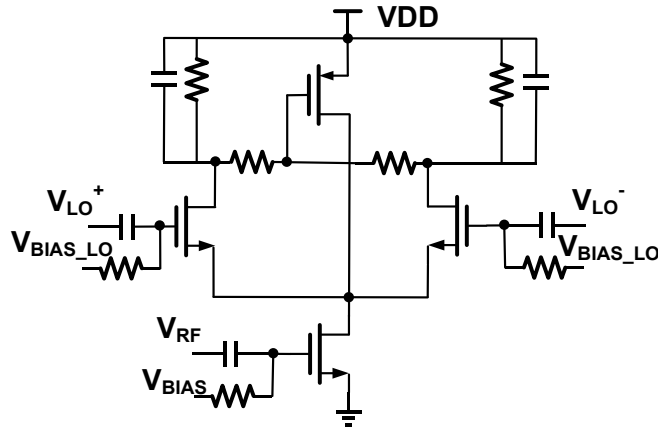


Fig. 5.2. Schematic of the current bleeding Gilbert cell for AFS FSK TRX.

5.2.1 FSK Transceiver for ULP Communications

We have developed the MEMS-based ULP FSK transceiver techniques, where several FSK communication chips have been taped out, which include a MEMS-based FSK receiver and a MEMS-based subsampling FSK receiver working at industrial,

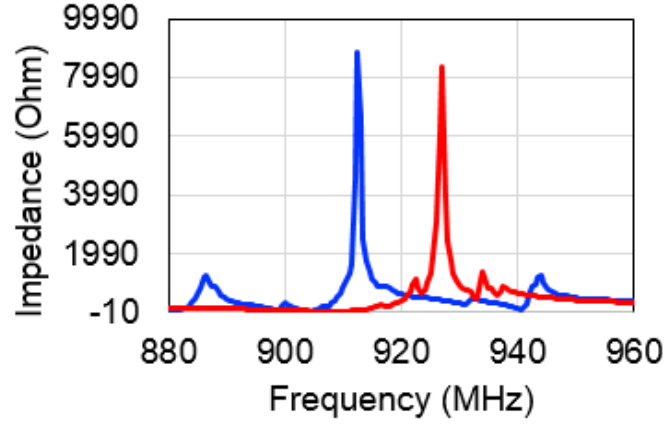


Fig. 5.3. Measured parallel impedance R_p of two different devices at the parallel resonant frequencies of 911.9 MHz and 923.1 MHz [131].

scientific and medical (ISM) band [124].

The schematic of the AFS FSK receiver is demonstrated in Fig. 5.1. To enable the low power consumption with high conversion gain, a current-bleeding RF input Gilbert cell with single-ended RF input and differential LO input is used in the ULP FSK receiver, which is illustrated in Fig. 5.2. There are two resonant frequencies in the MEMS resonators, namely series resonant frequency f_s where the impedance of resonator R_s is lowest and parallel resonant frequency f_p where the resonator has the highest impedance value of R_p . For the MEMS-based cross-coupled oscillator, the oscillation will happen at f_p . To start up oscillation with low power, larger R_p is required. Fabricated with different device dimensions, the measured R_p of two MEMS resonators are larger than 7000 at 911.5 MHz and 926.2 MHz, which are shown in Fig. 5.3 [131].

5.2.2 CMOS-Integrated UWB Radar Sensor for Accurate Multimodal Vital Signs Monitoring

To further improve the resolution and power consumption of CMOS-integrated biomedical radar sensors, a proposed chirped UWB chip-scale radar for future work is

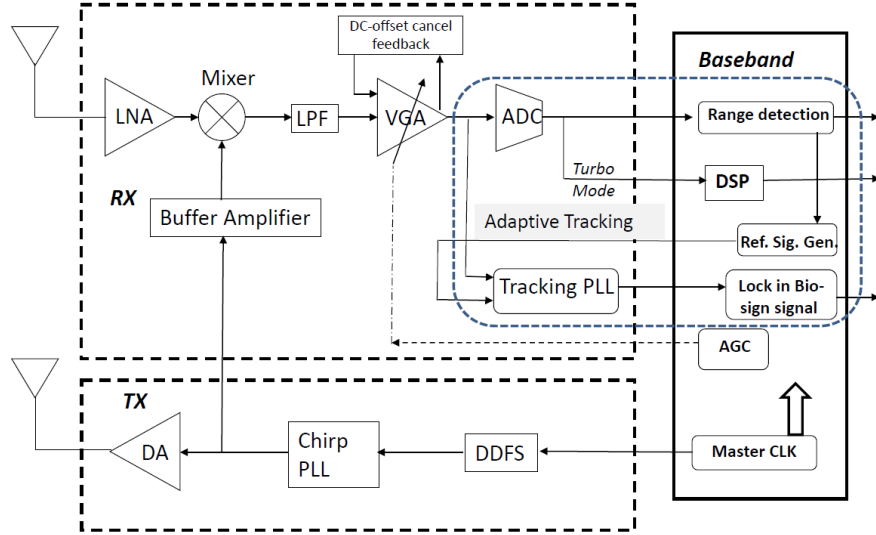


Fig. 5.4. Proposed coherent chirped UWB CMOS-integrated radar sensor with turbo mode closed-loop tracking.

illustrated in Fig. 5.4, where the advantages of UWB and FMCW techniques are leveraged together. The closed-loop chirp generation can enable high chirp linearity and broader bandwidth, which will ensure a much better range resolution and improved pulse phase coherence. The tracking PLL and turbo-mode DSP module will be developed to ensure reliable and accurate heartbeat discerning and tracking with low phase noise in the closed loop. The power consumption of the proposed radar sensor is scalable to enable reliable performance under different application requirements. Moreover, the UWB masked Chirp Radar (UWB-CR) technique is compatible with the Federal Communications Commission (FCC) frequency mask, where the ranging and bio-sign detection can be achieved concurrently in real-time. The turbo mode supported by adaptive tracking loop is leveraged to enable enhanced data processing and effective feature extraction in an efficient mixed-signal mode.

5.2.3 Efficient Sensor Signal Processing Techniques

The robust and high-resolution vital signs monitoring algorithm can be further

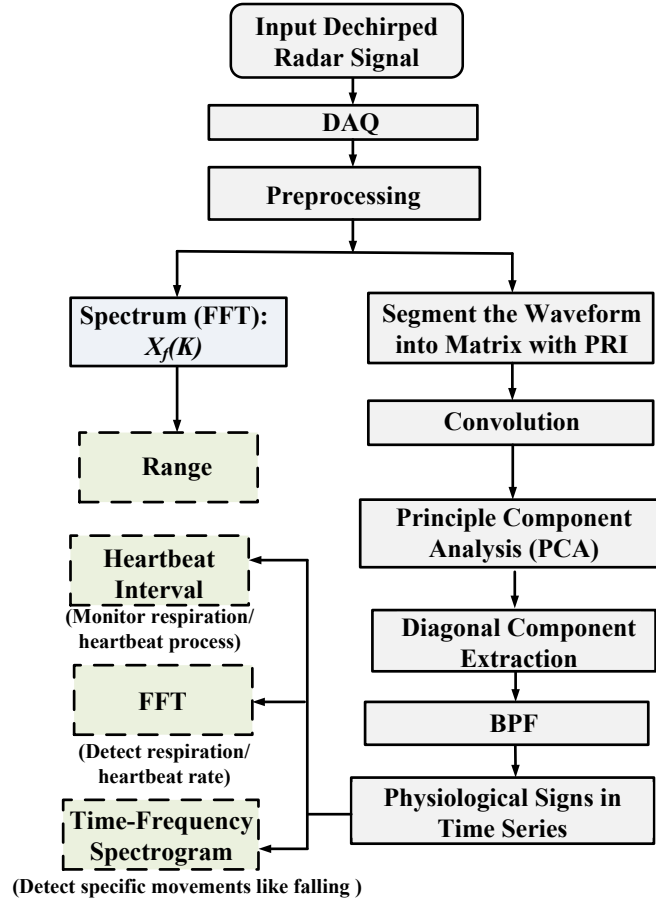


Fig. 5.5. Proposed robust and accurate algorithm for multimodal vital signs monitoring based on radar sensor.

explored to improve the detection sensitivity and accuracy of the radar system [125]. As illustrated in Fig. 5.5, the algorithm will utilize FFT for range determination, the interferometry processing for tiny movements detection, and the sPCA algorithm for accurate biomedical features extraction; therefore, the precise healthcare monitoring can be achieved. Moreover, the proposed algorithm can be easily implemented on-chip as a digital processing module. To further improve the recognition accuracy on specific movements like falling and different gestures, convolutional neural networks (CNN), recurrent neural networks (RNN), and reinforcement learning can be explored to improve the radar sensor system's performance for intelligent precise recognition on the target's features, enabling near-sensor processing in an easily deployable way.

To further enhance the PA sensor SoC system's performance, artificial intelligent

(AI) techniques can be implemented on-chip. AI models with local learning such as biologically-plausible spiking neuron networks and restricted Boltzmann machine models can be competitive candidates for radar bio-sensing applications, as the local learning is more energy-efficient than the CNN deep learning based on the backpropagation method with massive data movement across the network [127].

With a computation-in-memory architecture, the chip-scale sensor system's capabilities on cognitive sensing, imaging, and in-sensor signal processing have the potential to be further enhanced, paving the way for the next-generation chip-scale multimodal edge sensing, complementary healthcare monitoring, and personalized disease diagnosis with improved sensitivity and increased specificity in the IoE era.

Author's Publications

- [1] **Zhongyuan Fang**, Chuanshi Yang, Haoran Jin, Liheng Lou, Kai Tang, Xiaoyan Tang, Ting Guo, Wensong Wang, and Yuanjin Zheng, A Digital-Enhanced Chip-Scale Photoacoustic Sensor System for Blood Core Temperature Monitoring and *In Vivo* Imaging, **-IEEE Transactions on Biomedical Circuits and Systems, 2019.**
- [2] **Zhongyuan Fang** *et al.*, A Mixed-Signal Chip-Based Configurable Coherent Photoacoustic-Radar Sensing Platform for *In Vivo* Temperature Monitoring and Vital Signs Detection, **-IEEE Transactions on Biomedical Circuits and Systems, 2021.**
- [3] **Zhongyuan Fang**, Liheng Lou, Kai Tang, Wensong Wang, Yisheng Wang, Ting Guo, Chuanshi Yang, and Yuanjin Zheng, Wide Field-of-View Locating and Multi-Modal Vital Sign Monitoring Based on X-Band CMOS-Integrated Phased-Array Radar Sensor, **-IEEE Transactions on Microwave Theory and Techniques, 2020.**
- [4] Liheng Lou, Kai Tang, **Zhongyuan Fang**, Yisheng Wang, Bo Chen, Ting Guo, Xiaohua Feng, Siyu Liu, Wensong Wang, and Yuanjin Zheng, An Early Fusion Complementary RADAR-LiDAR TRX in 65nm CMOS Supporting Gear-Shifting Sub-cm Resolution for Smart Sensing and Imaging, **-International Solid-State Circuits Conference (ISSCC), 2021.** (First student author)
- [5] **Zhongyuan Fang**, and Liheng Lou, and Chuanshi Yang, and Kai Tang, and Yuanjin Zheng, A Ku-band FMCW Radar on Chip for Wireless Micro Physiological Signal Monitoring by Interferometry Phase Analysis, **-IEEE International Symposium on Circuits and Systems (ISCAS), 2018.**
- [6] **Zhongyuan Fang**, Chuanshi Yang, Kai Tang, Liheng Lou, Wensong Wang, Haoran Jin, Xiaoyan Tang, and Yuanjin Zheng, A Quadrature Adaptive Coherent Lock-in

- Chip-Based Sensor for Accurate Photoacoustic Detection, **-IEEE International Symposium on Circuits and Systems (ISCAS), 2020.**
- [7] **Zhongyuan Fang,** Liheng Lou, et al., A Digital-Enabled Interferometric Radar Sensor for Physiological Sign Monitoring, **-IEEE International System-on-Chip Conference (SOCC), 2019 (invited).**
- [8] **Zhongyuan Fang,** et al., A CMOS-Integrated Radar-Assisted Cognitive Sensing Platform for Seamless Human-Robot Interactions, **-IEEE International Symposium on Circuits and Systems (ISCAS), 2021.**
- [9] Kai Tang, Liheng Lou, Bo Chen, Ting Guo, Yisheng Wang, **Zhongyuan Fang,** Chuanshi Yang, Wensong Wang, and Yuanjin Zheng, A 4TX/4RX Pulsed Chirping Phased-Array Radar Transceiver in 65nm CMOS for X-Band Synthetic Aperture Radar Application, **-IEEE Journal of Solid-State Circuits (JSSC), 2020.**
- [10] Liheng Lou, Kai Tang, Bo Chen, Ting Guo, Yisheng Wang, Wensong Wang, **Zhongyuan Fang,** Zhe Liu, Yuanjin Zheng, A 253mW/Channel 4TX/4RX Pulsed Chirping Phased- Array Radar TRX in 65nm CMOS for X-Band Synthetic-Aperture Radar Imaging, **-International Solid-State Circuits Conference (ISSCC), 2018.**
- [11] Chuanshi Yang, **Zhongyuan Fang*,** Xiaoyan Tang, Liheng Lou, Kai Tang, Yuanjin Zheng, “A Photoacoustic Receiver System-on-Chip with a Novel Correlation Detection Technique Based on Early-and-Late Tracking,” **-IEEE International Symposium on Circuits and Systems (ISCAS), 2020.**
- [12] Lei Qiu, Supeng Liu, **Zhongyuan Fang,** Yuanjin Zheng, An Adaptive Beamforming Technique for UWB Impulse Transceiver, **-IEEE Transactions on Circuits and Systems II, 2019.**
- [13] Longjie Zhong, Xinquan Lai, Xinqin Liao, Chuanshi Yang, **Zhongyuan Fang,** and Yuanjin Zheng, Capacitive Touch Panel With Low Sensitivity to Water Drop

- Employing Mutual-Coupling Electrical Field Shaping Technique, **-IEEE Transactions on Circuits and Systems I**, 2019.
- [14] Longjie Zhong, Xinquan Lai, Xinqin Liao, **Zhongyuan Fang**, and Yuanjin Zheng, Precision Improvement of Power-Efficient Capacitive Sensor Readout Circuit Using Multi-Nested Clocks, **-IEEE Transactions on Circuits and Systems I**, 2020.
- [15] Wensong Wang, Zhenyu Zhao, Quqin Sun, **Zhongyuan Fang**, et. al., Compact Quad-Element Vertically-Polarized High-Isolation Wideband MIMO Antenna for Vehicular Base Station, **-IEEE Transactions on Vehicular Technology**, 2020.
- [16] Chuanshi Yang, Huaxi Sun, Lei Qiu, **Zhongyuan Fang**, and Yuanjin Zheng, A Broadband Resonant Noise Matching Technique for Piezoelectric Ultrasound Transducers, **-IEEE Sensors Journal**, 2020.
- [17] Liheng Lou, Kai Tang, **Zhongyuan Fang**, Bo Chen, Ting Guo, Zhe Liu and Yuanjin Zheng, A DDS-Driven ADPLL Chirp Synthesizer with Ramp-Interpolating Linearization for FMCW Radar Application in 65nm CMOS, **-IEEE International Symposium on Circuits and Systems (ISCAS)**, 2018.
- [18] Wensong Wang, Zhenyu Zhao, **Zhongyuan Fang**, et.al., Compact Broadband Four-Port MIMO Antenna for 5G and IoT Applications, **-Asia-Pacific Microwave Conference (APMC)**, 2019.
- [19] Zhe Liu, Liheng Lou, **Zhongyuan Fang**, Kai Tang, Ting Guo, and Yuanjin Zheng, A DLL-based Configurable Multi-Phase Clock Generator for True-Time-Delay Wideband FMCW Phased-Array in 40nm CMOS, **-IEEE International Symposium on Circuits and Systems (ISCAS)**, 2018.
- [20] Ting Guo, Kai Tang, Liheng Lou, **Zhongyuan Fang**, et. al., A Two-Stage Push-pull Power Amplifier with Electro-Thermal Effects Study in 130 nm SOI CMOS for IEEE 802.11ac Applications, **-IEEE International Symposium on Circuits and Systems (ISCAS)**, 2019.

- [21] Liheng Lou, Kai Tang, **Zhongyuan Fang**^{*}, Bo Chen, Ting Guo, Chuanshi Yang, and Yuanjin Zheng, Radar Transceivers for Inverse Synthetic Aperture Radar (ISAR) Imaging of Human Activity in 65nm CMOS, **-IEEE International System-on-Chip Conference (SOCC), 2019 (Corresponding author) (invited)**.
- [22] Kai Tang, Chuanshi Yang, **Zhongyuan Fang**, Wensong Wang, Nan Wang, Yao Zhu, Eldwin Jiaqiang Ng, Chun-Huat Heng, and Yuanjin Zheng, A 75.3 pJ/b Ultra-Low Power MEMS-based FSK Transmitter in ISM-915 MHz Band for Pico-IoT Applications, **-IEEE International Symposium on Circuits and Systems (ISCAS), 2021**.
- [23] Wensong Wang, Shuhui Yang, **Zhongyuan Fang**, Quqin Sun, Yin Chen, and Yuanjin Zheng, Compact Dual-Polarized Wideband Antenna with Dual-/Single-Band Shifting for Micro Base Station Applications, **-IEEE Transactions on Antennas and Propagation, 2021**.
- [24] **Zhongyuan Fang** *et al.*, Integrated Wideband Chip-Scale RF Transceivers for Radar Sensing and UWB Communications: A Survey, **-IEEE Circuits and Systems Magazine, 2021** (Submitted).
- [25] **Zhongyuan Fang** *et al.*, A CMOS-Integrated Robotic Radar Sensing Platform for Cognitive Interactions with Human, - **IEEE Transactions on Circuits and Systems II, 2021** (Submitted).

Bibliography

- [1] R. Suzman, J. Beard, *Global health and aging*. US Department of State, 2011: 1-32.
- [2] C. Li, K. F. Un, P. Mak, Y. Chen, J. M. Muñoz-Ferreras, Z. Yang, and R. Gómez-García, "Overview of recent development on wireless sensing circuits and systems for healthcare and biomedical applications," *IEEE J. Emerg. Sel. Topics Circuits Syst.*, vol. 8, no. 2, pp. 165-177, Jun. 2018.
- [3] Acharya, U. Rajendra, K. Paul Joseph, N. Kannathal, C. M. Lim, and J. S. Suri, "Heart rate variability: a review," *Medical and biological engineering and computing*, vol. 44, no. 12, pp. 1031-1051, Dec. 2006.
- [4] T. Y. Huang, L. F. Hayward, and J. Lin, "Non-invasive measurement and analysis of laboratory rat's cardiorespiratory movement," *IEEE Trans. Microw. Theory Techn.*, vol. 65, no. 2, pp. 574-581, Feb. 2017.
- [5] J. Tu, T. Hwang, and J. Lin, "Respiration rate measurement under 1-D body motion using single continuous-wave Doppler radar vital sign detection system," *IEEE Trans. Microw. Theory Techn.*, vol. 64, no. 6, pp. 1937-1946, Jun. 2016.
- [6] N. Mehrdad, and N. Tavassolian, "High-Accuracy Heart Rate Variability Monitoring Using Doppler Radar Based on Gaussian Pulse Train Modeling and FTPR Algorithm." *IEEE Trans. Microw. Theory Techn.*, vol. 66, no. 1, pp. 556-567, Jan. 2018.
- [7] Q. Lv *et al.*, "Doppler vital signs detection in the presence of large-scale random body movements," *IEEE Trans. Microw. Theory Techn.*, vol. 66, no. 9, pp. 4261-4270, Sep. 2018.
- [8] T. Fan, C. Ma, Z. Gu, Q. Lv, J. Chen, D. Ye, J. Huangfu, Y. Sun, C. Li, and L. Ran, "Wireless hand gesture recognition based on continuous-wave Doppler radar

- sensors,” *IEEE Trans. Microw. Theory Techn.*, vol. 64, no. 11, pp. 4012-4020, Nov. 2016.
- [9] M. C. Tang, C. M. Liao, F. K. Wang, and T. S. Horng, “Noncontact Pulse Transit Time Measurement Using a Single-Frequency Continuous-Wave Radar,” in 2018 *IEEE MTT-S Int. Microw. Symp.*, Jun. 2018, vol. 1, pp. 1409-1412.
- [10] J. Yan, H. Liu, B. Jiu, Z. Liu, and Z. Bao, “Joint detection and tracking processing algorithm for target tracking in multiple radar system,” *IEEE Sens. J.*, vol. 15, no. 11, pp. 6534-6541, Nov. 2015.
- [11] A. D. Droitcour, O. Boric-Lubecke, V. M. Lubecke, J. Lin, and G. T. Kovacs, “Range correlation and I/Q performance benefits in single-chip silicon Doppler radars for noncontact cardiopulmonary monitoring,” *IEEE Trans. Microw. Theory Techn.*, vol. 52, no. 3, pp. 838-848, Mar. 2004.
- [12] V. Rahman *et al.*, “Doppler Radar Techniques for Accurate Respiration Characterization and Subject Identification,” *IEEE J. Emerg. Selected Topics Circuits Syst.*, vol. 8, no. 2, pp. 350-359, Jun. 2018.
- [13] C. Li, J. Ling, J. Li, and J. Lin, “Accurate Doppler radar noncontact vital sign detection using the RELAX algorithm,” *IEEE Trans. on Instrum. Meas.*, vol. 59, no. 3, pp. 687-695, Mar. 2010.
- [14] S. Takuya, R. Imasaka, H. Taki, T. Sato, M. Yoshioka, K. Inoue, T. Fukuda, and H. Sakai, “Feature-based correlation and topological similarity for interbeat interval estimation using ultrawideband radar,” *IEEE Trans. Biomed. Eng.*, vol. 63, no. 4, pp. 747-757, Apr. 2016.
- [15] P. Bernardi, R. Cicchetti, S. Pisa, E. Piuze, and O. Testa, “Design, realization, and test of a UWB radar sensor for breath activity monitoring,” *IEEE Sens. J.*, vol. 14, no. 2, pp. 584-596, Feb. 2014.

- [16] L. Qiu, S. Liu, Z. Fang, and Y. Zheng, "An Adaptive Beamforming Technique for UWB Impulse Transceiver," *IEEE Trans. Circuits Syst. II*, vol. 66, no. 3, pp. 417-421, Aug. 2018.
- [17] S. Sasaki, F. Shang, S. Kidera, T. Kirimoto, K. Saho, and T. Sato, "Three-dimensional imaging method incorporating range points migration and doppler velocity estimation for UWB millimeter-wave radar," *IEEE Geosci. & Remote Sens. Letters*, vol. 14, no. 1, pp. 122-126, Jan. 2017.
- [18] B. R. Phelan, K. I. Ranney, K. A. Gallagher, J. T. Clark, K. D. Sherbondy, and R. M. Narayanan, "Design of ultrawideband stepped-frequency radar for imaging of obscured targets," *IEEE Sens. J.*, vol. 17, no. 14, pp. 4435-4446, Jul. 2017.
- [19] L. Ren, N. Tran, F. Foroughian, K. Naishadham, J. E. Piou, O. Kilic, and A.E. Fathy, "Short-Time State-Space Method for Micro-Doppler Identification of Walking Subject Using UWB Impulse Doppler Radar," *IEEE Trans. Microw. Theory Techn.*, vol. 66, no. 7, pp. 3521-3534, Jul. 2018.
- [20] M. Muragaki, S. Okumura, K. Maehara, T. Sakamoto, M. Yoshioka, K. Inoue, T. Fukuda, H. Sakai, and T. Sato, "Noncontact respiration monitoring of multiple closely positioned patients using ultra-wideband array radar with adaptive beamforming technique," in *Proc. IEEE ICASSP*, Mar. 2017, pp. 1118–1122.
- [21] M. Mercuri, P. J. Soh, G. Pandey, P. Karsmakers, G. A. E. Vandenbosch, P. Leroux, and D. Schreurs, "Analysis of an indoor biomedical radar-based system for health monitoring," *IEEE Trans. Microw. Theory Techn.*, vol. 61, no. 5, pp. 2061–2068, May 2013.
- [22] J. Wang, X. Wang, L. Chen, J. Huangfu, C. Li, and L. Ran, "Noncontact distance and amplitude-independent vibration measurement based on an extended DACM algorithm," *IEEE Trans. on Instrum. Meas.*, vol. 63, no. 1, pp. 145-153, Jan. 2014.

- [23] G. Wang, C. Gu, T. Inoue, and C. Li, "A hybrid FMCW-interferometry radar for indoor precise positioning and versatile life activity monitoring," *IEEE Trans. Microw. Theory Techn.*, vol. 62, no. 11, pp. 2812-2822, Nov. 2014.
- [24] Z. Peng, J. Muñoz-Ferreras, Y. Tang, C. Liu, R. Gómez-García, L. Ran, and C. Li, "A portable FMCW interferometry radar with programmable low-IF architecture for localization, ISAR imaging, and vital sign tracking," *IEEE Trans. Microw. Theory Techn.*, vol. 65, no. 4, pp. 1334-1344, Apr. 2017.
- [25] Y. Yan, L. Cattafesta, C. Li, and J. Lin, "Analysis of detection methods of RF vibrometer for complex motion measurement," *IEEE Trans. Microw. Theory Techn.*, vol. 59, no. 12, pp. 3556-3566, Dec. 2011.
- [26] P. Park, S. Kim, S. Woo, and C. Kim, "A centimeter resolution, 10 m range CMOS impulse radio radar for human motion monitoring," *IEEE J. Solid-State Circuits*, vol. 49, no. 5, pp. 1125-1134, May 2014.
- [27] T. Chu, J. Roderick, S. Chang, T. Mercer, C. Du, and H. Hashemi, "A short-range UWB impulse-radio CMOS sensor for human feature detection," in *2011 IEEE Int. Solid-State Circuits Conf. Tech. Dig.*, Feb. 2011, vol. 1, pp. 294-296.
- [28] D. Zito, D. Pepe, M. Mincica, and F. Zito, "A 90nm CMOS SoC UWB pulse radar for respiratory rate monitoring," *IEEE Int. Solid-State Circuits Conf. Tech. Dig.*, Feb. 2011, vol. 1, pp. 40-41.
- [29] D. Zito *et al.*, "SoC CMOS UWB pulse radar sensor for contactless respiratory rate monitoring," *IEEE Tran. Biomed. Circuits Syst.*, vol. 5, no. 6, pp. 503-510, Dec. 2011.
- [30] A. Nikolaj *et al.*, "A 118-mw pulse-based radar soc in 55-nm cmos for non-contact human vital signs detection," *IEEE J. Solid-State Circuits*, vol. 52, no. 12, pp. 3421-3433, Dec. 2017.

- [31] L. Lou, K. Tang, B. Chen, T. Guo, Y. Wang, W. Wang, Z. Fang, Z. Liu, and Y. Zheng, "A 253mW/channel 4TX/4RX pulsed chirping phased-array radar TRX in 65nm CMOS for X-band synthetic-aperture radar imaging," in *2018 IEEE Int. Solid-State Circuits Conf. Tech. Dig.*, Feb. 2018, vol.1, pp. 160-162.
- [32] C. M. Lai, J. M. Wu, P. C. Huang, and T. S. Chu, "A scalable direct-sampling broadband radar receiver supporting simultaneous digital multibeam array in 65nm CMOS," *IEEE Int. Solid-State Circuits Conf. Tech. Dig.*, Feb. 2013, vol.1, pp. 242-243.
- [33] C. Cheung, R. Shah, and M. Parker, "Time delay digital beamforming for wideband pulsed radar implementation," *Proc. IEEE Int. Symp. Phased Array Syst. Technol.*, Oct. 2013, pp. 448–455.
- [34] W. Wang, Z. Qu, Z. Shen, L. Lou, K. Tang, and Y. Zheng, "Design of broadband phased array antenna at X-band," *IEEE Progr. Electromag. Res. Symp. -FALL*, Nov. 2017, vol. 1, pp.1563-1567.
- [35] Z. Fang, L. Lou, C. Yang, K. Tang, and Y. Zheng, "A Ku-band FMCW Radar on Chip for Wireless Micro Physiological Signal Monitoring by Interferometry Phase Analysis," *IEEE Int. Symp. Circuits Syst.*, May. 2018, vol 1, pp. 1-4.
- [36] L. Ren, H. Wang, K. Naishadham, O. Kilic, and Aly E. Fathy, "Phase-based methods for heart rate detection using UWB impulse Doppler radar," *IEEE Trans. Microw. Theory Techn.*, vol. 64, no. 10, pp. 3319-3331, Oct. 2016.
- [37] Y. Koo, L. Ren, Y. Wang, and Aly E. Fathy, "UWB MicroDoppler radar for human gait analysis, tracking more than one person, and vital sign detection of moving persons," *IEEE MTT-S Int. Microw. Symp.*, Jun. 2013, vol. 1, pp. 1-4.

- [38] H. Hashemi, X. Guan, A. Komijani, and A. Hajimiri, "A 24-GHz SiGe phased-array receiver-LO phase-shifting approach," *IEEE Trans. Microw. Theory Techn.*, vol. 53, no. 2, pp. 614-626, Feb. 2005.
- [39] A. Asoodch, and M. Atarodi, "A full 360°vector-sum phase shifter with very low RMS phase error over a wide bandwidth," *IEEE Trans. Microw. Theory Techn.*, vol. 60, no. 6, pp. 1626-1634, Apr. 2012.
- [40] M. Mercuri, I. R. Lorato, Y. H. Liu, F. Wieringa, C. Van Hoof, and T. Torfs, "Vital-sign monitoring and spatial tracking of multiple people using a contactless radar-based sensor," *Nature Electronics*, vol. 1, 2019.
- [41] Christopher F. Barnes, Synthetic Aperture Radar. Barnes, 2015.
- [42] V. C. Chen, F. Li, S. -. Ho, and H. Wechsler, "Micro-Doppler effect in radar: phenomenon, model, and simulation study," *IEEE Trans. Aerospace Electronic Syst.*, vol. 42, no. 1, pp. 2-21, Jan. 2006.
- [43] Z. Peng, J. M. Muñoz-Ferreras, R. Gómez-García, and C. Li, "FMCW radar fall detection based on ISAR processing utilizing the properties of RCS, range, and Doppler," in *2016 IEEE MTT-S Int. Microw. Symp.*, May. 2016, vol. 1, pp. 1-3.
- [44] P.A. Hager, and L. Benini, "LightProbe: A Digital Ultrasound Probe for Software-Defined Ultrafast Imaging," *IEEE Trans. Ultrason., Ferroelect., Freq. Control*, vol. 66, no. 4, pp. 747-760, Feb. 2019.
- [45] B. Behroozpour, P.A. Sandborn, N. Quack, T.J. Seok, Y. Matsui, M.C. Wu, and B.E. Boser, "Electronic-photonic integrated circuit for 3D microimaging," *IEEE J. Solid-State Circuits*, vol. 52, no.1, pp. 161-172, Nov. 2016.
- [46] R.J. Przybyla, H.Y. Tang, A. Guedes, S.E. Shelton, D.A. Horsley, B.E. Boser, "3D ultrasonic rangefinder on a chip," *IEEE J. Solid-State Circuits*, vol. 50, no. 1, pp. 320-334, Dec. 2014.

- [47] H.Y. Tang, Y. Lu, X. Jiang, E.J. Ng, Tsai JM, Horsley DA, Boser BE, “3-D ultrasonic fingerprint sensor-on-a-chip,” *IEEE J. Solid-State Circuits*, vol. 51, no. 11, pp. 2522-2533, Nov. 2016.
- [48] A. Bhuyan, J.W. Choe, B.C. Lee, I. Wygant, A. Nikoozadeh, O. Oralkan, B.T. Khuri-Yakub, “3D volumetric ultrasound imaging with a 32×32 CMUT array integrated with front-end ICs using flip-chip bonding technology,” in *IEEE ISSCC Dig. Tech. Papers*, Feb. 2013, pp. 396-397.
- [49] K. Chen, H.S. Lee, A.P. Chandrakasan and C.G. Sodini, “Ultrasonic imaging transceiver design for CMUT: A three-level 30-Vpp pulse-shaping pulser with improved efficiency and a noise-optimized receiver,” *IEEE J. Solid-State Circuits*, vol. 48, no. 11, pp. 2734-45, Nov. 2013.
- [50] K. Chen, H.S. Lee, and C.G. Sodini, “A column-row-parallel ASIC architecture for 3-D portable medical ultrasonic imaging,” *IEEE J. Solid-State Circuits*, vol. 51, no. 3, pp. 738-751, Dec. 2015.
- [51] A. Zerda *et al.*, “Photoacoustic molecular imaging using single walled carbon nanotubes in living mice,” *Proc. SPIE*, vol. 7177, p. 717725, Feb. 2009.
- [52] S. Park, J. Jang, J. Kim, Y.S. Kim, and C. Kim, “Real-time triple-modal photoacoustic, ultrasound, and magnetic resonance fusion imaging of humans,” *IEEE Trans. Med. Imag.*, vol. 36, no. 9, pp. 1912-1921, Apr. 2017.
- [53] A. Danielli, K. Maslov, A. Garcia-Urbe, A. M. Winkler, C. Li, L. Wang, Y. Chen, G. W. Dorn 2nd, and L. V. Wang, “Label-free photoacoustic nanoscopy,” *J. Biomed. Opt.*, vol. 19, no. 8, pp. 086006, Aug. 2014.
- [54] J. Yao, L. Wang, C. Li, C. Zhang, and L. V. Wang, “Photoimprint photoacoustic microscopy for threedimensional label-free subdiffraction imaging,” *Phys. Rev. Lett.*, vol. 112, no. 1, pp. 014302, Jan. 2014.

- [55] E.M. Stroh, M.J. Moore, and M.C. Kolios, "Single cell photoacoustic microscopy: a review," *IEEE Jour. Selec. Topics Quant. Electronics.*, vo.22, no. 3, pp. 137-51, Nov. 2015.
- [56] J. Tang, R. N. Germain, and M. Cui, "Superpenetration optical microscopy by iterative multiphoton adaptive compensation technique," *Proc. Natl. Acad. Sci.*, vol. 109, no. 22, pp. 8434–8439, May. 2012.
- [57] H. Jin *et al.* "Fast and High-resolution Three-dimensional Hybrid-domain Photoacoustic Imaging Incorporating Analytical Focused Transducer Beam Amplitude," *IEEE Trans. Med. Imag.*, May. 2019.
- [58] F. Gao, X. Feng, and Y. Zheng, "Coherent photoacoustic-ultrasound correlation and imaging," *IEEE Trans. Biomed. Engin.*, vol. 61, no. 9, pp. 2507-2512, Sep. 2014.
- [59] H. Jin, R. Zhang, S. Liu, Z. Zheng, Y. Zheng, "A Single Sensor Dual-Modality Photoacoustic Fusion Imaging for Compensation of Light Fluence Variation," *IEEE Trans. on Biomed. Engin.*, vol. 66, no. 6, pp. 1810-1813, Mar. 2019.
- [60] O. Tzang, and R. Piestun, "Lock-in detection of photoacoustic feedback signal for focusing through scattering media using wave-front shaping," *Optics Express*, vol. 24, no. 24, pp. 28122-28130, Nov. 2016.
- [61] H. Nan, and A. Arbabian, "Peak-power-limited frequency-domain microwave-induced thermoacoustic imaging for handheld diagnostic and screening tools," *IEEE Trans. Microw. Theory Techn.*, vol. 65, no. 7, pp. 2607-2616, Jul. 2017.
- [62] H. Nan, S. Liu, J.G. Buckmaster, and A. Arbabian, "Beamforming Microwave-Induced Thermoacoustic Imaging for Screening Applications," *IEEE Trans. Microw. Theory Techn.*, vol. 67, no. 1, pp. 464-474, Nov. 2018.

- [63] H.Y. Tang, Y. Lu, S. Fung, D.A. Horsley, and B.E. Boser, "Integrated ultrasonic system for measuring body-fat composition," *IEEE ISSCC Dig. Tech. Papers*, Feb. 2015, pp. 1-3.
- [64] H.Y. Tang, D. Seo, U. Singhal, X. Li, M.M. Maharbiz, E. Alon, and B.E. Boser, "Miniaturizing ultrasonic system for portable health care and fitness," *IEEE Trans. Biomed. Circuits Syst.*, vol. 9, no. 6, pp. 767-776, Dec. 2015.
- [65] M.C. Chen, A.P. Perez, S.R. Kothapalli, P. Cathelin, A. Cathelin, S.S. Gambhir, and B. Murmann, "A pixel pitch-matched ultrasound receiver for 3-D photoacoustic imaging with integrated delta-sigma beamformer in 28-nm UTBB FD-SOI," *IEEE J. Solid-State Circuits*, vol. 52, no. 11, pp. 2843-56, Nov. 2017.
- [66] N. Sun, Y. Liu, H. Lee, R. Weissleder, and D. Ham, "CMOS RF biosensor utilizing nuclear magnetic resonance," *IEEE J. Solid-State Circuits*, vol. 44, no. 5, pp. 1629-1643, May 2009.
- [67] Y. Wang, B. Afshar, L. Ye, V.C. Gaudet, and A.M. Niknejad, "Design of a low power, inductor less wideband variable-gain amplifier for high-speed receiver systems," *IEEE Trans. Circuits Syst. I: Regular Papers*, vol. 59, no. 4, pp. 696-707, Nov. 2011.
- [68] S. Liu et al., "Portable photoacoustic system for noninvasive blood temperature measurement," *IEEE Int. Symp. Circuits Syst.*, May 2018, pp. 1-5.
- [69] American National Standards Institute, American national standard for the safe use of lasers, ANSI Standard Z136.1-2000, ANSI, Inc., New York. (2000).
- [70] M.H. Hsieh, L.H. Chen, S.I. Liu and C.C.P. Chen, "A 6.7 MHz to 1.24 GHz 0.0318mm² Fast-Locking All-Digital DLL Using Phase-Tracing Delay Unit in 90 nm CMOS," *IEEE J. Solid-Sate Circuits*, Vol.51, No.2, pp. 412-427, Feb. 2016.

- [71] D.H. Jung, K. Ryu, J.H. Park and S.O. Jung, "All-Digital 90° Phase-Shift DLL With Dithering Jitter Suppression Scheme," *IEEE Trans. Very Large Scale Integration Sys.*, Vol.24, No.3, pp. 1015-1024, March 2016.
- [72] S. Hoyos, C.W. Tsang, J. Vanderhaegen, Y. Chiu, Y. Aibara, H. Khorramabadi and B. Nikolic, "A 15 MHz to 600 MHz, 20 mW, 0.38 mm² Split-Control, Fast Coarse Locking Digital DLL in 0.13 μ m CMOS," *IEEE Trans. Very Large Scale Integration Sys.*, Vol.20, No.3, pp. 564-568, March 2012.
- [73] Y.S. Kim, S.K. Lee, H.J. Park and J.Y. Sim, "A 110 MHz to 1.4 GHz locking 40-phase all-digital DLL," *IEEE J. Solid-State Circuits*, Vol.46, No.2, pp. 435-444, Feb. 2011.
- [74] K. Ryu, J. Jung, D.H. Jung, J.H. Kim and S.O. Jung, "High-Speed, Low-Power, and Highly Reliable Frequency Multiplier for DLL-Based Clock Generator," *IEEE Trans. Very Large Scale Integ. Sys.*, Vol.24, No.4, pp. 1484-1492, April 2016.
- [75] J.M. Lin, C.Y. Yang and H.M. Wu, "A 2.5-Gb/s DLL-Based Burst-Mode Clock and Data Recovery Circuit With 4 \times Oversampling," *IEEE Trans. Very Large Scale Integ. Sys.*, Vol.23, No.4, pp. 791-795, April 2015.
- [76] M. Kim, S. Choi, T. Seong and J. Choi, "A Low-Jitter and Fractional-Resolution Injection-Locked Clock Multiplier Using a DLL-Based Real-Time PVT Calibrator With Replica-Delay Cells," *IEEE J. Solid-State Circuits*, Vol.51, No.2, pp. 401-411, Feb. 2016.
- [77] Q. Ma *et al.*, "A 12ps true-time-delay phase shifter with 6.6% delay variation at 20–40GHz," *Radio Frequency Int. Circuits Symp.*, pp. 61-64, June 2013.
- [78] J. Christiansen, "An integrated high resolution CMOS timing generator based on an array of delay locked loops," *IEEE J. Solid-State Circuits*, Vol.31, No.7, pp. 952-957, July 1996.

- [79] L. Wang, Y. Lian and C.H. Heng, “3–5 GHz 4-Channel UWB Beamforming Transmitter With 1° Scanning Resolution Through Calibrated Vernier Delay Line in 0.13- μ m CMOS,” *IEEE J. Solid-State Circuits*, Vol.47, No.12, pp. 3145-3159, Dec. 2012.
- [80] A. Arbabian *et al.*, “A 94 GHz mm-wave-to-baseband pulsed-radar transceiver with applications in imaging and gesture recognition,” *IEEE J. Solid-State Circuits*, Vol.48, No.4, pp. 1055-1071, April 2013
- [81] T. Sowlati *et al.*, “A 60GHz 144-element phased-array transceiver with 51dBm maximum EIRP and $\pm 60^\circ$ beam steering for backhaul application,” in Proc. 2018 *IEEE Int. Solid-State Circuits Conf. (ISSCC)*, Feb. 2018, pp. 66–68.
- [82] D. Parker *et al.*, “Phased arrays—part 1: Theory and architectures,” *IEEE Trans. Microw. Theory Techn.*, vol. 50, no. 3, pp. 678–687, Mar. 2002.
- [83] Chao Liu *et al.*, “A fully integrated X-band phased-array transceiver in 0.13- μ m SiGe BiCMOS technology,” *IEEE Trans. Microw. Theory Techn.*, vol. 64, no. 2, pp. 575–584, Feb. 2016.
- [84] J. Yan, S. Gogineni, C.-R. Bruno, and J. Brozena, “A dual-polarized 2– 18-GHz Vivaldi array for airborne radar measurements of snow,” *IEEE Trans. Antennas and Propagation*, vol. 64, no. 2, pp. 781-785 Feb. 2016.
- [85] N. Rajesh *et al.*, “Design of Vivaldi antenna with wideband radar cross section reduction,” *IEEE Trans. Antennas and Propagation*, Vol.65, No.4, 2102-2105, 2017.
- [86] M. Ali *et al.*, “Dielectric lens balanced antipodal Vivaldi antenna with low cross-polarization for ultra-wideband applications,” *IET Microwave, Antennas & Propagation*, Vol. 8, No.14, 1137-1142, 2014.

- [87] Abbak, M., M. N. Akinci, M. Cayoren and I. Akduman, "Experimental microwave imaging with a novel corrugated Vivaldi antenna," *IEEE Trans. Ant. and Prop.*, Vol. 65, No. 6, pp. 3302-3307, 2017.
- [88] C. A. Balanis, *Antenna Theory: Analysis and Design*. Hoboken, NJ: Wiley, 2016.
- [89] C. Kim *et al.*, "Deeply penetrating in vivo photoacoustic imaging using a clinical ultrasound array system," *Biomed. Opt. Exp.*, Vol. 1, 335–340, 2010.
- [90] C. P. Favazza, O. Jassim, L. A. Cornelius and L. V. Wang, "In vivo photoacoustic microscopy of human cutaneous microvasculature and a nevus," *J. Biomed. Opt.*, Vol. 16, No. 1, pp. 016015, Jan. 2011.
- [91] J. Roderick *et al.*, "Silicon-Based Ultra-Wideband Beam-Forming," *IEEE J. Solid-State Circuits*, vol. 41, no. 8, pp. 1726–1738, Aug. 2006.
- [92] S. Lee *et al.*, "A K-Band CMOS UWB Four-Channel Radar Front-End with Coherent Pulsed Oscillator Array," *IEEE Trans. Microwave Theory and Techniques*, vol. 63, no. 5, pp. 1735–1745, May. 2015.
- [93] L. Wang *et al.*, "3–5 GHz 4-channel UWB beamforming transmitter with 1° scanning resolution through calibrated Vernier delay line in 0.13-μm CMOS," *IEEE J. Solid-State Circuits*, vol. 47, pp. 3145–3159, Dec. 2012.
- [94] J. Yu *et al.*, "A direct digital synthesis based chirp radar transmitter in 0.13 μm SiGe technology," *Proc. IEEE Bipolar/BiCMOS Circuits Techn. Meeting*, Sep. 2013.
- [95] X. Geng, F. F. Dai, J. D. Irwin, and R. C. Jaeger, "An 11-bit 8.6 GHz direct digital synthesizer MMIC with 10-bit segmented sine-weighted DAC," *IEEE J. Solid-State Circuits*, vol. 45, no. 2, pp. 300–313, Feb. 2010.
- [96] B. Chen *et al.*, "A broadband, high isolation millimeter-wave CMOS power amplifier using a transformer and transmission line matching topology," *Anal. Integr. Circuits Signal Process.*, vol. 81, no. 2, pp. 537–547, Nov. 2014.

- [97] S. Wang, K.-H. Tsai, K.-K. Huang, S.-X. Li, H.-S. Wu, and C.-K.-C. Tzuang, "Design of X-band RF CMOS transceiver for FMCW monopulse radar," *IEEE Trans. Microw. Theory Techn.*, vol. 57, no. 1, pp. 61–70, Jan. 2009.
- [98] D. Shin and G. M. Rebeiz, "A high-linearity X-band four-element phased-array receiver: CMOS chip and packaging," *IEEE Trans. Microw. Theory Techn.*, vol. 59, no. 8, pp. 2064–2072, Aug. 2011.
- [99] D. Shin *et al.*, "A high-power packaged four-element X-band phased-array transmitter in 0.13- μ m CMOS for radar and communication systems," *IEEE Trans. Microw. Theory Techn.*, vol. 61, no. 8, pp. 3060–3071, Aug. 2013.
- [100] J. Yu *et al.*, "An X-band radar transceiver MMIC with bandwidth reduction in 0.13 μ m SiGe technology," *IEEE J. Solid-State Circuits*, vol. 49, no. 9, pp. 1905–1915, Sep. 2014.
- [101] K. Gharibdoust, N. Mousavi, M. Kalantari, M. Moezzi, and A. Medi, "A fully integrated 0.18- μ m CMOS transceiver chip for X-band phased array systems," *IEEE Trans. Microw. Theory Techn.*, vol. 60, no. 7, pp. 2192–2202, Jul. 2012.
- [102] J. P. Comeau *et al.*, "A silicon-germanium receiver for X-band transmit/receive radar modules," *IEEE J. Solid-State Circuits*, vol. 43, no. 9, pp. 1889–1896, Sep. 2008.
- [103] K. J. Koh and G. M. Rebeiz, "An X- and Ku-band 8-element phased array receiver in 0.18 μ m SiGe BiCMOS technology," *IEEE J. Solid- State Circuits*, vol. 43, no. 6, pp. 1360–1371, Jun. 2008.
- [104] B. R. Mahafza, *Radar Systems Analysis and Design using Matlab. London, U.K.: Chapman & Hall, 2000.*
- [105] M. Mercuri *et al.*, "A Direct Phase-Tracking Doppler Radar Using Wavelet Independent Component Analysis for Non-Contact Respiratory and Heart Rate

- Monitoring," *IEEE Trans. Biomed. Circuits Syst.*, vol. 12, no. 3, pp. 632-643, Jun. 2018.
- [106] I. Nasr et al., "A Highly Integrated 60 GHz 6-Channel Transceiver With Antenna in Package for Smart Sensing and Short-Range Communications," *IEEE J. Solid-State Circuits*, vol. 51, no. 9, pp. 2066-2076, Sep. 2016.
- [107] Y. Liu *et al.*, "An Ultralow Power Burst-Chirp UWB Radar Transceiver for Indoor Vital Signs and Occupancy Sensing in 40-nm CMOS," *IEEE Solid-State Circuits Letters*, vol. 2, no. 11, pp. 256-259, Nov. 2019.
- [108] M. Le, "Heart rate extraction based on eigenvalues using UWB impulse radar remote sensing," *Sensors and Actuators A: Physical*, 303, 111689, 2020.
- [109] H.S. Cho and Y.J. Park, "Detection of heart rate through a wall using UWB impulse radar," *J. healthcare engineering*, 2018.
- [110] Y. Wang *et al.*, "A Ku-band 260mW FMCW synthetic aperture radar TRX with 1.48 GHz BW in 65nm CMOS for micro-UAVs," *IEEE Int. Solid-State Circuits Conf. Dig. Tech. Papers*, pp. 240-241, Feb. 2016.
- [111] P. Heydari "Design considerations for low-power ultrawideband receivers," *IEEE Int. Symp. Qua. Electro. Design*, Mar. 2005, pp. 668-673.
- [112] M. Crepaldi, C. Li, J. R. Fernandes and P. R. Kinget, "An Ultra-Wideband Impulse-Radio Transceiver Chipset Using Synchronized-OOK Modulation," *IEEE J. Solid-State Circuits*, vol. 46, no. 10, pp. 2284-2299, Oct. 2011.
- [113] X. Wu, J. L. Sanders, X. Zhang, F. Y. Yamaner and Ö. Oralkan, "An FPGA-Based Backend System for Intravascular Photoacoustic and Ultrasound Imaging," *IEEE Trans. Ultras., Ferroelectrics, and Frequency Control*, vol. 66, no. 1, pp. 45-56, Jan. 2019.

- [114] A. Visweswaran *et al.*, "A 145GHz FMCW-Radar Transceiver in 28nm CMOS," *IEEE Int. Solid-State Circuits Conf. Dig. Tech. Papers*, pp. 168-170, Feb. 2019.
- [115] B. P. Ginsburg *et al.*, "A multimode 76-to-81GHz automotive radar transceiver with autonomous monitoring," *IEEE Int. Solid-State Circuits Conf. Dig. Tech. Papers*, pp. 158-160, Feb. 2018.
- [116] X. Ma *et al.*, "Design of a 100-GHz Double-Sideband Low-IF CW Doppler Radar Transceiver for Micrometer Mechanical Vibration and Vital Sign Detection," *IEEE Trans. Microw. Theory Techn.*, vol. 68, no. 7, pp. 2876-2890, July 2020.
- [117] Z. Fang *et al.*, "Wide Field-of-View Locating and Multimodal Vital Sign Monitoring Based on X -Band CMOS-Integrated Phased-Array Radar Sensor," *IEEE Trans. Microw. Theory Techn.*, vol. 68, no. 9, pp. 4054-4065, Sept. 2020.
- [118] Y. Zheng *et al.*, "A 0.92/5.3nJ/b UWB impulse radio SoC for communication and localization," *IEEE Int. Solid-State Circuits Conf. Dig. Tech. Papers*, pp. 230-231, Feb. 2010.
- [119] Y. Liu *et al.*, " A 680 μ W Burst-Chirp UWB Radar Transceiver for Vital Signs and Occupancy Sensing up to 15m Distance," *IEEE Int. Solid-State Circuits Conf. Dig. Tech. Papers*, pp. 166-168, Feb. 2019.
- [120] Z. Fang *et al.*, "A Digital-Enhanced Chip-Scale Photoacoustic Sensor System for Blood Core Temperature Monitoring and *In Vivo* Imaging," *IEEE Trans. Biomed. Circuits Syst.*, vol. 13, no. 6, pp. 1405-1416, Dec. 2019.
- [121] L. Lou *et al.*, "Radar Transceivers for Inverse Synthetic Aperture Radar (ISAR) Imaging of Human Activity in 65nm CMOS," *IEEE Int. System-on-Chip Conf.*, pp. 471-474, Sep. 2019.

- [122] Z. Fang *et al.*, "A Digital-Enhanced Interferometric Radar Sensor for Physiological Sign Monitoring," *IEEE Int. System-on-Chip Conf.*, pp. 122-125, Sep. 2019.
- [123] Z. Liu, L. Lou, Z. Fang, K. Tang, T. Guo and Y. Zheng, "A DLL-based Configurable Multi-Phase Clock Generator for True-Time-Delay Wideband FMCW Phased-Array in 40nm CMOS," *IEEE Int. Symp. Circuits Syst.*, pp. 1-4, May. 2018.
- [124] Y. Zhu, *et al.*, "A High Coupling Coefficient 2.3-GHz AlN Resonator for High Band LTE Filtering Application," *IEEE Electron Device Lett.*, vol. 37, no. 10, pp. 1344-1346, 2016.
- [125] M. Mercuri, I. R. Lorato, Y. H. Liu, F. Wieringa, C. Van Hoof, and T. Torfs, "Vital-sign monitoring and spatial tracking of multiple people using a contactless radar-based sensor," *Nat. Electron.*, vol. 2, no. 6, pp. 252–262, 2019.
- [126] Jean-Olivier Plouchart *et al.*, "Si-Based 94-GHz Phased Array Transmit and Receive Modules for Real-Time 3D Radar Imaging," *IEEE MTT-S International Microwave Symposium (IMS)*, 2019, pp. 532-534.
- [127] J. Wu, X. Huang, L. Yang, L. Wang, J. Wang, Z. Liu, K. S. Chong, S. W. Lin, and C. Wang, "An Energy-efficient Multi-core Restricted Boltzmann Machine Processor with On-chip Bio-plausible Learning and Reconfigurable Sparsity," *IEEE Asian Solid-State Circuits Conf.*, Nov.9-11, 2020.
- [128] Z. Fang *et al.*, "A Quadrature Adaptive Coherent Lock-in Chip-Based Sensor for Accurate Photoacoustic Detection," *IEEE International Symposium on Circuits and Systems (ISCAS)*, Seville, Spain, 2020, pp. 1-4.
- [129] K. Tang *et al.*, "A 4TX/4RX Pulsed Chirping Phased-Array Radar Transceiver in 65-nm CMOS for X-Band Synthetic Aperture Radar Application," *IEEE Journal of Solid-State Circuits*, vol. 55, no. 11, pp. 2970-2983, Nov. 2020.

- [130] L. Lou, K. Tang, Z. Fang, Y. Wang, B. Chen, T. Guo, X. Feng, S. Liu, W. Wang, and Y. Zheng, "An Early Fusion Complementary RADAR-LiDAR TRX in 65nm CMOS Supporting Gear-Shifting Sub-cm Resolution for Smart Sensing and Imaging," *IEEE International Solid- State Circuits Conference (ISSCC)*, San Francisco, CA, USA, 2021, pp. 220-222.
- [131] Kai Tang, Chuanshi Yang, Zhongyuan Fang, Wensong Wang, Nan Wang, Yao Zhu, Eldwin Jiaqiang Ng, Chun-Huat Heng, Yuanjin Zheng, "A 75.3 pJ/b Ultra-Low Power MEMS-based FSK Transmitter in ISM-915 MHz Band for Pico-IoT Applications," *IEEE International Symposium on Circuits and Systems (ISCAS)*, Korea, pp. 1-4, May 2021.
- [132] B. Baumann, C. Merkle, R. Leitgeb, M. Augustin, A. Wartak, M. Pircher, and C. Hitzenberger, "Signal averaging improves signal-to-noise in OCT images: But which approach works best, and when?" *Biomed. Opt. Express*, vol. 10, pp. 5755-5775, 2019.